MORPHOLOGY AND SELF-DECONTAMINATION OF POLYMER-METAL OXIDE ELECTROSPUN FIBER

A Dissertation

Presented to the Faculty of the Graduate School

of Cornell University

In Partial Fulfillment of the Requirements for the Degree of

Doctor of Philosophy

by

Dong Jin Woo

January 2012

MORPHOLOGY AND SELF-DECONTAMINATION OF POLYMER-METAL OXIDE ELECTROSPUN FIBER

Dong Jin Woo, Ph. D.

Cornell University 2012

TiO_2 and MgO were investigated as self-decontaminating catalysts on a fibrous substrate. A photo-oxidation mechanism with UV energy resulting in strong oxidation by TiO_2 was demonstrated by degradation of a carbamate pesticide. In contrast, MgO functioned through surface destructive adsorption and thus did not require exposure to UV radiation for self-decontamination to occur. Regarding to the effect of fiber morphology, two types of morphology were studied: Core/sheath fiber and continuous porous fiber structure were formed in electrospinning. In the core/sheath approach by coaxial spinning, a higher density of nanoparticle distribution in the surface region was observed when compared with the uniaxial approach, which means the probability of interaction between TiO_2 and toxin increased. The core/sheath structure with a higher particle concentration in the sheath provided more rapid initial degradation of toxin and the photocatalytic reaction of core/sheath morphology showed second-order behavior. It was also observed that the fibers containing higher content of TiO_2 degraded more pesticide for both uniaxial and coaxial fibers. Aside from the selective location of nanoparticles to the fiber surface, interconnected porous morphology was studied. With varying the ratio of solvents, different morphologies were observed in electrospun fibers. A polymer solution consisting of An/Ac 60/40 and 15

wt % of CA/PEO 60/40 (80/20 in moles) enabled the highest degree of continuity (0.77) of PEO phase in CA matrix during the electrospinning. The interconnected intra-fiber pores (89 nm width) and large surface area (21.8 m^2/g) were observed at the electrospun fiber fabricated with the above composition. A catalyst incorporated substrate of the nanochanneled fiber contained MgO was investigated as a methyl parathion removal membrane. In both a soaking test and a membrane filtration, the MgO loaded highly channeled fiber was observed to remove more amount of MP, which resulted from the physical adsorption and destructive adsorption. MP was suggested to be adsorbed and removed from solutions by the exposed MgO particles in fiber and the adsorption to porous fiber. The advantage of the channeled morphology over the conventional regular surface in fiber was showed up in a membrane filtration process. SEM, DSC, TGA, XRD, a BET instrument, and HPLC were used to confirm the morphology, chemistry, and removal performance.

BIOGRAPHICAL SKETCH

Dong Jin (DJ) Woo was born and raised in Seoul, Republic of Korea. He received his undergraduate (1995) and Master of Science (1997) in Chemical Engineering from Hanyang University in Seoul. He had worked for SK Energy as a research scientist (1997-2005). Dong Jin began graduate school at Materials Science (Master of Engineering) in Cornell University and received his Doctor of Philosophy degree in Fiber Science, January 2012.

To my family, Chanyoung, Joonyoung and Soolin

ACKNOWLEDGMENTS

A multitude of people deserve recognition for their help with and support of my work. I would like to thank my advisor, Dr. S. Kay Obendorf for her support and encouragement. For the past several years I have been privileged to work in Prof. Obendorf's research group. I am grateful to have worked with truly nice and smart colleagues; Laura Lange for her experimental advice on methyl parathion, Elizabeth Allen for her proof-reading of my manuscripts, and Mark Chan for his helps on literature search and my final exam preparation. I also thank the past members of the Obendorf group; Kuitian Tan, Ellan Spero, Vivechana Dixit and Jagdish Tewari. I also want to thank Xia (Sam) Zeng for his great helps on analytical instruments. And, I really want to thank everyone else who contributed to my work. In particular, I would like to thank Drs. Yong Lak Joo, Juan Hinestroza, Claude Cohen, Emmanuel Giannelis, Margaret Frey and Anil Netravali for their encouragement and advices. Special thanks to Nathaniel Hansen, Daehwan Cho, Jay Hoon Park, John Hunt, John Grazul and Jon Shu. This research was funded by the NTC (C05-CR01); the Cornell Agricultural Experiment Station, North Central Regional Research Project NC 170 federal formula funds, Project NYC329407 received from Cooperative State Research, Education, and Extension Service, U.S. Department of Agriculture; and College of Human Ecology at Cornell University for financial support. This work made use of the Cornell Center for Materials Research Shared Experimental Facilities, supported through the NSF MRSEC program (DMR 1120296).

TABLE OF CONTENTS

LIST OF FIGURES

LIST OF TABLES

CHAPTER 1

INTRODUCTION: BACKGROUND OF LITERATURE

Electrospinning

Though the process of electrically forcing a fluid jet to make fibers, known as electrospinning, has been recognized for over 70 years, its utilization has increased only in the last two decades, likely due to the increased interest in nanotechnology. In 1917, Zeleny performed observational studies on the instability of electrified droplets [1]. The next relevant investigation was performed by Sir Geoffrey Taylor in the 1960s, who published articles relating to the conical shape taken by a liquid droplet to which an electric potential is applied (now known as a "Taylor cone") as well as the fluid jets expelled by electrified liquids [2, 3]. In his work, Taylor noted several intriguing instabilities of these jets; the theoretical treatment of the flow in these jets and their various instabilities is still a subject of research today. The first officially documented case of electrospinning can be found in a patent by Anton Formhals in 1934, in which he describes "an apparatus for producing artificial filaments" using "the action of an electrical field upon liquids containing solid materials dissolved in them." [4] Other early work in the field of electrospinning includes work by Baumgarten on the electrospinning of acrylic fibers [5] and by Larrondo and Manley on the electrospinning of polymer melts [6-8].

In a standard electrospinning process, a solution of polymer in solvent is supplied to a metallic needle held a distance from a ground collecting

substrate. The solution forms a droplet at the end of the needle. Upon application of a high voltage to the needle, the droplet forms a Taylor cone under the influence of the electric field. If the voltage is increased to the point where the cone becomes unstable, an elongational fluid jet emerges from the tip of the cone and is accelerated towards the grounded substrate. As the jet approaches the grounded collecting substrate, it thins due to stretching and solvent evaporation. As the solvent evaporates, the fluid jet solidifies into a polymer fiber, which is deposited on the substrate. The electrospinning process is illustrated in Figure 1.1.

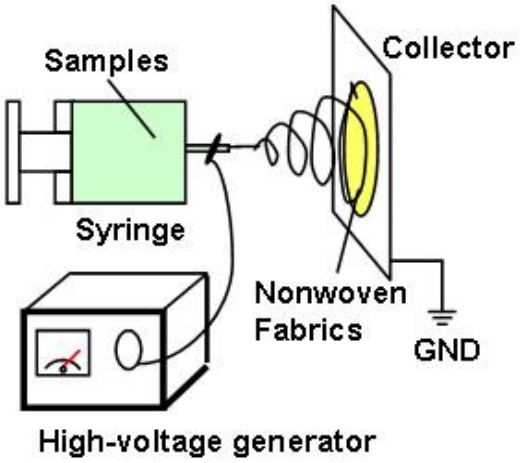

Figure 1.1 Illustration of a Standard Electrospinning System and a Typical Fiber Mat

The majority of work in the field of electrospinning deals with jets of a solution of polymer in solvents that evaporate in ambient air leaving a solid fiber. This technique works well for polymers that are easily dissolved in volatile solvents, and can also be used to make inorganic fibers using sol-gel chemistry [9]. However, there are cases when spinning from solution is either

difficult or impossible and thus other technique must be used. One popular technique is to electrospin from a melt of the desired polymer [10, 11]. In this process, a polymer melt is driven into a jet using an electric field and the solidifying mechanism is cooling of the liquid melt into a solid fiber. The works by Lee et al. and Lyons et al. [12, 13] have demonstrated melt electrospinning of polypropylene fibers ranging from several hundred nanometers to several hundred microns in diameter, depending on the particular polymer used. In another variation, wet electrospinning, a solution is electrospun into a coagulation bath [14-15]. This technique can be used when the solvent required to dissolve the polymer is not volatile enough to fully evaporate before the jet is collected. Electrospinning can also be used to create fibers with a core/sheath microstructure by a process known as coaxial electrospinning [16-19]. In coaxial electrospinning, two coaxially placed spinnerets are utilized to separate the core and sheath polymer solutions. The two solutions are electrospun together, creating fibers with core-sheath structure in a single step. Coaxial electrospinning has been used to easily make hollow nanofibers by using mineral oil as the inner jet, followed by thermal treatment [20]. It has also been used to form core-sheath fibers to effectively functionalize just the surface of the fiber by the coating of the sheath layer.

Polymeric solutions for electrospinning

1. Solubility parameters

Evaluation of certain thermodynamic potentials and related quantities allows prediction of a polymer's solubility in a given solvent, i.e. if a polymer

dissolves in the given solvent or not. Such thermodynamic potential is the 'Gibbs free energy' of mixing G_M and the assign thermodynamic quantities are solubility parameters δ's. When a pure polymer is mixed with a pure solvent at a given temperature T and pressure, the change of Gibbs free energy of mixing is given by the following thermodynamic Equation (1.1):

$$\Delta G_M = \Delta H_M - T\Delta S_M \qquad \text{(Eq. 1.1)}$$

where ΔH_M is the enthalpy change of mixing and ΔS_M is the entropy change of mixing. Since the term ΔS_M is relatively small for polymeric solutions, ΔH_M must be smaller than $T\Delta S_M$ in order to obtain a negative ΔG_M to predict solubility: a negative ΔG_M means that the mixing between the two is spontaneous. The ΔH_M is given by an Equation (1.2) introduced by Hildebrand and Scott [21]:

$$\frac{\Delta H_M}{Vm} = \varphi_1\varphi_2(\delta_1 - \delta_2)^2 \qquad \text{(Eq. 1.2)}$$

where δ_1 and δ_2 are Hildebrand solubility parameters for a polymer and a solvent, while Vm denotes the molar volume. The solubility parameters determine the polymer solubility in the given solvent. Apart from solubility parameters, the related polymer structure heavily influences its solubility. The Hildebrand solubility parameter method was conceptually extended by Hansen [22] aiming to estimate the relative miscibility of polar systems and system with hydrogen bonds. Hansen split up the square of the Hildebrand solubility parameter δ^2 into three components: a dispersion force component

δ_D^2, a polar interaction component δ_P^2, and hydrogen bond component δ_H^2; thus, his approach (Equation 1.3) has a name of '3-D solubility parameters':

$$\delta^2 = \delta_P^2 + \delta_D^2 + \delta_H^2 \qquad \text{(Eq. 1.3)}$$

Hansen used his three-dimensional geometrical model to interpret solubility of polymers graphically. This model introduces a 'solubility volume' of a polymer as a sphere in three-dimensional Cartesian coordination system, whose axes are represented by the three solubility components (δ_D, δp, δ_H). The centre of the solubility sphere is located in the point (${}^P\delta_D$, ${}^P\delta p$, ${}^P\delta_H$) with particular component values of the solubility parameters of the particular polymer. The radius of the solubility sphere is called the 'interaction radius' R (Figure 1.2). Solvents with triplet solubility parameters located at the centre of the Hansen solubility volume dissolve the polymer so effectively that the individual polymer chains are free to uncoil and stretch out. On the other hand, if the polymer is dissolved in solvents localized off-centre of the Hansen solubility sphere, polymer chains remain coiled and grouped together into microscopic clumps that tend to create solutions of lower viscosity, as mentioned by Burke [23].

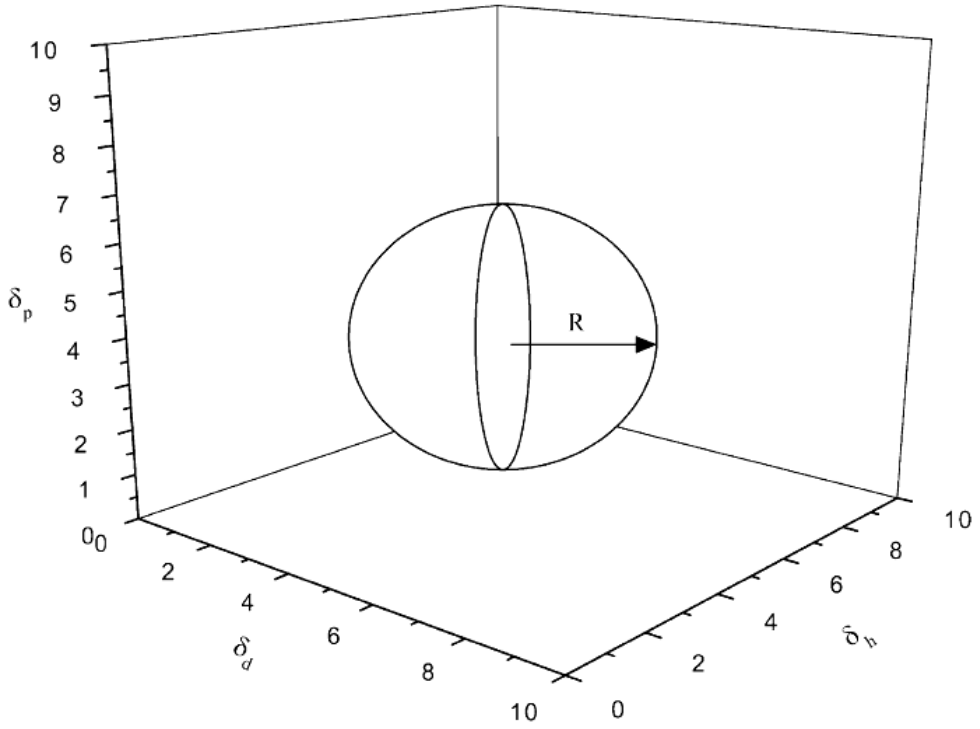

Figure 1.2 Solubility Sphere in the Hansen 3-D Solubility Parameter System (R: Interaction Radius)

The variances in polymer chain configuration can significantly affect the electrospinning process. Wannatong et al. [24] studied behavior of polystyrene (PS) solutions prepared from 18 various solvents. They observed that a significant difference between the solubility parameters of PS and its solvent is responsible for the bead-on-string morphology of electrospun fibers. Liu and Hsieh [25] prepared polymer solutions of cellulose acetate (CA) dissolved in three solvents: acetone, acetic acid and dimethylacetamide (DMAc) with a range of solubility parameter, surface tension, viscosity and boiling temperature. They found that none of these solvents alone enables continuous formation of fibers; however, mixing DMAc with either acetone or acetic acid provides suitable solvent systems for electrospinning technology.

2. Solvent in electrospinning

During electrospinning, the solvent evaporates very promptly as fibers are formed. The solvent evaporation is another important parameter affecting the resultant morphology of nanofibers. When the rate of evaporation of the solvent is too low, then the process leads to formation of a thin film or flat ribbons that are deposited on a collector instead of smooth cylindrical fibers as has been reported by Reneker and Yarin [26]. On the other hand, if the rate of evaporation is too high, fibers are not formed since electrospinning is blocked by the creation of a tiny layer of gel formed on a polymeric solution surface. When a solvent has an optimal volatility, the presence of residual solvent in electrospun nanofibers facilitates the bonding between intersecting fibers grasped by a collector, creating a mechanically strong cohesive structure of fiber webs. This is analogous to thermal or chemical bonding of non-woven fabrics. Jirsak and Wadsworth's [27] study consults more details in the solvent evaporation when electrospinning.

An interesting finding is that the evaporation of solvents sometimes yields polymer fibers with a relatively regular porous structure. The regular phase morphology is induced by a rapid phase separation in electrospinning jet when a highly volatile solvent is used. The solvent rich regions in a jet are apparently transformed into pores after its intensive evaporation. The replacement of dichloromethane with solvents of lower vapor pressure, such as chloroform, reduces the tendency towards pore formation significantly [28]. The elongation of the pores along the fiber axis is most probably the result of a uniaxial jet extension that persists even after the solvent was evaporated. Bognitzki et al. [28] prepared porous ultrafine fibers from polylactic acid,

polycarbonate and poly(vinyl carbazole) with dichlormethane used as the solvent. Khil et al. [29] prepared porous polycaprolactone filaments to study growth of cells on these non-woven fabrics. This work reviled the important role of scaffold porosity for proliferation of living animal cells. Han et al. [30] prepared ultrafine porous cellulose triacetate fibers by electrospinning methylene-chloride and a mixed solvent of MC and ethanol. In Chapter 3, electrospinning polymer blends consisting of cellulose acetate (CA) and polyethylene oxide (PEO) dissolved in a mixture of acetonitrile (An) and acetone (Ac) will be described in terms of continuous structure in electrospun fibers. Before the CA/PEO solution jet ejected, each polymer was interacted with each solvent bearing different solubility and vapor pressure. Consequently, the various polymer mixing conditions and phase separation behaviors dominantly affected fiber morphology.

Cellulose and the derivatives

Cellulose and its derivatives are major biomacromolecules and are among the most widely employed natural polymers in numerous industrial fields, such as textiles, packaging materials, films, membranes and thermoplastics. However, the limitations of cellulose utilization are poor solubility in most solvents and are not melt processible due to the decomposition prior to melting. In cellulose, glucose units produce linear polymer chains that can align side by side, presenting interchain hydrogen bonding. These intermolecular links produce a rigid structure of layered sheets of cellulose (Figure1.3) resulting in the insolubility in water. In contrast, organic derivatives of cellulose allow the materials to be processed into various useful forms. The modification of its physical properties can greatly expand its

application fields [31]. Cellulose esters and cellulose ethers have been pioneer compounds of cellulose derivatives and remain the most important derivatives of cellulose [32].

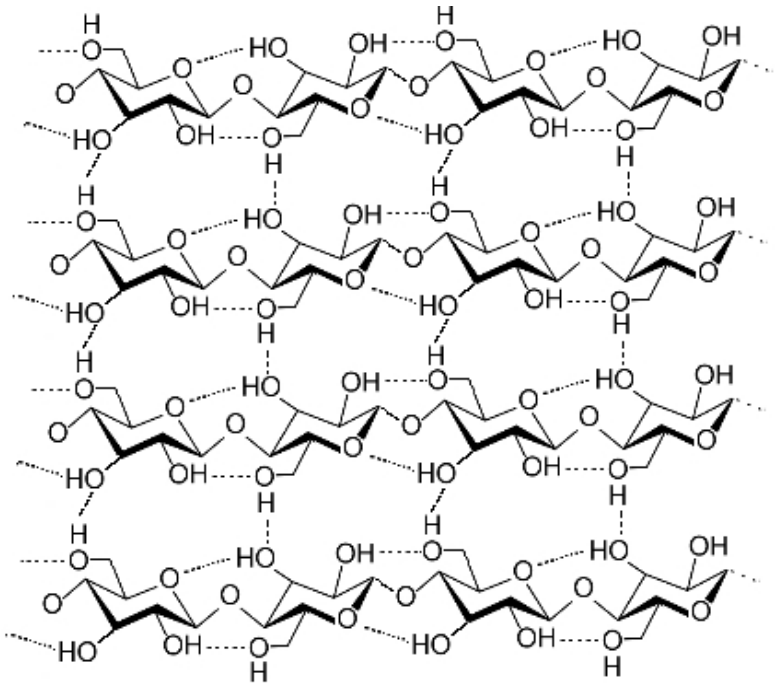

Figure 1.3 Molecular Structure of Cellulose

To obtain cellulose electrospun fibers via more straightforward electrospinning processes, several researchers have worked with cellulose acetate as a starting material. Cellulose acetate has the advantages of ready solubility in suitable electrospinning solvents and straightforward conversion to cellulose by means of deacetylation (Figure 1.4). In this article, many of studies have conducted with cellulose acetate due to its versatility, and finally the findings were applied to cellulose to expand the potential to more stable region rather than cellulose acetate, especially in molecular damages such as degradation by oxidation and hydrolysis.

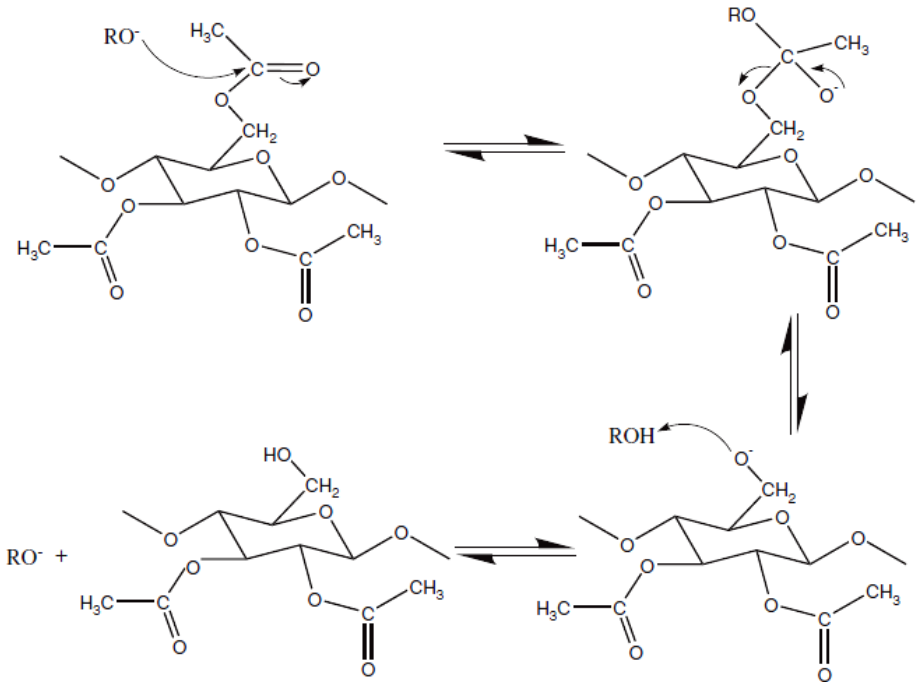

Figure 1.4 Deacetylation Process; Converting Cellulose Acetate into Cellulose

Self-decontamination and destructive adsorbent nanoparticle

Self-decontaminating materials are defined as substances or objects designed and fabricated to deactivate pathogenic microorganisms or chemical warfare agents [31]. Self-decontamination makes it possible for continuous protection against toxic materials. In order to develop destructive barriers against biological and chemical air pollutants, protective clothing and membranes

using catalytic or enzymatic degradation have recently been studied in various fields such as air purification system, chemical biological defense for weapons demilitarization, and personal protection wear [32-34]. When engineering the self-contaminating protective systems, catalytic performance and the structure and property of substrate should be investigated and selected.

Metal oxides such as titanium dioxide (TiO_2) and magnesium oxide (MgO) have been investigated as a self-decontaminating catalyst for almost four decades [35]. These metal compounds have been studied in various forms such as metal nanoparticle [36], encapsulated particle [37], aerogel [38], and nanofiber [39, 40]. A photo-oxidation mechanism was suggested to define the driving force of strong oxidation by such metal based inorganic catalysts [41]. However, the catalytic activities of titanium dioxide drastically increase only with the energy of ultra-violet region. While much has been reported on the photo-catalytic performance of TiO_2, its real applications are still not satisfactory due to many limitations, especially the necessity of source light in the UV region. On the contrary, MgO does not have such limitations, furthermore, it is reported that MgO is very effective to decompose organophosphorous compounds with P-S or P-O bonds [42-44]. In this thesis, both TiO_2 and MgO have been employed in the self-decontamination fiber system using an electrospun membrane as a substrate of the metal oxide particles.

Nanoscale metal oxide compounds have been reported to be strong degradation catalysts for organic compounds. Klabunde et al. [36, 45]

classified metal oxides and showed some examples of their unique properties in terms of particle size. Particle sizes are dependent on the formation methods. Chemists reported several methods for the preparation of metal oxides. The most common one is a conventional preparation (CP) and the other is an aerogel method (AP). While the former uses boiling water and vacuuming treatments, the latter uses hydrolysis and thermal treatments with autoclaving. The unique characteristics of the particles made by the two methods are surface area and crystal size. Aerogel-prepared (AP) nanoparticles have larger surface area and smaller crystals compared with conventional prepared (CP) ones; for example, CP-MgO has 150 m^2g^{-1} of surface area and 8 nm of crystal size and AP-MgO has 400 m^2g^{-1} and 4 nm [42].

Crystallite nanomaterials exhibit a wide spectrum of unusual properties and can be considered as new materials that bridge molecular and condensed matter through a surface adsorption [46]. The enhanced chemical reactivity suggests a two-step decomposition mechanism of the adsorbates on nanoparticles (first step – adsorption of toxic agent on the surface by means of physisorption, followed by the second step – chemical decomposition). This two-step mechanism substantially enhances the detoxification abilities of nanoparticles because it makes the decomposition less dependent on the rate of chemical reaction which is affected by the agent-nanoparticle combination and temperature. Reactive nanoparticles do not have such a drawback because the surface adsorption sites remain active even at low temperature. In this way, the toxins are trapped and eventually undergo “destructive adsorption”.

Destructive adsorption is the typical mechanism of such metal oxide nanoparticle catalysts. The term "destructive adsorption" is often applied to reactions in which the organic compound is "destroyed" during the reaction with metal oxide by becoming mineralized as environmentally benign compound and carbon dioxide gas. Thus, the term is used to differentiate the nanocrystalline metal oxide from materials such as activated carbon or zeolites that simply adsorb the hazardous materials but do not chemically alter them [42]. Several kinds of organic compounds have been used to investigate the degradation activities of metal oxides: acid gases such as SO_2 [43, 45]; chlorine compounds such as CCl_4, CH_2Cl_2, CH_3Cl [45]; hydrocarbons such as acetaldehyde, acetone, trimethylacetaldehyde [46], tetrahydrofuran [44], paraoxon and other pesticides [36, 42, 47]; common air-pollutants; dimethyl methylphosphonate; and even military agents such as GD, VX, and HD[1] [42-44]. Research studying oxidation and adsorption has used UV/Vis, GC, HPLC, MS, and FT-IR to analyze the oxidation performances of the nanoparticles.

Magnesium oxide (MgO) is believed to carry out the oxidative degradation by the cleavage of the P-S bond or P-O bond of organophosphates, the most typical structure of warfare nerve agents. For example, nanocrystalline MgO is able to hydrogen bond with phosphorous compounds at room temperature with hydrolysis of the compounds occurring to produce surface bound species. Figure 1.5 shows a mechanism of destructive adsorption of paraoxon,

[1] Nerve agents GD (soman), HD (Sulfur Mustard) and VX are manufactured compounds. The G-type agents are clear, colorless, tasteless liquids miscible in water and most organic solvents. VX is a clear, amber-colored odorless, oily liquid. It is miscible with water and dissolves in all solvents. VX is the least volatile nerve agent.

an organophosphate compound with P-O bonds. In the Chapter 3, the adsorption reactivity onto the surface of MgO particle will be described. The destructive adsorption study of MgO particles has conducted in the substrate of electrospun fiber that was designed to have larger surface area, which aims the higher reactivity on the larger surface of the substrate that MgO was embedded.

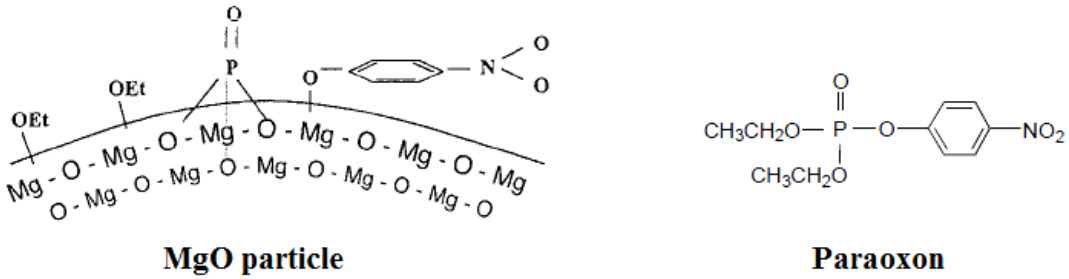

Figure 1.5 Example of Destructive Adsorption Mechanism; Proposed Structure for Adsorbed Paraoxon on Nanocrystalline MgO [32]

Co-continuous polymer blend

Blending different polymers and conserving their individual properties in the final mixture is an extremely attractive and inexpensive way of obtaining new structural materials from a limited palette. Blends have been intensively studied since polymers were first synthesized, and usually consist of a particulate minority phase dispersed in a matrix. A long-sought goal of polymer research is the formation of stable co-continuous blends. A co-continuous blend is a mixture in which a path can be traced from one side of the material to another without moving from one phase to another, and they generally have superior mechanical properties. A route to achieving this is described by Pernot and co-workers [50], owing to a unique combination of

theoretical prediction, judicious selection of starting materials and an *in situ* chemical reaction.

The entropy of mixing of polymers is usually very low, so polymer mixtures tend to phase separate into two layers, just like oil and water. In the solid state, there are few reports of pairs of polymers that will co-crystallize. The most common industrial method of making polymer blends is by mixing the molten polymers in a twin-screw extruder. As a consequence, polymer blends tend to have morphologies that are very dependent on their processing and thermal history. The stiffness of conventional polymer blends tends to be dominated by the matrix, whereas the fracture toughness can be either enhanced or catastrophically reduced by the presence of the particulate phase. Control of polymer morphology is also essential for functional materials, such as conductive and emissive polymer blends, in which phase size and continuity play a role [51]. However, preserving the morphology during processing is not always possible with mechanical mixing alone. Co-continuous morphologies can be induced by mechanical mixing for a wide range of polymer blends, but in most cases once the input of energy from mixing is stopped, the material quickly moves toward equilibrium and co-continuity is lost.

One solution to this problem is to add a 'compatibilizer' to the system, which increases the compatibility between two dissimilar polymers. For two homopolymers, A and B, a linear diblock copolymer (A-B) is a good first choice as a compatibilizer [52]. The diblock copolymer, acting as a macromolecular surfactant, segregates forming a layer at the interface

between the two homopolymers, thereby reducing the interfacial tension between the two domains and stabilizing the microscopic morphologies [53]. The compatibilizer usually stabilizes micrometer-to submicrometer-sized dispersions, and only in very special compositions are they co-continuous. This is the route taken to produce many of the compatiblized blends currently on the market. There is theoretical support [53] for this strategy and it is now possible to design blends with a characteristic dispersed phase in submicron size [54, 55]. Unfortunately for many polymer pairs, such as polyethylene and polyamide studied by Pernot *et al*. [50], it is either very difficult if not impossible to synthesize the crucial diblock polymer.

The main purpose of cocontinuous blends in this study is to create interconnected and continuous porous morphology in polymeric fiber, leading to large surface area. Recently, the importance of interconnected microporous structures was also emphasized by researchers in the polymer field, and many intelligent techniques were invented to make such structures. Existing techniques able to realize this design concept include fiber bonding (nonwoven meshes) [56, 57], solvent casting/particulate leaching [58, 59], phase separation/emulsification [60, 61] and co-continuous melt blending [62-65]. These techniques have been found to be especially useful when dealing with polymers. In particular, co-continuous melt blending has been shown to be an extremely versatile technique; interconnected porous structures with controllable porosity, pore size and even pore size distribution can be generated with this method. The continuous porous structure formation by microphase separation electrospinning and the selective dissolution has been conducted and the study is described in Chapter 3.

REFERENCES

(1) Zeleny, J. "The electrical discharge from liquid points, and a hydrostatic method of measuring the electric intensity at their surfaces" *Physical Review* **1917**, 10 (1), 1.

(2) Taylor, G. *Proceedings of the Royal Society of London. Series A, Mathematical and Physical Sciences* **1964**, 280 (1382), 383-397.

(3) Taylor, G. *Proceedings of the Royal Society of London. Series A, Mathematical and Physical Sciences* **1969**, 313 (1515), 453-475.

(4) Formhals, A. "Process and Apparatus for Preparing Artificial Threads" Process and Apparatus for Preparing Artificial Threads. USP 1975504, **1934.**

(5) Baumgarten, P. K. "Electrostatic spinning of acrylic microfibers" *Journal of Colloid and Interface Science* **1971**, 36 (1), 71.

(6) Larrondo, L.; St John Manley, R. "Electrostatic fiber spinning from polymer melts. I. Experimental observations on fiber formation and properties" *Journal of Polymer Science, Polymer Physics Edition* **1981**, 19 (6), 909.

(7) Larrondo, L.; St John Manley, R. "Electrostatic fiber spinning from polymer melts. II. Examination of the flow field in an electrically driven jet" *Journal of Polymer Science, Polymer Physics Edition* **1981**, 19 (6), 921.

(8) Larrondo, L.; St John Manley, R. "Electrostatic fiber spinning from polymer melts. III. Electrostatic deformation of a pendant drop of polymer melt" *Journal of Polymer Science, Polymer Physics Edition* **1981**, 19 (6), 933.

(9) Li, D.; Xia, Y. "Fabrication of Titania Nanofibers by Electrospinning" *Nano Letters* **2003**, 3 (4), 555-560.

(10) Zhou, H.; Kim, K. W.; Giannelis, E. P.; Joo, Y. L. "Polymeric Nanofibers" In *ACS Symposium*, Reneker, D. H.; Fong, H., Editors American Chemical Society **2006**, 918, 217-230.

(11) Reneker, D. H.; Chun, I. "Nanometre diameter fibres of polymer, produced by electrospinning" *Nanotechnology* **1996**, 7 (3), 216-223.

(12) Lee, S.; Obendorf, S. K. "Developing Protective Textile Materials as Barriers to Liquid Penetration Using Melt-Electrospinning" *Journal of Applied Polymer Science* **2006**, 102 (4), 3430-3437.

(13) Lyons, J.; Li, C.; Ko, F. "Melt-electrospinning part I: processing parameters and geometric properties" *Polymer* **2004**, 45 (22), 7597-7603.

(14) Khil, M.-S.; Bhattarai, S. R.; Kim, H.-Y.; Kim, S.-Z.; Lee, K.-H. "Novel fabricated matrix via electrospinning for tissue engineering" *Journal of Biomedical Materials Research Part B, Applied Biomaterials* **2005**, 72B (1), 117-124.

(15) Piotr, K. "Cellulose nanofibers prepared by the N-methylmorpholine-N-oxide method" *Journal of Applied Polymer Science* **2005**, 98 (4), 1855-1859.

(16) Loscertales, I. G.; Barrero, A.; Marquez, M.; Spretz, R.; Velarde-Ortiz, R.; Larsen, G. "Electrically forced coaxial nanojets for one-step hollow nanofiber design" *J. Am. Chem. Soc.* **2004**, 126, 5376.

(17) Sun, Z.; Zussman, E.; Yarin, A. L.; Wendorff, J. H.; Greiner, A."Compound Core–Shell Polymer Nanofibers by Co-Electrospinning" *Adv. Mater*. **2003**, 15, 1929.

(18) Yu, J. H.; Fridrikh, S. V.; Rutledge, G. C. "Production of submicrometer diameter fibers by two-fluid electrospinning" *Adv. Mater.* **2004**, 16, 1562.

(19) Kalra, V.; Lee, J. H.; Park, J. H.; Marquez, M.; Joo, Y. L. "Confined Assembly of Asymmetric Block-Copolymer Nanofibers via Multiaxial Jet Electrospinning" *Small* **2009**, 5, 20, 2323–2332.

(20) McCann, J. T.; Li, D.; Xia, Y. "Electrospinning of Nanofibers with Core-Sheath, Hollow, or Porous Structures" *J. Mater. Chem.* **2005**, 15, 735.

(21) Hildebrand, J.H.; Scott, R.L. *The Solubility of Nonelectrolytes*, Dover Publications, New York, **1964.**

(22) Hansen, C. *Hansen Solubility Parameters: A User's Handbook*, CRC Press, New York, **2007.**

(23) Burke, J. The Book and Paper Group Annual 3, **1984**, p. 13.

(24) Wannatong, L.; Sirivat, A.; Supaphol, P. "Effects of solvents on electrospun polymeric fibers: preliminary study on polystyrene" *Polym. Int.* **2004**, 53, 1851.

(25) Liu, H. Q.; Hsieh, Y. L. "Ultrafine Fibrous Cellulose Membranes from Electrospinning of Cellulose Acetate" *J. Polym. Sci.* **2002**, B 40, 2119-2129.

(26) Reneker D.H.; Yarin, A. L. "Electrospinning jets and polymer nanofibers" *Polymer* **2008**, 49, 2387.

(27) O. Jirsak and L.C. Wadsworth, *Nonwoven Textiles*, Carolina Academic Press, Durham, **1999.**

(28) Bognitzki, M.; Czado, W.; Frese, T.; Schaper, A.; Hellwig, M.; Steinhart, M.; Greiner, A.; Wendorff, J. H. "Nanostructured Fibers via Electrospinning" *Adv. Mater*. **2001**, 13, 70.

(29) Khil, M.S.; Bhattarai, S.R.; Kim, H.Y.; Kim, S.Z.; Lee, K.H. "Novel fabricated matrix via electrospinning for tissue engineering." *J. Biomed. Mater. Res*. **2005**, 72B, 117.

(30) Han, S. O.; Son, W. K.; Youk, J. H.; Lee, T. S.; Park, W. H. "Ultrafine Porous Fibres Electrospun from Cellulose Triacetate" *Mater. Lett*. **2005**, 59, 2998.

(31) Braun, J. L.; Kadla, J. F. "Diffusion and Saponification Inside Porous Cellulose Triacetate Fibers" *Biomacromolecules* **2005**, 6, 152-60.

(32) Edgar, K. J.; Buchanan, C. M.; Debenham, J. S.; Rundquist, P. A.; Seiler, B. D.; Shelton, M. C.; Tindall, D. "Advances in Cellulose Ester Performance and Application" *Prog. Polym. Sci*. **2001**, 26, 1605.

(33) Wander, J. D. "Self-Decontaminating Materials" The Society of American Military Engineers Force Protection Symposium, Charleston, S.C., 1 November **2001.**

(34) Self-Decontaminating Filters, Clothing, and Disposable Wipes, Naval Research Laboratory, US Patent 10,750, 637.

(35) Tan, K.; Obendorf, S. K. "Fabrication and Evaluation of Electrospun Nanofibrous Antimicrobial Nylon 6 Membranes" *J. Mem. Sci.,* **2007**, 305, 287.

(36) Schreuder-Gibson, H.; Gibson, P.; Senecal, K.; Sennett, M.; Walker, J.; Yeomans, W.; Tsai, P. "Protective Textile Materials Based on Electrospun Nanofibers" *J. Adv. Mater.* **2002**, 34, 44.

(37) Fujishima A.; Honda, K. "Photocell using Covalently-bound Dyes on Semiconductor Surfaces" *Nature* **1972**, 37, 238.

(38) Klabunde, K. J.; Stark, J.; Koper, O.; Mohs, C.; Park, D. G.; Decker, S.; Jiang, Y.; Lagadic, I.; Zhang, D. "Nanocrystals as Stoichiometric Reagents with Unique Surface Chemistry" *J. Phys. Chem.* **1996**, 100, 12142.

(39) Shchukin, D.G.; Ustinovich, E.; Sviridov, D. V.; Lvov, Y. M.; Sukhorukov, G. B. "Photocatalytic Microreactor based on TiO_2-modified Polyelectrolyte Multilayer Capsules" *Photochem. Photobiol. Sci.* **2003**, 2, 975.

(40) Baia, L.; Peter, A.; Cosoveanu, V.; Indrea, E.; Baia, M.; Popp, J.; Danciu, V. "Synthesis and Nanostructural Characterization of TiO_2 Aerogels for Photovoltaic Devices" *Thin Solid Films* **2006**, 511-512, 512.

(41) Kobayashi, S.; Hanabusa, K.; Suzuki, M.; Kimura, M.; Shirai, H. "Preparation of TiO_2 Fiber in a Sol-Gel System Containing Organogelator" *Chemistry Letters* **1999**, 1077.

(42) Lee, S. W.; Kim, Y. U.; Choi, S.-S.; Park, T. Y.; Joo, Y. L.; Lee, S. G. "Preparation of SiO_2/ TiO_2 Composite Fibers by Sol-Gel Reaction and Electrospinning" *Materials Letters* **2007**, 61, 889.

(43) Linsebigler, A. L.; Lu, G.; Yates Jr., J. T. "Photocatalysis on TiO_2 Surfaces: Principles, Mechanisms, and Selected Results" *Chem. Rev*. **1995**, 95, 735.

(44) Rajagopalan, S.; Koper, O.; Decker, S.; Klabunde, K. J. "Nanocrystalline Metal Oxides as Destructive Adsorbents for Organophosphorus Compounds at Ambient Temperatures" *Chem. Eur. J.* **2002**, 8, 11, 2602.

(45) Decker, S.; Klabunde, K. J. "Enhancing Effect of Fe_2O_3 on the Ability of Nanocrystalline Calcium Oxide to Adsorb SO_2" *J. Am. Chem. Soc*. **1996**, 118, 12465.

(46) Wagner, G. W.; Procell, L. R.; O'Connor, R. J.; Munavalli, S.; Carnes, C. L.; Kapoor P. N.; Klabunde, K. J. "Reactions of VX, GB, GD, and HD with Nanosize Al_2O_3. Formation of Aluminophosphonates" *J. Am Chem. Soc*. **2001**, 123, 1636.

(47) Koper, O.; Li, Y.; Klabunde, K. J. "Destructive Adsorption of Chlorinated Hydrocarbons on Ultrafine (Nanoscale) Particles of Calcium Oxide" *Chem. Mater*. **1993**, 5, 500.

(48) Khaleel, A.; Kapoor, P. N.; Klabunde, K. J. "Nanocrystalline Metal Oxides As New Adsorbents for Air Purification" *Nanostructured Materials* **1999**, 11, 459.

(49) Li, Y. X.; Klabunde, K. J. "Nano-scale metal oxide particles as chemical reagents. Destructive adsorption of a chemical agent simulant, dimethyl

methylphosphonate, on heat-treated magnesium oxide" *Langmuir* **1991**, 7, 1388.

(50) Pernot, H.; Baumert, M.; Court, F.; Leibler, L. "Design and properties of co-continuous nanostructured polymers by reactive blending" *Nature Mater.* **2002**, 1, 54–58.

(51) Arias, A. C.; MacKenzie, J. D.; Corcoran, N.; Friend, R. H. "Lateral and vertical phase separation control of thin-film structures for photovoltaics" *Mater. Res. Soc. Symp. Proc.* **2002**, 665, 199–205.

(52) Wilkinson, A. N.; Ryan, A. J. *Polymer Processing: Structure Development,* Kluwer, Dordrecht, The Netherlands, **1998**.

(53) Shull, K. R.; Kramer, E. "Mean-Field Theory of Polymer Interfaces in the Presence of Block Copolymers" *J. Macromolecules* **1990**, 23, 4769–4779.

(54) Nakayama, A.; Inoue, T.; Guegan, P.; Macosko, C. W. "Compatibilizers for melt blending: premade vs. reactively formed block copolymers" *Polym. Prepr.* **1993**, 34, 840–841.

(55) Adedeji, A.; Lyu, S.; Macosko, C. W. "Block copolymers in homopolymer blends: Interface vs micelle" *Macromolecules* **2001**, 34, 8663–8668.

(56) Mooney, D. J.; Mazzoni, C. L.; Breuer, C.; McNamara, K.; Hern, D.; Vacanti, J. P. "Stabilized polyglycolic acid fibre-based tubes for tissue engineering" *Biomaterials* **1996**, 17, 115–24.

(57) Freed, L. E.; Marquis, J. C.; Nohria, A.; Emmanual, J. Mikos, A. G.; Langer, R. "Neocartilage Formation In Vitro and In Vivo Using Cells Cultured on Synthetic Biodegradable Polymers" *J. Biomed. Mater. Res.* **1993**, 27, 11–23.

(58) Thompson, R. C.; Yaszemski, M. J.; Powers, J. M.; Mikos, A. G. "Hydroxyapatite fiber reinforced poly(a-hydroxy ester) foams for bone regeneration" *Biomaterials* **1998**, 19, 1935–1943.

(59) Mikos, A. G.; Bao, Y.; Cima, L. G.; Ingber, D. E.; Vacanti, J. P.; Langer, R. "Preparation of poly(glycolic acid) bonded fiber structures for cell attachment and transplantation" *J. Biomed. Mater. Res.* **1993**, 27, 183–189.

(60) Whang, K.; Thomas, C. H.; Healy, K. E.; Nuber, G. "A novel method to fabricate bioabsorbable scaffolds" *Polymer* **1995**, 36, 837–842.

(61) Schugens, C.; Maquet, V.; Grandfils, C.; Jerome, R.; Teyssie, P. "Polylactide macroporous biodegradable implants for cell transplantation 2. Preparation of polylactide foams by liquid-liquid phase separation" *J. Biomed. Mater. Res.* **1996**, 30, 449–461.

(62) Potschke, P.; Paul, D. R. "Formation of Co-continuous Structures in Melt Mixed Immiscible Polymer Blends" *J. Macromol. Sci., Polym. Rev.* C **2003**, 43, 87–141.

(63) Yuan, Z. H.; Favis, B. D. "Macroporous poly(L-lactide) scaffold 1. Preparation of a macroporous scaffold by liquid-liquid phase separation of a PLLA-dioxane-water system" *Biomaterials* **2004**, 25, 2161–2170.

(64) Yao, D.; Zhang, W.; Zhou, J. G. "Controllable growth of gradient porous structures." *Biomacromolecules* **2009**, 10, 1282–1286.

(65) Zhang, W.; Deodhar, S.; Yao, D. "Geometrical confining effects in compression molding of co-continuous polymer blends" *Ann. Biomed. Eng.* **2010**, 38, 1954–1964.

CHAPTER 2

PHOTOCATALYTIC SELF-DETOXIFICATION BY COAXIALLY ELECTROSPUN FIBER CONTAINING TiO_2 NANOPARTICLES

1. INTRODUCTION

Photocatalysis, a partial oxidation of alkanes and olefinic hydrocarbons, was introduced and developed in 1970 [1]; these reactions took place at ambient temperature under ultra-violet irradiation. The nature of the reaction medium is heterogeneous being comprised of at least two phases: the solid (catalyst) and a fluid reagent (gas or liquid). Current research and development activities use the application of photocatalysis as the basis for environmentally friendly technologies. Ollis and co-workers [2] demonstrated that the hydroxyl radicals produced during the sequence of light-induced redox reactions were responsible for the oxidative degradation of organic pollutants present in water and air with titania as a photocatalyst. Within the past 30 years, semiconductor photocatalysis has been successfully used in the removal of over 1200 different organic toxicants in various media [3].

Titanium dioxide (TiO_2) as a photocatalyst has been investigated for almost four decades [4]. Photoxidation, one of the unique features of this metal oxide, is a mechanism suggested to define the driving force of strong oxidation by such metal based inorganic catalysts [5]. Titanium dioxide has been studied in various forms such as nanoparticles [6], cluster [7], encapsulated particle [8],

thin film [9], aerogel [10] and nanofiber [11, 12] considering various applications such as highly efficient photocatalysis, solar energy conversion and self-cleaning ingredient. In this study, TiO_2 nanoparticles were employed to form a photocatalytic nanofiber based on a polymeric substrate.

Coaxial electrospinning provides the technology to produce many different morphologies and nanofiber structures that were previously unattainable through simple monoaxial electrospinning [13]. Introduced around 2003 [14-16], it uses two different fluids flowing through concentric spinnerettes to generate nanofibers with a core-sheath structure [17]. Previous studies have indicated that while monoaxial nanofibers exhibit the capability to support catalytic nanoparticles and prevent their aggregation, if these nanoparticles are located at the center of the nanofiber there is a significant mass transfer limitation for the reactant to reach the catalytic particles thereby making any catalyst at the center virtually unavailable [18]. Coaxial electrospinning can be used to tune the catalyst location in the shell or surface region of the nanofiber. In this work, TiO_2 nanoparticle was used as a self-decontaminating catalyst in both monoaxial and coaxial electrospun nanofibers to study any photocatalytic differences due to nanoparticle distributions: randomly distributed nanoparticles by monoaxial electrospinning versus sheath side embedded ones by coaxial.

2. EXPERIMENTAL SECTION

2.1 Materials

Polyacrylonitrile (PAN) (Mn ~150 kDa, Poly Science Inc., Warrington, PA), *N, N*-dimethylformamide (DMF) (98%, Fluka, Milwaukee, WI) and aldicarb (2-methyl-2(methylthio)propanal o-[(methylamino)-carbonyl] oxime, purity 99%, FW:190.26, Chem Service, West Chester, PA) were purchased commercially and anatase titanium dioxide (TiO_2) was provided by Samsung Cheil Industries (Seoul, South Korea).

2.2 Electrospinning

Solutions of ten weight percent polyacrylonitrile (MW = 150 kDa) in N,N dimethylformamide and various weight percent titania nanoparticles were prepared and heated at 100 C for 24 h. Monoaxial nanofibers were generated using a syringe pump (Harvard Apparatus PHD 2000 Infusion, Holliston, MA) flowing at 0.03 mL/min through a 22 gauge needle (Hamilton N722, Reno, NV). The electric field was generated by a 15 kV electric charge and a 15 cm tip to collector plate distance. Coaxial nanofiber samples were generated using concentric needles (Scheme 2.1), inner of 24 gauge and outer of 18 gauge, with an inner/outer flow rate ratio of 2/3. The amount of components in each solution and the spinning conditions are listed in Table 2.1

Table 2.1 Uniaxial and Coaxial Electrospinning of PAN/TiO_2 Solutions

spinning type	sample code	PAN / TiO_2 (w/w)	solution flow rate (mL/min)	needle diameter (mm, I.D.)
Uniaxial	*U*-0	1 / 0	0.03	0.41
	U-1	1 / 0.2	0.03	0.41
	U-2	1 / 0.5	0.03	0.41
Coaxial	*C*-1	Core: 1 / 0	Core: 0.010	Core: 0.31
		Shell: 1 / 0.3	Shell: 0.015	Shell: 0.84
	C-2	Core: 1 / 0	Core: 0.010	Core: 0.31
		Shell: 1 / 0.5	Shell: 0.015	Shell: 0.84

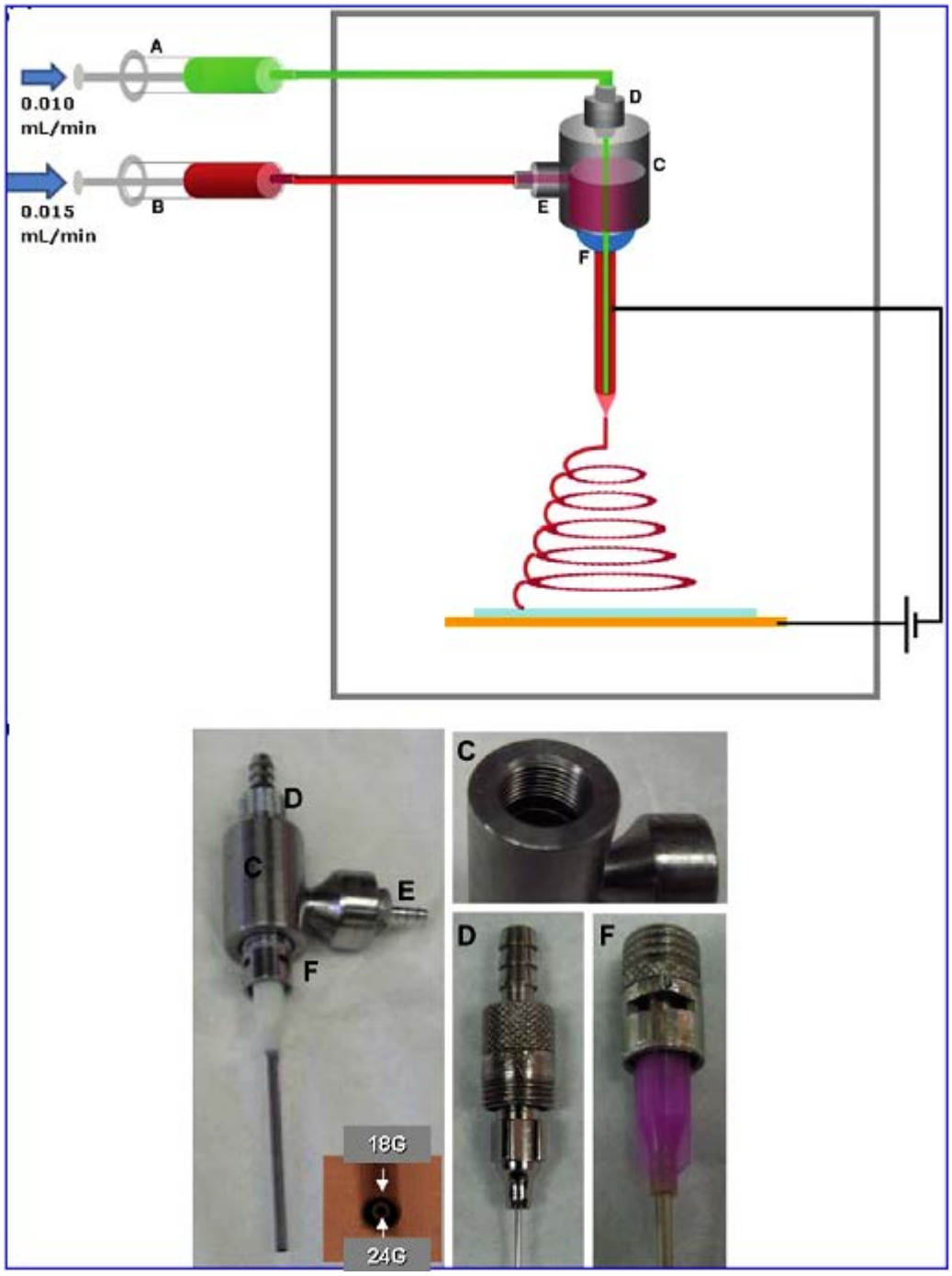

Scheme 2.1 Coaxial Electrospinning Setup

2.3 Fiber Characterization

For scanning electron microscopical analysis, electropsun fibers were mounted on aluminum microscopy stubs using carbon tape. The specimens were coated with gold-palladium (Au-Pd) for 30 s using an Edwards Auto 306 High Vacuum Evaporator (Edwards High Vacuum International, Wilmington, MA). Fiber morphology and TiO_2 particle distribution were observed using a Field Emission Scanning Electron Microscope (FESEM) – Hitachi 4500 (Tokyo, Japan). Backscattered electron (BSE) imaging and subsequent energy dispersive X-ray (EDX) analyses were conducted using a Scanning Electron Microscope- JEOL model XA-8900R superprobe (JEOL Ltd., Tokyo, Japan) equipped with a Tracor Northern Flextran Series-II Energy Dispersive X-ray Analyzer (Middletown, WI). All the electron microscopy images were obtained with an accelerating voltage of 10 KeV. The specimen current in backscattered electron imaging was 5.0 nA. It was necessary to use EDX analysis to identify TiO_2 in the fiber mat, putting the X-ray spot probe on a location of interest for 30 s with respect to the energy at 4.5 KeV of Ti. Analysis of these data allowed comparisons of TiO_2 nanoparticles at different locations on the fiber.

Sample preparation for the electron microscopy analysis of the fiber cross-section involved embedding the electrospun fiber mat. Epo-fix embedding resins A (1232-R) and B (1232-H) obtained from Electron Microscopy Sciences (Hatfield, PA) were mixed together in a mass ratio of 5:1 and transferred to silicone rubber molds (EMS, Hatfield, PA) where fibers aligned and fixed with two pins at both ends in the resin matrix (Scheme 2.2). After curing in an oven at 70 ˚C for 15 h, the embedded fiber was then sectioned vertically in a

transverse direction at room temperature, using an ultra-microtome with a diamond knife, into slices 60-80 nm thick.

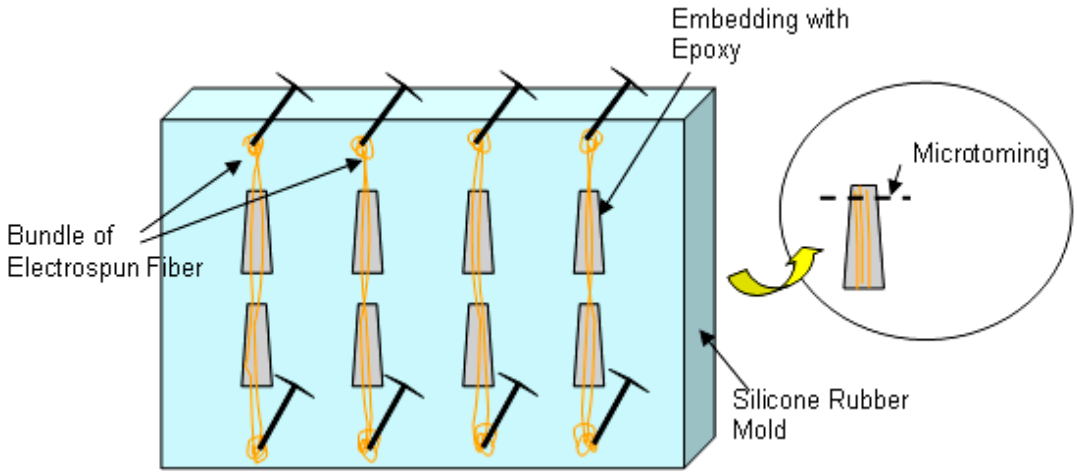

Scheme 2.2 Embedding and Microtoming for SEM Analysis (Cross-Section of Electrospun Fiber)

Elemental analysis was performed by X-ray photoelectron spectroscopy (XPS) (Surface Science Instrument, Model SSX-100, Mountain View, CA) with operating pressure < $2x10^{-9}$ Torr and monochromatic AlK_{α} X-rays at 1486.6 eV. Photoelectrons were collected at an angle of 0^{o} from the surface normal of samples, and the analysis depth was 27 nm from the surface. The area by X-ray beam spot was about 1 mm diameter on the nanofibrous mats film. Survey scans were conducted with an 150 V pass energy.

2.4 Photodegradation of Aldicarb Solution

Photo-oxidation experiments were conducted with the electrospun PAN nanofibers containing varying amounts of TiO_2. A solution for the decontamination test was made with 2 mM aldicarb, a carbamate pesticide chemical, in HPLC grade water. A nanofiber mat 10 (±0.01) mg was submerged in each 5 mL-aqueous aldicarb solution. After sonication in an ultrasonic bath for 5 min to distribute the fibers uniformly and remove air bubbles from solution, test tubes containing contaminated solution with electrospun nanofibrous web were placed in an ultra-violet (UV) chamber and exposed to UV radiation for 1, 2 and 3 h. The chamber had fixed 8 UV lamps (350 nm wavelength, 4 watt, 3 inch tall each) on wall side and a rotating sample holder with 2.5 cm distance between sample and lamp.

Following the photoreaction, the specimens were centrifuged with a force of 1,400 gravity (5-cm rotating radius at 5,000 rpm) for 3 min; the supernatant was filtered through a disk type syringe filter (Alltech Assoc. Inc., Deerfield, IL) with 25 mm diameter consisting of 0.2-μm pore size nylon membrane in order to remove particles and fibrils and then placed a 2-mL HPLC vial. Photodegradation activities of the electrospun fibers were measured by analyzing the concentration of aldicarb in each treatment solution of 1.5 mL using HPLC (Agilent 1100, Santa Clara, CA) with method conditions: 15 ˚C, C18 column, 60% acetonitrile / 40% water (pH-3 using H_3PO_4), 220/4 detector (DAD), flow rate 1 mL/min, with detection for 15 min.

3. RESULTS AND DISCUSSION

3.1 Fiber Characterization

Fibers were electrospun from five PAN-TiO_2 solutions (Table 2.1). Both uniaxial and coaxial electrospun fibers had average diameters in the range of 0.8 to 0.9 µm except *C*-2 while the higher TiO_2 content coaxially spun fiber showed 1.9 µm average diameter (Figure 2.1). In *U*-2 and *C*-2 (Figure 2.1a and 2.1b), some beaded fibers were observed as they had higher amounts of TiO_2 in the fibers. The morphology of co-axially electrospun fiber containing 33wt% of TiO_2 (sample code: *C*-2) is shown in Figure 2.1e. The fiber has irregular surface and observable nanoparticles which are embedded and exposed on the surface with diameters in the range of 20 to 50 nm. The areas with higher intensity of secondary electron scattering were investigated with X-ray microanalysis. This electron microprobe analysis confirmed that these regions on the fiber surface contained titanium (Ti) element with energy at 4.5 KeV while there was no Ti observed for the background regions of the fiber surface. XRD patterns shown in Figure 2.2 presented consistent characteristics of TiO_2 particles. TiO_2 powder that we used exhibited typical peaks of anatase crystal structure (Figure 2.2c) that were also observed in electrospun PAN-TiO_2 fibers (Figure 2.2a and 2.2b).

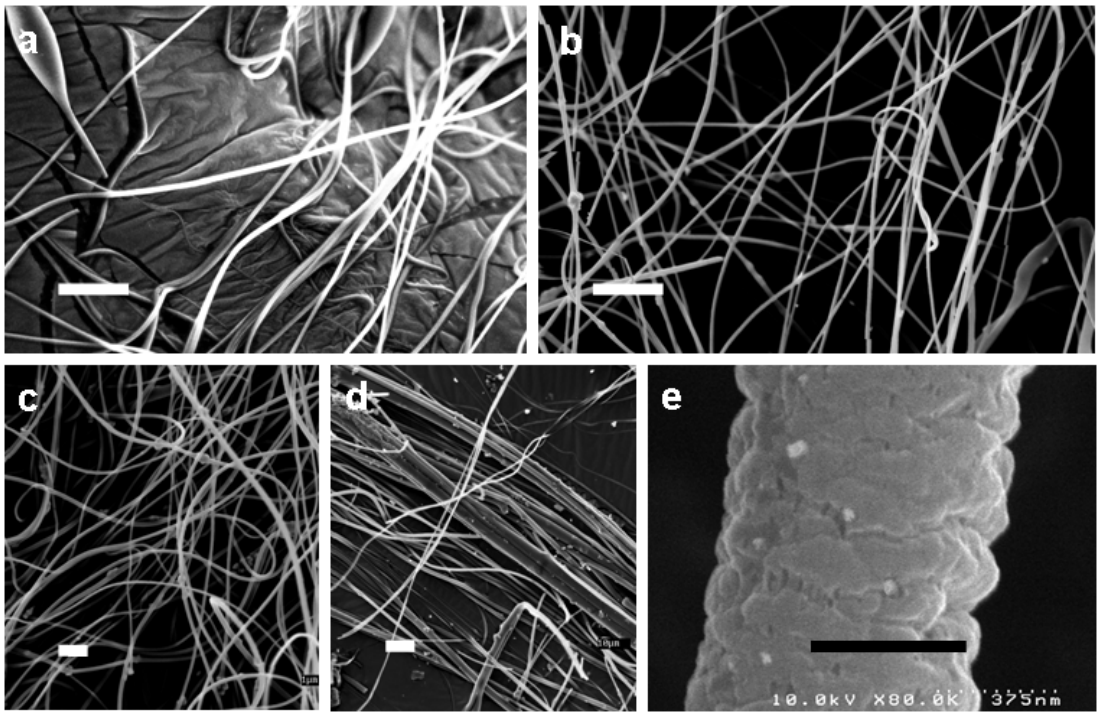

Figure 2.1 SEM Images of Electrospun PAN Fiber containing TiO_2 Nanoparticles; (**a**) *U*-1 with an average diameter 0.9 µm (range = 0.6 to 3.2 µm), (**b**) *U*-2 with an average diameter 0.8 µm (range = 0.4 to 1.5 µm), (**c**) *C*-1 with an average diameter 0.8 µm (range = 0.5 to 1.5 µm), (**d**) *C*-2 with an average diameter 1.9 µm (range = 0.4 to 17.6 µm), (**e**) Secondary electron image of *C*-2 single fiber, white scale bar = 10 µm and black scale bar = 0.5 µm

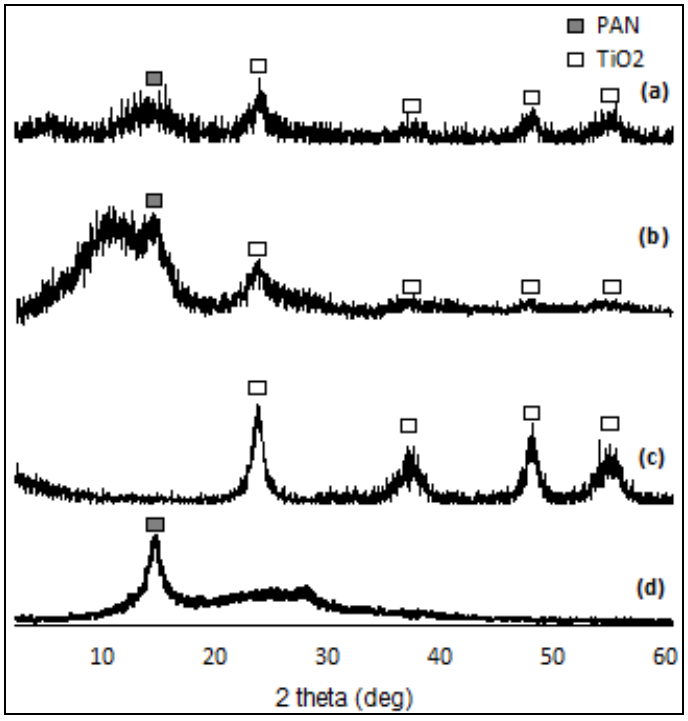

Figure 2.2 X-ray Diffraction Patterns (a) Electrospun Fiber *U*-2; (b) Electrospun Fiber *U*-1; (c) TiO_2 Powder; (d) PAN Powder

X-ray microanalysis spot probes for cross-sectional specimens of fibers were also conducted (Figure 2.3 and 2.4). The results of cross-sectional X-ray microanalysis confirmed there is a structural difference between the uniaxial and coaxial electrospun fibers. For the uniaxially electrospun fiber, TiO_2 particles were uniformly dispersed (Figure 2.3). For coaxial spun fiber, Ti was observed at locations close to the surface (Figure 2.4; point 1, 2 and 5), while the locations near the center of cross- section did not show any Ti signal (Figure 2.4; point 3 and 4).

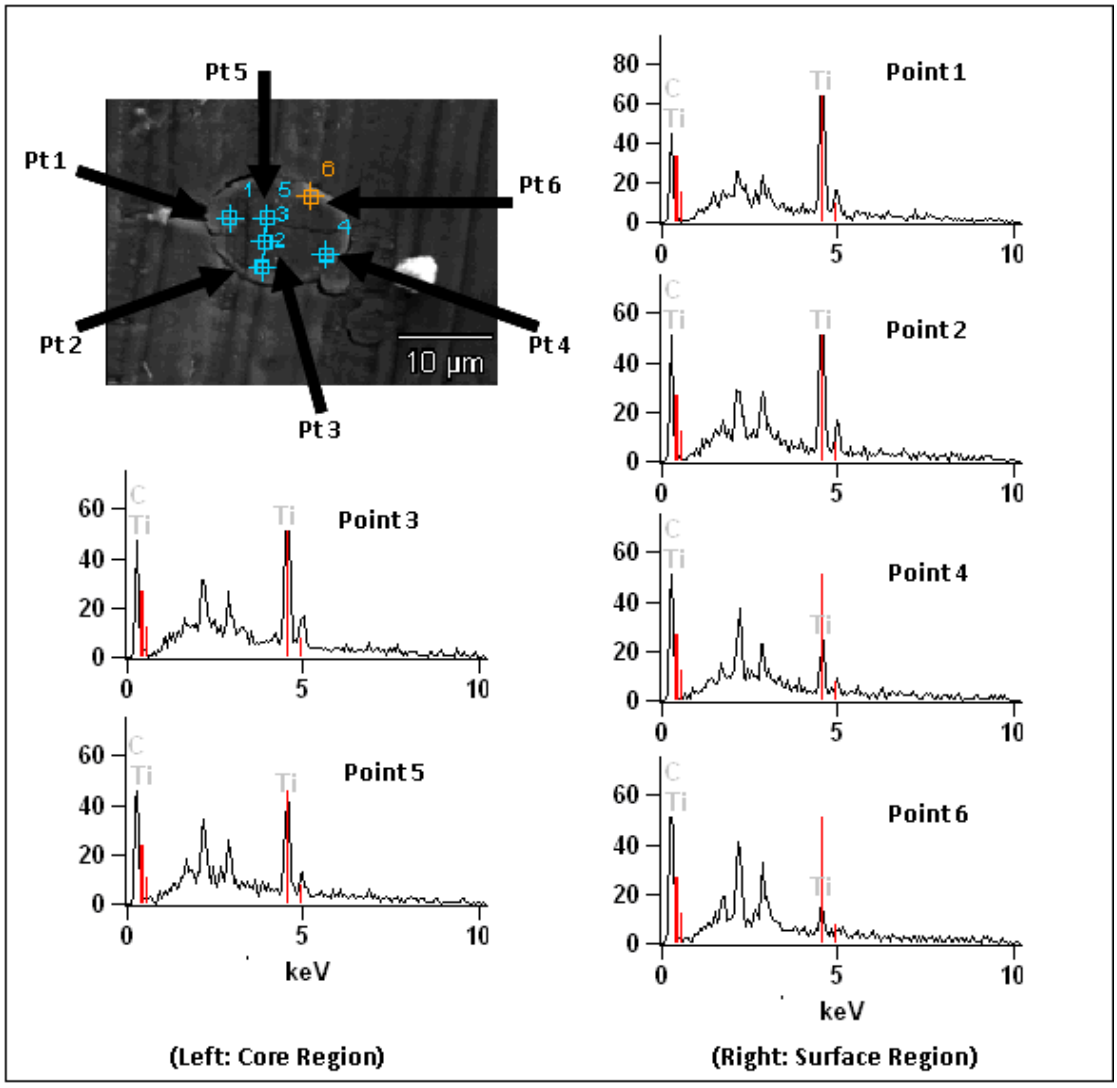

Figure 2.3 Secondary Electron Cross-section Image and Electron Microprobe Analysis of Uniaxially Electrospun PAN-TiO_2 Fiber

These results demonstrated that coaxial electrospinning formed bi-component, core-sheath fiber structure with TiO_2 particles located in the sheath. In the Figures 2.3 and 2.4, the peaks of gold (Au) are due to the Au-Pd sputter coating on the fiber specimen used to reduce charging in the electron microscope. We note that fibers with very large diameter (~ 10 µm) were

selected for both cases to be able to probe spatial distribution of TiO_2 particles because of the limitation of the interaction volume of backscattered electron beam in microprobe analysis (Scheme 2.3).

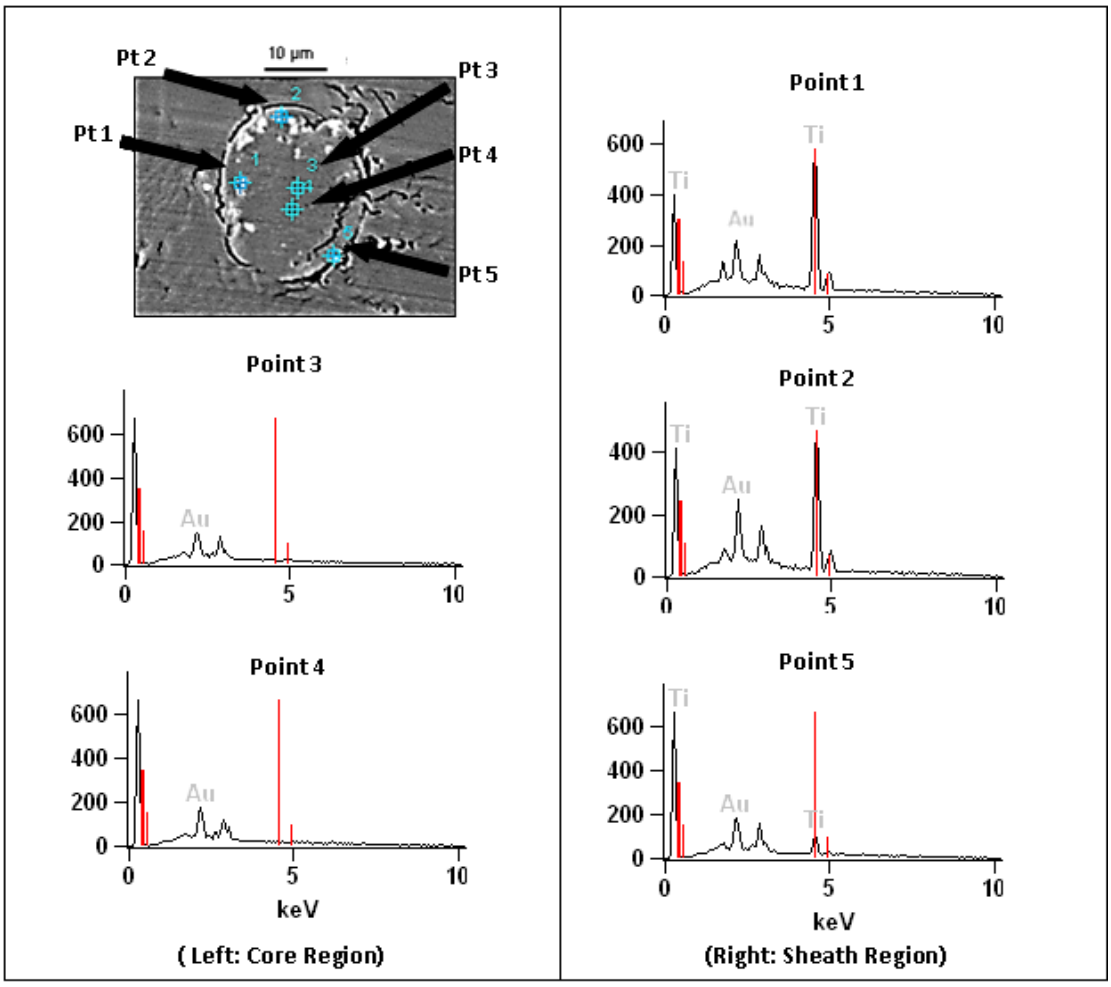

Figure 2.4 Secondary Electron Cross-section Image and Electron Microprobe Analysis of Coaxially Electrospun PAN-TiO_2 Fiber; Point1, 2 and 5: Surface Region (sheath), Point 3 and 4: Center Region (core)

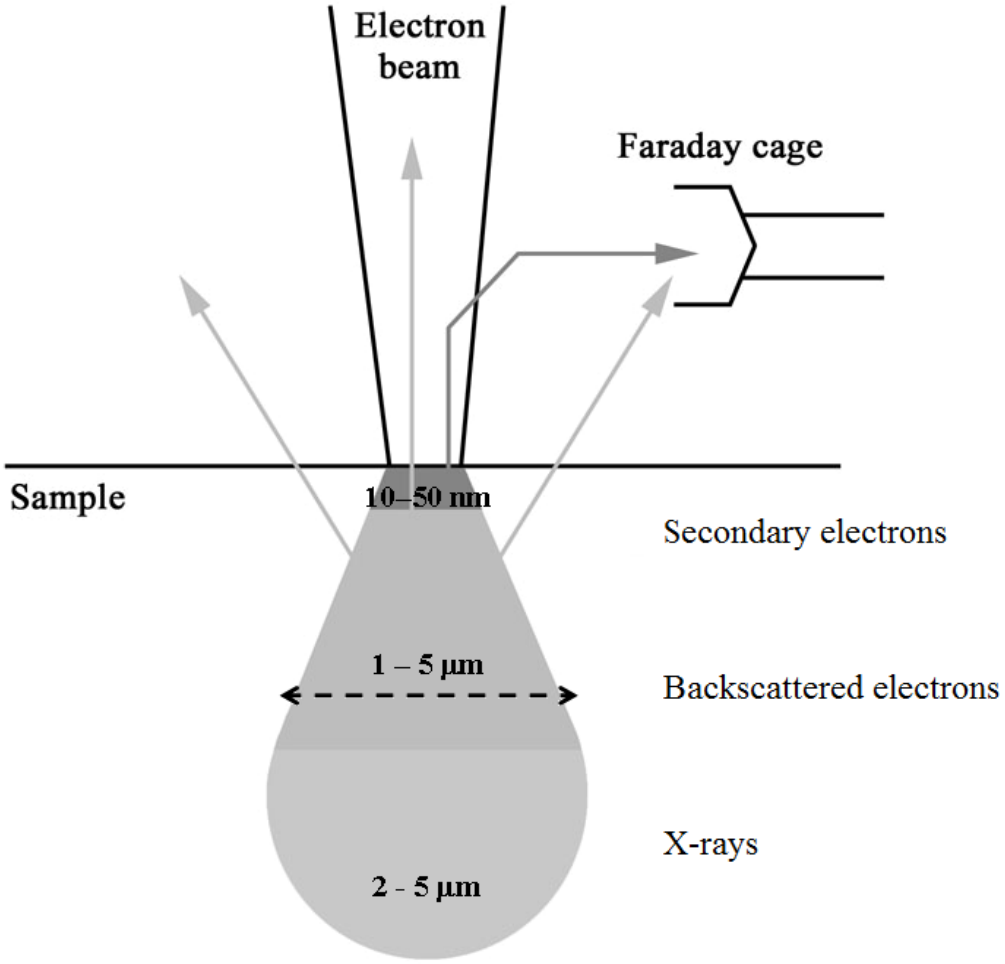

Scheme 2.3 Interaction Volume of Electron Beam

X-ray photoelectron spectroscopy (XPS) analysis presented elemental contents in a region from the surface to 27 nm depth of the nanofibers. The main elements (C, O, N and Ti) of PAN and TiO_2 were characterized. Ti (2p) was observed, but (1s) peak was not, which the oxidation states of TiO_2 in both samples had no difference. The atomic intensity ratio of Ti/N (Table 2.2), a normalized relative intensity of Ti in PAN-TiO_2 fiber showed that uniaxial nanofiber containing 33% TiO_2 had a significantly lower amount of titanium in the surface region than coaxial fiber with the same total TiO_2 content. The result is in good agreement with the cross-sectional morphologies of energy dispersive spectroscopy in Figures 2.3 and 2.4. Furthermore, this method substantiates the overall characteristic that there are more TiO_2 particles existing on the surface of coaxial fiber than that of uniaxial for the nanofiber mats (Table 2.2).

Table 2.2 XPS Result for Uni and Coaxial PAN-TiO_2 Fibers Containing 33 % TiO_2

Atom	Atomic %	
	Uniaxial	Coaxial
C	77	76
O	3	6
N	20	18
Ti (2p)	0.059	0.279
Ti/N	0.003	0.015

3.2 Photocatalytic Degradation

In HPLC analysis, PAN-TiO_2 nanofiber exhibited photocatalytic degradation of aldicarb (Figure 2.5). The amount of aldicarb (I in Figure 2.6) with the retention time of 8.8 min decreased over time, while those of other two products increased over the degradation time of 3 h. According to another study [19], the other two compounds (II and III) with the time of 5.1 and 7.3 min in Figure 2.5 and Table 2.3 were observed in the photo-oxidation pathway of aldicarb (Figure 2.6).

Table 2.3 Aldicarb and the Oxidized Derivatives

Compound	Common name	Compound in Figure 2.6	MW (g/mole)	Retention time in HPLC (min)
propanal, 2-methyl-2(methylthio)-, O-[(methylamino)-carbonyl] oxime	Aldicarb	I	190	8.8
propanal, 2-methyl-2(methylsulfonyl)-, O – [(methylamino)-carbonyl] oxime	Aldicarb sulfone	II	222	7.3
2-propenal, 2-methyl-, O-[(methylamino) carbonyl] oxime	--	III	142	5.1

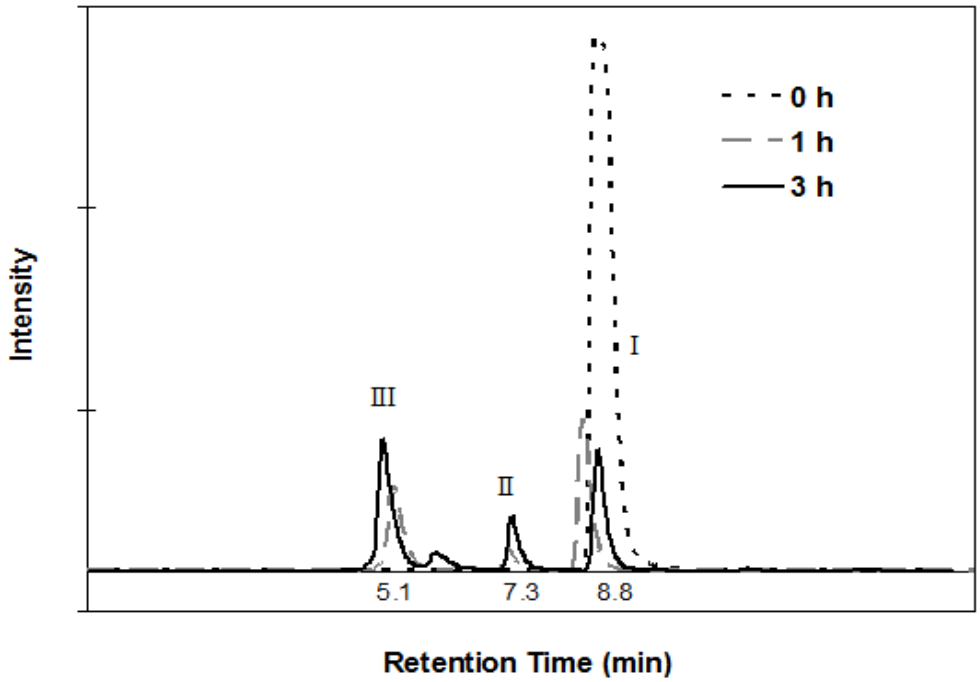

Figure 2.5 HPLC Chromatogram showing Concentration Change of Aldicarb and Oxidized Products by PAN-TiO_2 Fiber

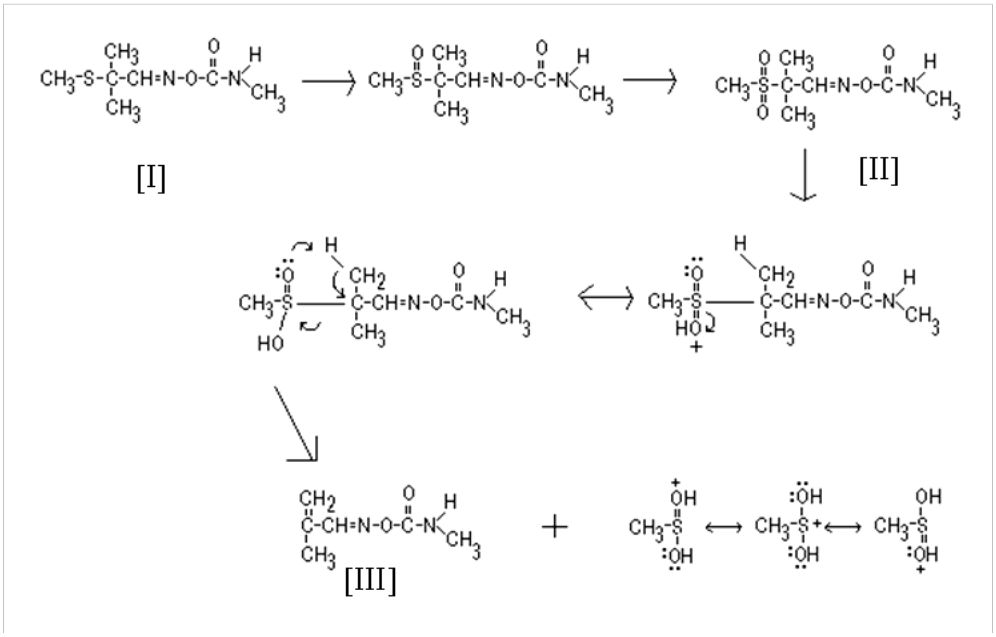

Figure 2.6 Oxidation Pathway for Aldicarb [19]

All fiber mats exhibited decrease of aldicarb over time (Figure 2.7). In particular, it was observed that the fiber containing higher content of TiO_2 degraded more aldicarb for both uniaxially (Figure 2.7a) and coaxially (Figure 2.7b) electrospun fibers. Over all, such photocatalytic properties of the TiO_2-containing nanofibers were suggested to offer potential for application of these fibers for protective materials. While a difference in degradation activity between the uniaxial and coaxial fibers was observed, the initial degradation rate for uniaxial fiber was lower than that for coaxial. Degradation time to the half of the initial mass (1.9 mg) was approximately 1 h in coaxial fiber, whereas it was about 2 h in uniaxial (Figure 2.8). In terms of reaction rate, the decomposition rates of aldicarb for the first hour were 0.69 mg/h by uniaxial and 0.95 mg/h by coaxial fiber, respectively, i. e. coaxial fiber with TiO_2 located in the sheath degraded aldicarb faster than uniaxial fiber with the TiO_2 distributed through the fiber structure. Further analysis of reaction kinetics also indicated the unique characteristics of coaxial morphology. The correlation between concentrations and reaction time determines the order of reaction. The decrease in the concentration over time can be written as Eq. 2.1, where C is concentration of reactant and *k* is a reaction constant [24].

$$-\frac{d[C]}{dt} = k[C] \quad \text{or} \quad -\frac{d[C]}{[C]} = kdt \qquad \text{(Eq. 2.1)}$$

$$\ln[C] = -kt + \ln[C]_0 \qquad \text{(Eq. 2.2)}$$

Integrating equation 2.1 and applying initial concentration C_0 at t=0 yield equation 2.2. If the linear correlation exists between ln[C] and t, the rate constant k of the first-order reaction is obtained from the slope of the linear

regression. The second-order reaction has a linear correlation between 1/C and t, which is derived from the equation 2.3 and 2.4, the integrated form of Eq. 2.3.

$$-\frac{d[C]}{dt} = k[C]^2 \qquad \text{(Eq. 2.3)}$$

$$\frac{1}{[C]} = kt + \frac{1}{[C]_0} \qquad \text{(Eq. 2.4)}$$

All the concentration changes in the photocatalytic reaction were depicted in Figure 2.9 to confirm the order of reaction. In logarithmic concentrations as a function of time, concentration decrease by the uniaxial fiber followed the first-order reaction behavior presenting linear trends, which was in good agreement with literature on photocatalytic destruction of hydroquinone, benzoquinone, cathechol and toluene by anatase TiO_2 [20, 21, 23]. On the contrary, aldicarb degradation by coaxial fiber was observed to follow second-order reaction rather than first-order in the relationships of ln[c] vs time and 1/c vs time (inset) in Figure 2.9, which resulted from the higher initial degradation rate of coaxial fiber with selective particle locations.

Previous studies have shown that photocatalytic degradation using TiO_2, has factors influencing reaction rate of the degradation such as adsorption, initial concentration of solution, temperature, and some inorganic species presenting ions in the research of TiO_2 covered non-woven paper [25]. In other studies using a photoreactor containing TiO_2 suspension [26, 27], it appears that the degree of degradation of organic compounds was obviously affected by illumination time, recirculation flowrate, light intensity, amount of

photocatalyst, suspension pH and initial concentration. According to the previous studies, the reaction rates and the reaction order shown in this study were obviously influenced by the factors of amount of photocatalyst on the surface of fiber and diffusion of solution, resulting in collision of both molecules (TiO_2 and aldicarb). In other words, the difference of reaction order was related to the total photocatalytic activity contributed by diffusion of aldicarb solution through PAN matrix to TiO_2 and the probability of reaction between aldicarb and TiO_2. As the uniformly distributed fiber gave slower degradation rate due to the lack of TiO_2 particles near surface, the core-sheath morphological fiber generated a higher initial photocatalytic activity by the more particles near surface of fiber. However, the diffusion of aldicarb into the particles under the surface still took place in the photocatalytic reaction of uniaxial, leading to a steady first-order reation in uniaxial fiber and the simiar final concentration observed at 3 h reaction time (Figure 2.8), whereas a diffusion effect may not exist in further depth in coaxial one. Suppose the photocatalytic reaction follows the each regression curve of the result (Table 2.4), it is suggested that coaxially and uniaxially electrospun 33%-TiO_2 fibers and the membranes with them will give half-concentration time ($t_{1/2}$) of $1/(k[C]_0)$ and $(\ln 2)/k$, respectively, where $[C]_0$ is the initial concentration of toxin. The each rate constant (k) was calculated and listed in Table 2.4. From the reaction kinetics, it is demonstrated that location of TiO_2 close to the surface of the coaxial fiber determines the photocatalytic decontamination rate. And, the core-sheath structure obtained by coaxial electrospinning offers the potential of providing enhanced self-decontamination properties since the initial degradation rate is important in protective materials and kinetic transport studies of contaminants through human skin [22].

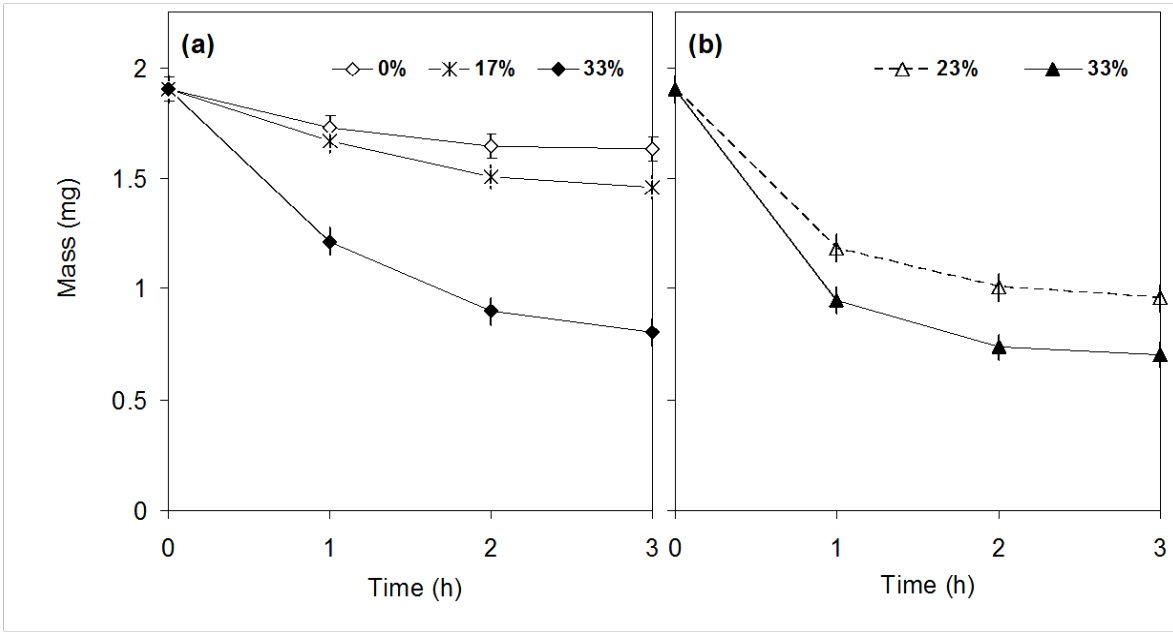

Figure 2.7 Photocatytic Degradation of Aldicarb by (a) Uniaxial; (b) Coaxial Electrospun Fiber Mats containing TiO_2 Nanoparticles

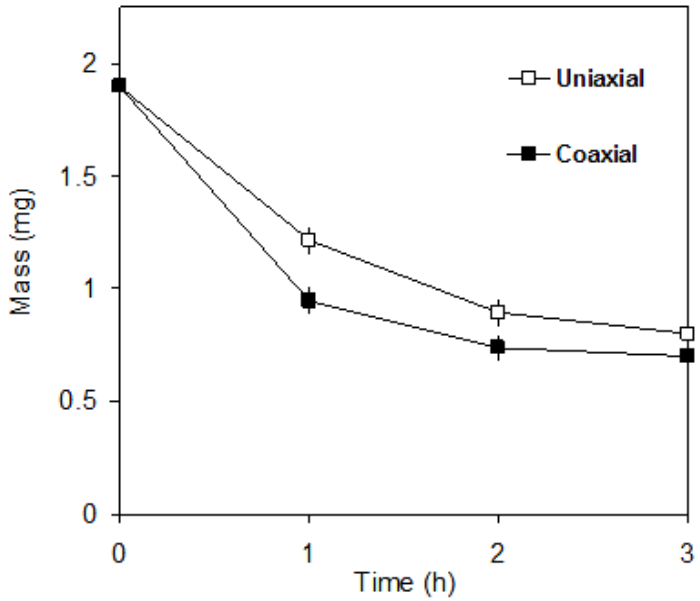

Figure 2.8 Photocatytic Degradation of Aldicarb; Uniaxial vs Coaxial Electrospun Fibers containing 33% TiO_2

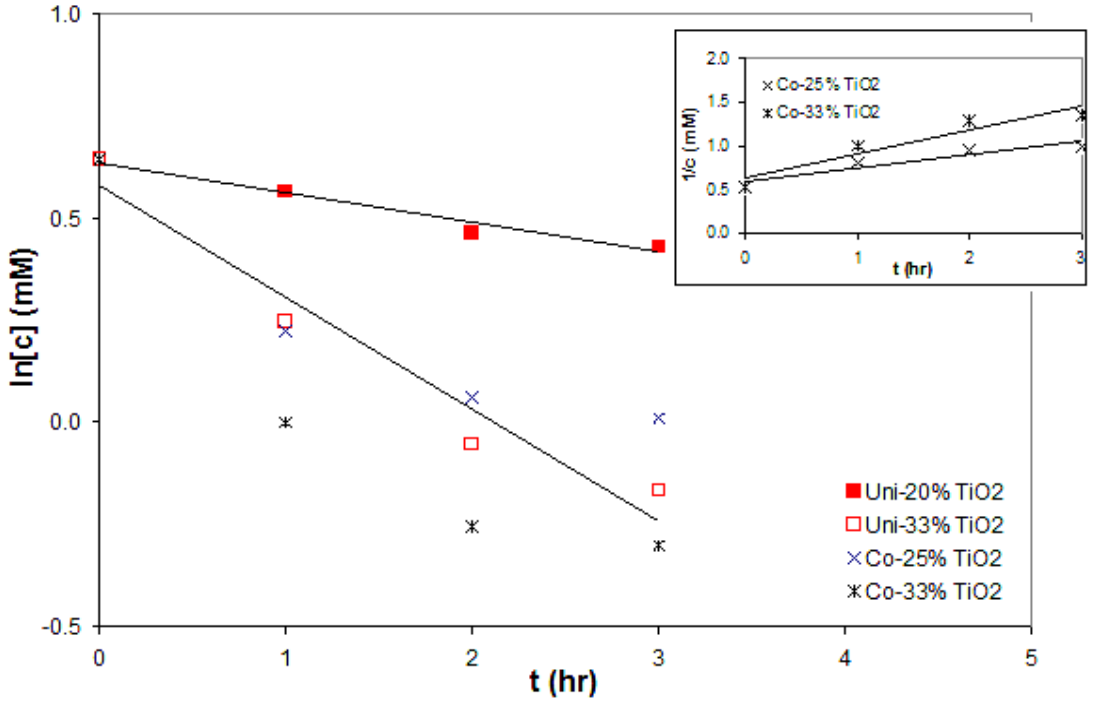

Figure 2.9 Photocatytic Degradation of Aldicarb ; First-Order Reaction and Second-Order Reaction (Inset)

Table 2.4 Rate Constant of Photocatalytic Reaction

Samples	1st-order		2nd-order	
	k (s^{-1})	R^2	k (mol^{-1} s^{-1})	R^2
Uni-33% TiO_2	7.6 x 10^{-5}	0.95	--	--
Co-33% TiO_2	8.6 x 10^{-5}	0.84	7.7 x 10^{-2}	0.90

k: Rate constant, R^2: Coefficient of determination, k and R^2 were calculated using the least squares regression function in MS Excel 2003.

4. CONCLUSIONS

PAN/TiO_2 electrospun nanofibers using uniaxial and coaxial methods were investigated as self-detoxifying materials comparing the detoxification activities of the photocatalyst in different fiber morphologies. It was demonstrated that the coaxial approach resulted in a bi-component core-sheath fiber structure with TiO_2 particles located in the sheath, while overall distribution of TiO_2 particles was obtained for uniaxial fiber. Photocatalytic activity of the fibers under UV irradiations exhibited degradation of aldicarb. In terms of degradation kinetics, higher distribution density of TiO_2 particles in sheath region resulted in a higher initial degradation rate. The core-sheath morphological TiO_2 containing fiber showed the second-order reaction behavior in photocatalytic reaction with aldicarb, whereas uniformly distributed TiO_2 fiber was observed to follow first-order reaction. The effective degradation activity of the coaxial electrospun fibers showed potential for application of these fibers for a self-decontaminating material such as protective clothing and filter media.

REFERENCES

(1) Formenti, M.; Juillet, F.; Teichner, S. J. "Photo-oxydation ménagée de parafffines et oléfines sur anatase à température ambiante" *Cr Acad Sci C Chim* **1970**, 270, 138.

(2) Childs, L. P.; Ollis, D. F. "Is Photocatalysis Catalytic" *J Catal* **1980**, 66, 383-390.

(3) Blake, D. M. Bibliography of Work on Heterogeneous Photocatalytic Removal of Hazardous Compounds from Water and Air, NREL/TP-430-22197, National Renewable Energy Laboratory, Golden **1997**.

(4) Fujishima, A.; Honda, K. "Electrochemical Photolysis of Water at a Semiconductor Electrode" *Nature* 1972, 238, 37-38.

(5) Linsebigler, A. L.; Lu, G.; Yates, J. T. "Photocatalysis on TiOn Surfaces: Principles, Mechanisms, and Selected Results" *Chem Rev* **1995**, 95, 735.

(6) Liqiang, J.; Xiaojun, S.; Baifu, X.; Baiqi, W.; Weimin, C.; Honggang, F. "The preparation and characterization of La doped TiO_2 nanoparticles and their photocatalytic activity" *J Solid State Chem* **2004**, 177, 3375-3382.

(7) Yu, H.; Lee, S. C.; Ao, C. H.; Yu, J. "Low-temperature fabrication and photocatalytic activity of clustered TiO_2 particles formed on glass fibers" *J Cryst Growth* **2005**, 280, 612-619.

(8) Shchukin, D. G.; Ustinovich, E.; Sviridov, D. V.; Lvov, T. M.; Sukhorukov, G. B. "Photocatalytic microreactors based on TiO_2-modified polyelectrolyte multilayer capsules." *Photochem Photobiol Sci* **2003**, 2, 975-977.

(9) Masuda, Y.; Sugiyama, T.; Seo, W. S.; Koumoto, K. "Deposition Mechanism of Anatase TiO_2 on Self-Assembled Monolayers from an Aqueous Solution" *Chem Mater* **2003**, 15, 2469-2476.

(10) Baia, L.; Peter, A.; Cosoveanu, V.; Indrea, E.; Baia, M.; Popp, J.; Danciu, V. "Synthesis and nanostructural characterization of TiO_2 aerogels for photovoltaic devices" *Thin Solid Films* **2006**, 511/512, 512-516.

(11) Kobayashi, S.; Hanabusa, K.; Suzuki, M.; Kimura, M.; Shirai, H. "Preparation of TiO_2 Fiber in a Sol–Gel System Containing Organogelator" *Chem Lett* **1999**, 10, 1077.

(12) Lee, S. W.; Kim, Y. U.; Choi, S.-S.; Park, T. Y.; Joo, Y. L.; Lee, S. G. "Preparation of SiO_2/TiO_2 Composite Fibers by Sol-gel Reaction and Electrospinning" *Mater Lett* **2007**, 61, 889-893.

(13) Li, D.; Xia, Y. "Direct Fabrication of Composite and Ceramic Hollow Nanofibers by Electrospinning" *Nano Lett* **2004**, 4, 933-938.

(14) Loscertales, I. G.; Barrero, A.; Marquez, M.; Spretz, R.; Velarde-Ortiz, R.; Larsen, G. "Electrically forced coaxial nanojets for one-step hollow nanofiber design." *J Am Chem Soc* **2004**, 126, 5376.

(15) Sun, Z.; Zussman, E.; Yarin, A. L.; Wendorff, J. H.; Greiner, A. "Compound Core–Shell Polymer Nanofibers by Co-Electrospinning" *Adv Mater* **2003**, 15, 1929.

(16) Yu, J. H.; Fridrikh, S. V.; Rutledge, G. C. "Production of submicron diameter fibers from difficult-to-process materials by two-fluid electrospinning" *Adv Mater* **2004**, 16, 1562.

(17) McCann, J. T.; Li, D.; Xia, Y. "Electrospinning of nanofibers with core-sheath, hollow, or porous structures" *J. Mater Chem* **2005**, 15, 735-738.

(18) Kalra, V.; Lee, J. H.; Park, J. H.; Marquez, M.; Joo, Y. L. "Confined Assembly of Asymmetric Block Copolymer Nanofibers via Multi-axial Jet Electrospinning." *Small* **2009**, 5, 2323.

(19) Dixit, V.; Tewari, J.; Obendorf, S. K. "Fungal Growth Inhibition of

Regenerated Cellulose Nanofibrous Membranes Containing Quillaja Saponin" *J Chromatogr A* 2009, 1216, 6394.

(20) Sobczynski, A.; Duczmal, L.; Dobosz, A. "Photocatalysis by Illuminated Titania: Oxidation of Hydroquinone and *p*-Benzoquinone" *Monatsh Chem* **1999**, 130, 377-384.

(21) Sobczynski, A.; Duczmal, L. "Photocatalytic Destruction of Catechol on Illuminated Titania" *React. Kinet. Catal. Lett*. **2004**, 82 (2), 213-218.

(22) Obendorf, S. K.; Csiszar, E.; Maneefuangfoo, D.; Borsa, J. "Kinetic Transport of Pesticide from Contaminated Fabric Through a Model Skin" *Arch. Environ. Contam. Toxicol.* **2003**, 45, 283-288.

(23) Cao, L. ; Gao, Z.; Suib, S. L.; Obee, T. N.; Hay, S. O.; Freihaut, J. D. "Photocatalytic Oxidation of Toluene on Nanoscale TiO_2 Catalysts: Studies of Deactivation and Regeneration" *J. Catal.* **2000**, 196, 253-261.

(24) IUPAC Goldbook Definition (2ND edition) "Order of Reaction"

(25) Barka, N.; Qourzal, S.; Assabbane, A.; Nounah, A.; Ait-Ichou, Y. "Factors influencing the photocatalytic degradation of Rhodamine B by TiO_2-coated non-woven paper" *J. Photochem. Photobiol. A* **2008**, 195, 346–351.

(26) Laoufi, N.A.; Tassalit, D.; Bentahar F. "THE DEGRADATION OF PHENOL IN WATER SOLUTION BY TiO_2 PHOTOCATALYSIS IN A HELICAL REACTOR" *Global NEST Journal* **2008**, 10 (3), 404-418.

(27) Guettai, N.; Amar, H. A. "Photocatalytic oxidation of methyl orange in presence of titanium dioxide in aqueous suspension. Part II: kinetics study" *Desalination* **2005**, 185, 439-448.

CHAPTER 3

FABRICATION OF NANOCHANNELED FIBER AND THE APPLICATION TO SELF-DECONTAMINATION MEMBRANE

1. INTRODUCTION

Fiber and fabric substrates can continually provide active particles without a significant loss of particles for a stable immobilized structure compared with catalyst powders or conglomerate state. However, the reaction between a toxic compound and active particles on fiber occurs only on the surface of fiber or diffusible sites of the fiber. It means that fiber morphology could enhance diffusion of chemical toxins for better efficiency of self-decontamination. Coaxial electrospinning was studied in chapter 2; while monoaxial nanofibers exhibited the capability to support catalytic nanoparticles and prevent their aggregation, it is observed that there is a significant mass transfer limitation making any catalyst at the center virtually unavailable to destroy a toxic compound if these nanoparticles are located at the center of the electrospun fiber [1]. Further besides the surface location, deep and continuous pores may also make it possible to enhance permeation of the toxin from the surface of fiber.

In electrospinning process, porous morphologies have studied extensively; however, most of studies were related to pores that may not be interconnecting. In terms of penetration or surface reaction efficiency, connected pores and channels have significance as well as large surface area.

In particular, for the application of filter media such as filtration membrane or protective textile, fibrous membranes that have connected pores and ultrafine channels in fibers would present an effective large surface area in a microporous fibrous membrane. Such morphologies with co-continuous polymer blends in the electrospinning process were studied.

Cocontinuous structures of polymer mixtures created by interconnected blends have been investigated and reported [2-5]. Recently, the importance of interconnected microporous structures was also emphasized by researchers in the polymer field, and many intelligent techniques were invented to make such structures. Existing techniques able to realize this design concept include fiber bonding (nonwoven meshes) [6, 7], solvent casting/particulate leaching [8, 9], phase separation/emulsification [10, 11] and co-continuous melt blending [12-15]. These techniques have been found to be especially useful when dealing with polymers. In particular, co-continuous melt blending has been shown to be an extremely versatile technique; interconnected porous structures with controllable porosity, pore size and even pore size distribution can be generated with this method. As stated above, cocontinuous polymer blends have been studied in the type of melt blending using a compatibilizer or varing comonomer blocks. In this study, cocontinuous polymer blends in a noble solution process were used to form interconnected channels in the fibers by electrospinning. Instead of a compatibilizer, different ratios of two solvents were investigated to vary the solubility of each polymer to the binary solvent system as well as the miscibility of the polymer blend resulting in various morphology of fiber.

Solvent extraction experiments require one of the phases to be selectively removed from the sample. The degree of continuity of the extracted phase is calculated based on its initial mass and the change in mass during extraction using the following equation:

$$\varphi_i = (m_{i0} - m_{if}) / m_{i0} \qquad \text{(Eq 2.1)}$$

where φ_i is the degree of continuity of component i; m_{i0} is the mass of component i originally present in the sample, and m_{if} is the mass of component i present in the sample after extraction. The degree of continuity represents the fraction of the phase that is continuous. Samples in which each phase has a degree of continuity of 1.0 are completely cocontinuous. The primary advantage of solvent extraction is that it is an absolute measurement. The degree of continuity gives a direct measure of the connectivity of each phase for a given composition. Other methods of detecting cocontinuity, such as image analysis, electrical conductivity measurements, or rheological measurements, require measurements on blends of several compositions to determine the region of cocontinuity. This study attempted to build a poly (ethylene oxide) (PEO) / cellulose acetate (CA) bicomponent blend in a binary solvent system consisting of acetonitrile (An) and acetone (Ac). The polymer solution has been investigated to form a CA fiber with continuous channels and pores using selective dissolution. In order to explore the possibility of self-decontaminating membrane application, metal oxide particles embedded on the unique channeled fiber have been introduced and their decontamination activity at the fibrous membrane were studied.

Nanocrystalline materials exhibit a wide array of unusual properties and can be considered as new materials that bridge molecular and condensed matter. One of the unusual features is enhanced surface chemical reactivity toward incoming adsorbates. For example, nanocrystalline MgO, CaO, TiO_2, and Al_2O_3 adsorb polar organics such as aldehydes and ketones in very high capacities and substantially outperform the activated-carbon samples that are normally utilized for such purposes [16]. TiO_2 as a photocatalyst has been investigated for almost four decades [17]. Photoxidation, one of the unique features of this metal oxide, is a mechanism suggested to define the driving force of strong oxidation by such metal based inorganic catalysts [18]. While TiO_2 requires light irradiation sources like ultraviolet (UV) light, MgO does not need such a light source. Furthermore, self-decontamination mechanism of MgO is different with that of TiO_2. The metal oxide carries out a degradation followed by the cleavage of the P-S bond or P-O bond of organophosphates, the most typical structure of warfare nerve agents. It is reported that MgO is very effective to decompose organophosphorus compounds [19, 20]. Therefore, nanocrystalline MgO is able to hydrogen bond with phosphorous compounds at room temperature with hydrolysis of the compounds occurring to produce surface bound species. Previously the decomposition of aldicarb (Figure 3.1b) by TiO_2 particles embedded in polyacrylonitrile fiber was examined. In the work described here, an analogous study of the organothiophosphate pesticide is described as a decomposition model compound. In this study, MgO particles incorporated in electrospun fiber with large surface area has been used to decontaminate methyl parathion, an organophosphate toxin (Figure 3.1a).

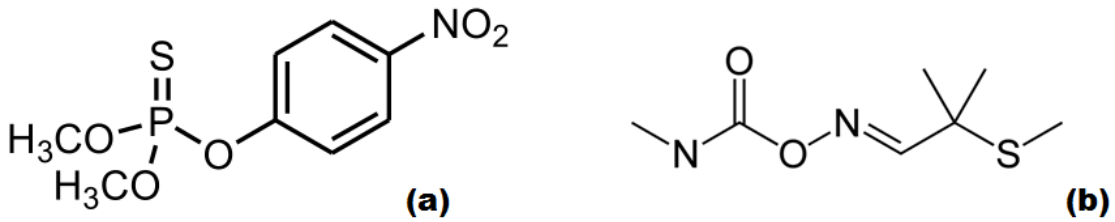

Figure 3.1 Decontamination Simulants; Methyl Parathion (a) and Aldicarb (b)[2]

2. EXPERIMENTAL SECTION

2.1 Materials

Poly (ethylene oxide) (PEO) (Mv: 200,000, Mn: 87,000, Sigma-Aldrich, St. Louis, MO), cellulose acetate (CA) (Mn: 30,000, acetyl content =39.8 wt%, Sigma-Aldrich, St. Louis, MO), HPLC-grade acetonirile (An) (99.9%, Fisher Chemical, Pittsburgh, PA) and acetone (Ac) (99.5%, Spectrum Chemicals, New Brunswick, NJ) were used in electrospinning solutions. The molecular weight of each polymer was characterized again by GPC to obtain comparable molecular weights. Methyl parathion, the pesticide, was purchased from Chem Service Incorporated (West Chester, PA). Methyl parathion (MP) is classified as an organophosphate, and its chemical name is O,O-dimethyl O-4 nitrophenyl phosphorothioate. The molecular weight is 263.23 g/mol with a chemical formula $C_8H_{10}NO_5PS$ [21]. Water (HPLC grade, Mallinck-rodt Laboratory Chemicals, Phillipsburg, NJ) and sodium hydroxide (Mallinck-rodt Laboratory Chemicals, Phillipsburg, NJ) were used without further

[2] Methyl Parathion: O,O-dimethyl O-4 nitrophenyl phosphorothioate
Aldicarb: (2-methyl-2(methylthio)propanal o-[(methylamino)-carbonyl] oxime

purification. Magnesium oxide (MgO) was purchased from NanoScale Corporation (Manhattan, KS). While several types were available, the form that was used in this study was the NanoActive Magnesium Oxide Plus particles (white powder, specific area: 600 m^2/g, crystallite size: 4 nm, mean aggregate size: 12 μm, bulk density: 0.4 g/cm^3, true density: 2.4 g/cm^3). The particles were vacuum dried for 24 h before using.

2.2 Solution Preparation

CA and PEO were selected as polymers for electrospinning of fiber materials. Their chemical structures are shown in Figure 3.2. In order to prepare CA/PEO blend solutions, acetonitrile (An) and acetone (Ac) were selected as solvents. Briefly, a 15 wt % CA solution in an An/Ac solvent mixture (An/Ac = 8/2 ~ 2/8, w/w) was prepared. After sonification of the CA solution for 1 h, PEO with 2/3 weight of CA was added into the CA solution under constant stirring to prepare the CA/PEO solution (CA/PEO = 60/40, w/w, 80/20, mole/mole). Then, a vial containing the solution (CA/PEO/An/Ac) was placed in a sonic bath at 45 °C for 2 h, the solution was stirred continually using a magnetic stirrer around 40 °C for 18 h. The main ratio of CA/PEO was 60/40 in weight (80/20, mole/mole) in the binary solvent (An/Ac = 20/80 ~ 80/20, w/w). MgO loaded solutions were prepared adding the nanoparticles with 10 wt% of polymer to the solvents prior addition of the polymers. After 20 min sonication of MgO particles in solvents, CA and PEO were mixed together and following the same procedures as used for the unloaded solution (containing no particles). Before electrospinning, the viscosity of solutions was measured using a rheometer (AR 2000; TA Instrument, New Castle, DE) at 25 °C.

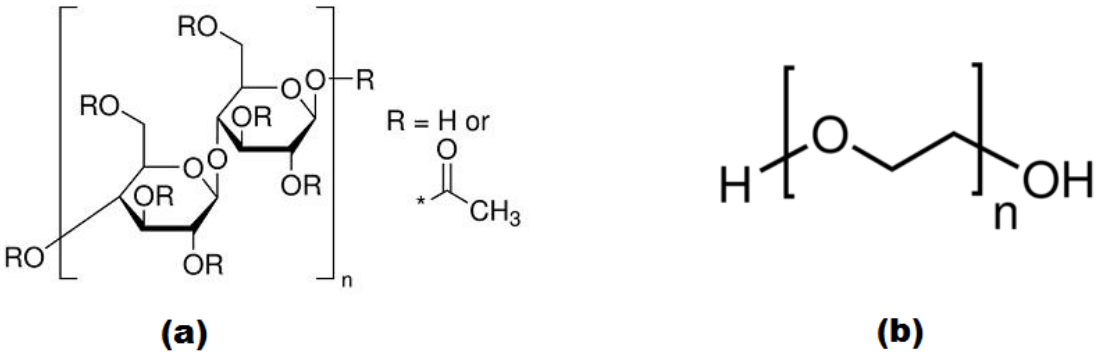

Figure 3.2 Structure of Cellulose Acetate (a) and Polyethylene Oxide (b)

The dissolution properties of acetonitrile and acetone are different for each polymer (CA, PEO). While CA is soluble in both acetone and acetonitrile, PEO is not very soluble in acetone in an ambient condition. However, in slightly higher temperature over 40 °C, PEO is also soluble in acetone. Both solvents do not have a highly hydrogen bonding strength. Acetone has medium and acetonitrile has poor H-bonding. Polyethylene oxide has low polarity compared to that of cellulose acetate (acetyl content=39.8%, degree of substitute=2.45). Further detail physical properties of polymers and solvents are listed in Table 3.1 and 3.2. All the solutions were checked and the turbidity to determine their phase region; single phase or two phase. The turbidity result was presented as a phase diagram.

Table 3.1 Properties of Solvents

Solvent	Acetonitrile (An)	Acetone (Ac)
Molar mass (g/mol)	41.1	58.1
Boiling point (°C)	81.6	56.2
Vapor Pressure (mm Hg, 20 °C)	73	184
Surface tension (dyn/cm, 20 °C)	29.3	23.7
Viscosity (cP, 25 °C)	0.343	0.308
Solubility parameter[a] (δ, MPa)$^{1/2}$		
δ_{total}	24.3	19.9
δ_P / δ_D / δ_H	18.0 / 15.4 / 6.1	10.4 / 15.5 / 7.0

a. δ_P: polar interaction, δ_D: dispersion force, δ_H: hydrogen bond

Table 3.2 Properties of Polymer

Polymer	Cellulose acetate (CA)	Polyethylene oxide (PEO)
Molecular weight (g/mol)	30,000 (M_n)	87,000 (M_n)
Transition temperature (°C)	67 (T_g)	65 (T_m)
Solubility parameter (δ, MPa)$^{1/2}$		
δ_{total}	25.1	20.0
δ_P / δ_D / δ_H	12.7 /18.6 / 11.0	3.0 / 17.3 / 9.4

T_g: glass transition temperature, T_m: melting temperature

2.3 Electrospinning

The solution was loaded into a 5-mL syringe for electrospinning. A syringe pump (PHD Ultra Pump; Harvard Apparatus, Holliston, MA) was used to infuse the polymer solution at speed of 0.04 ~ 0.08 mL/min through a stainless steel needle (Hamilton, Reno, NV) with an inner diameter of 0.016 inch (0.41 mm) and 0.023 inch (0.58 mm) (Hamilton N722 and N720, Reno, NV). A 16~18 kV voltage was applied between the needle and a circular metal plate (20-cm diameter) wrapped with aluminum foil. The distance between the needle and plate was maintained at 15 cm. Electrospun fibers were deposited on the plate forming a nonwoven nanofibrous mat. Experiments were conducted at room temperature. The collection time was approximately 1 h to fabricate a dimensionally stable and thick fibrous membrane. The obtained CA/PEO non-woven webs were detached from the collectors and dried under vacuum at ambient temperature overnight. For comparison purpose with electrospun CA/PEO fiber, a CA/PEO composite film was prepared by solvent-casting method from the as-prepared CA/PEO solution onto a glass dish. The thickness of the dry film was about 300 μm.

2.4 Selective Dissolution

After drying electrospun fiber mats, they were immersed in at least 80 °C HPLC grade deionized water for 10 h to remove PEO portion from the CA/PEO fiber. To avoid any structural damage to the fibrous mats during the process, the extraction was conducted in a soxhlet extractor maintaining the circulation of extraction hot water. The treated fibrous membranes were then dried for at least 6 h in a vacuum oven before characterization. The dried fiber

mass before and after the solvent extraction was monitored to give weight loss data for calculation of the degree of continuity for the PEO phase.

2.5 Deacetylation

After drying and mass analysis were complete, electrospun CA nanofibrous mats loaded and unloaded with MgO were immersed into a 0.05-M NaOH/ethanol solution for 3 h at room temperature, thus hydrolyzing cellulose acetate to cellulose [22]. The obtained regenerated cellulose webs were thoroughly rinsed in deionized water to remove any excess NaOH. Before drying the fiber samples, pH paper was used to confirm final neutralized pH after rinsing.

2.6 Fiber Characterization

The morphology of the fibers was observed with a scanning electron microscope (LEICA 440 SEM). The scanning electron microscopy analysis was followed as described in Chapter 2. Electropsun fibers were mounted on aluminum microscopy stubs using carbon tape. The specimens were coated with gold-palladium (Au-Pd) for 30 s using an Edwards Auto 306 High Vacuum Evaporator (Edwards High Vacuum International, Wilmington, MA). All the electron microscopy images were obtained with an accelerating voltage of 10 KeV. SEM images were process and analyzed by ImageJ (National Institute of Health, USA), an image analysis software utilized for measuring diameter of fibers.

Thermal properties of nanofiber membranes were evaluated using differential scanning calorimeter (DSC 2920; TA Instruments, New Castle, DE).

Samples of 4~10 mg were crimped in an aluminum sample pan. Each sample was scanned from 25 °C to 300 °C at a scanning rate of 10 °C/min under a nitrogen purge (99.99% pure). Thermogravimetry analysis was performed on a thermalgravimetric analyzer (TGA 2950; TA Instruments, New Castle, DE) to confirm the existence and amount of MgO in fiber after selective dissolution at a heating rate of 10 °C/min between 25 and 700 °C in air environment.

The Brunauer–Emmett–Teller (BET) surface area [41] and intro-pore size of the fibrous membranes were characterized by nitrogen adsorption isotherm data at 77K (liquid nitrogen temperature) using a surface area and porosity analyzer (Micrometrics, ASAP 2020). Prior to measurement, fibrous mat samples (50-100 mg) were cut into small pieces and placed in a narrow test tube followed by degassing for at least 12 h under vacuum at room temperature. BET surface areas were determined from 9-point adsorption isotherms that were completed in the 0.06-0.2 relative pressure range (p/p_0). Pore-size and the distributions were calculated from Barrett–Joyner–Halenda (BJH) desorption data in 0.02-0.99 relative pressure range (p/p_0) [42].

Fourier transformed infrared spectroscopy (FTIR; Thermo Nicolet MAGNA-IR 560, Wisconsin, MI) was used to confirm the chemical composition of electrospun fiber membranes determining conversion of cellulose acetate into regenerated cellulose. FTIR spectra were acquired in the frequency region of 4000 to 600 cm^{-1} at a 4 cm^{-1} resolution by scanning 3 replicates for 64 times at room temperature.

Wide-angle X-ray diffraction analysis (Theta-Theta Diffractometer, Scintag Inc., Cupertino, CA) was used to determine crystal structure, and to identify components of fiber composition with the 2 theta ranging from 30 to 50 degree.

2.7 MP Removal Test

The test method of removal of methyl parathion with MgO fiber followed the previous research of Lange L. E. in Professor K. Obendorf's group. Concentrations of MP were measured with a reverse-phase HPLC combined with a diode array UV-vis detector from the Agilent (Santa Clara, CA) HP series 1200. The injection volume was 20 μL. The set-up was run with an Agilent XDB-C18 reversed phase column with 5-μm particle size and 4.6 x 150 mm dimension and 25 °C. The mobile phase consisted of 50 % acetonitrile and 50 % water with 0.5 % formic acid, and the run time was 15 min. The UV-vis detector was set to scan at 280 and 320 nm.

Prior to the application of MgO loaded fibrous membrane to MP/hexane solution, standards of methyl parathion were run on the HPLC to compare the degradation products found in the MP/hexane solution. Methyl parathion standards were also used to normalize for any drift of the HPLC instrument. Differences in degradation of methyl parathion by the different fiber types were determined by exposing the fiber specimen to 20 mL of a 62.5 mg/L methyl parathion/hexane solution. Fiber samples containing an equivalent mass of 250 (± 1) mg were treated in a shaker for three reaction times (1, 10 and 100 min) with 3 replications. After the reaction time was complete, 1.5 mL of the hexane solution was taken with a syringe and filtered by syringe filter with 25 mm diameter consisting of 0.2-μm pore size (Alltech Assoc. Inc.,

Deerfield, IL) and then transferring the filtered solution to a HPLC vial. Each sample was then run on the HPLC.

Besides the solution-submerging experiment in a test tube, membrane filtration in a commercial filtration system (Sterifil® Funnel, Millipore) was performed as another measurement of decontamination efficiency. MP/hexane solutions of 200 mL with 62.5 mg/L concentration were filtered over an MgO loaded electrospun membrane with a filtration area of 13.8 cm^2 in a dead-end filtration cell. Prior to the membrane test, completely dried membrane samples with around 750 mg were placed on a filter support, and then sealed with a silicone o-ring (Figure 3.3). The experiment started after 3 min of conditioning time to stabilize the membrane for the contact with the MP/hexane solution. The test was conducted with a negative pressure of 2 in Hg from the bottom of membrane by a vacuum pump that was connected to a receive flask. The same as above process was repeated twice more using the filtered solution continuously to reduce the deviation of each filtration experiment. Three times fiber treated and filtered solutions through an MgO loaded membrane were collected to characterize MP concentrations by HPLC as described in a soaking test above.

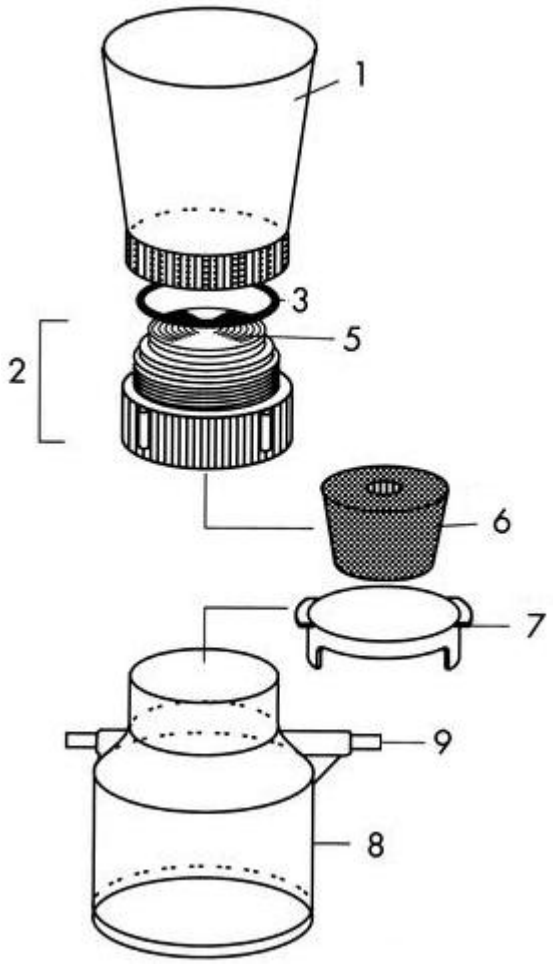

Figure 3.3 Membrane Filtration Setup and Parts
1) Funnel (Polysulfone)
2) Holder base
3) O-ring
5) Support screen for filter holder
6) Stopper (Silicone)
7) Receiver flask cover
8) Receiver flask
9) Vent (Vacuum connector)
http://www.millipore.com/catalogue/module/c171#1

3. RESULTS AND DISCUSSION

3.1 CA/PEO Solution in Ac/An Solvent

Electrospinning solutions were prepared varying the ratio of acetonitrile (An) and acetone (Ac) to investigate morphological effects of solvent component on cellulose acetate (AC)/polyethylene oxide (PEO) solution during the electrospinning. In Figure 3.4, solubility parameters (Table 3.1 and 3.2) of

polymers and solvents in this mixture system are drawn in two dimensions with hydrogen bonding and polar interaction component. For polymer CA, the solubility parameter of Ac is very close to that of CA, and within the interaction radius of CA. PEO also has a closer solubility parameter to Ac than An. With regard to the parameters, it was inferred that Ac dissolves both polymers more favorably than An.

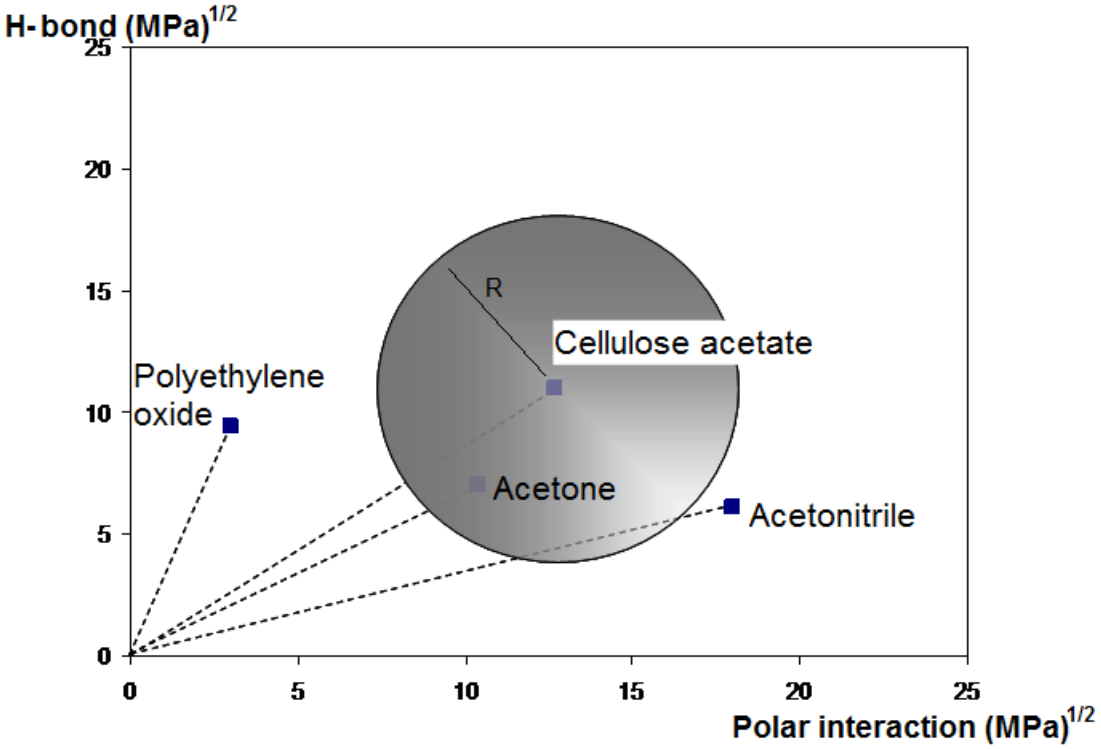

Figure 3.4 Sketch of Solubility Parameters in 2-Dimensions (R: Interaction radius of CA) [23, 24]

3.2 Fiber Diameter

Fiber diameter was a characteristic that changed when the ratio of the two solvents used in electrospinning was varied. Figure 3.5 and 3.6 showed that the diameter of electrospun fibers increased with increasing Ac content and increasing polymer concentration in solutions. The increase of fiber diameter with increasing polymer concentration obviously resulted from the greater feeding mass, larger initial jet radius and consequential higher viscosity enabling inability to maintain the flow of the solution, which was in good agreement with previous findings [40, 43], confirming that the concentration of a polymer solution is important for getting the right size of fibers. Highly concentrated polymer solution will produce large-diameter fibers, whereas decreasing the concentration to too low a level would result in small-diameter fibers. The concentration of a polymer solution depends on three factors, viscosity, surface tension and electric conductivity of the polymer solution. Dietzel *et al.* [46] demonstrated that solution surface tension and viscosity play important roles in determining the range of concentrations from which continuous fibers can be obtained through electrospinning. They pointed out that the fiber diameter increased with increasing polymer concentration according to a power law relationship. At low concentrations, beads are form instead of fibers, and at high concentrations, the formation of continuous fibers is prohibited because of the inability to maintain the flow of the solution at the tip of the needle, resulting in the formation of larger fibers. The concentration or the corresponding viscosity was one of the most effective variables to control fiber morphology. Demir *et al*. further found that the fiber diameter was proportional to the cube of the polymer concentration [70].

Figure 3.5 and 3.6 also showed the viscosity effect on the diameter increase with increasing the concentration of polymer.

While increasing polymer concentration was observed to have an obvious effect on high viscosity resulting in a large fiber diameter, the increase of fiber diameter with varying solvent ratio was contributed by several combined interactions such as polymer-solvent interaction and physical property of each solvent in the blend system. In different solvent ratios, the viscosity change was the most effective variable to control fiber morphology. It is suggested that varying the solvent ratio altered the nature of solvent, and solubility to CA/PEO blend as well, then final viscosity changed in the range of 60/40 – 20/80 An/Ac. In addition to the viscosity change, changes in charge density, electrical potential and vapor pressure were also suggested to affect the nature of the CA/PEO solution. Chowdhury *et. al* [43] observed that an adding ethanol on a PEO/water solution increased fiber diameter due to the increase of solvent viscosity resulting from both the increased disentanglement time of the transient entanglements and the poorer solubility of ethanol than water for PEO. Fong *et al.* [47] reported that fiber diameter and morphology changed from a beaded fiber gradually to ultrafine fibers on addition of ethanol, as ethanol is a solvent of PEO and its addition increased the solution viscosity. Wannatong *et. al* [48] found that fiber diameters decreased with increasing density and boiling point of the solvents in the study with polystyrene in different solvents, which was also observed in this study. Higher vapor pressure with increasing acetone may result in the rapid evaporation during the electrospinning, which blocked further elongation and diameter decrease. The overall behavior of diameter changes with solvent ratios demonstrated

that An/Ac solvent ratio affected CA/PEO polymer mixture solution and processing parameter enabling different fiber morphology during electrospinning. This was in agreement with previous observations. Choktaweesap *et. al* [49], observed that mixed solvent with acetic acid and several solvents affected the fiber morphology including diameter of gelatin compared with an acetic acid single solvent. In another investigation [50], CA was observed to be affected in fiber diameter and overall morphology by the mixed-solvent systems of acetone–DMAc, chloroform–methanol, and dicholoromethane-methanol compared with the individual solvents. In this study, besides fiber diameter, the further morphological effects by different ratios of mixed solvent will be discussed.

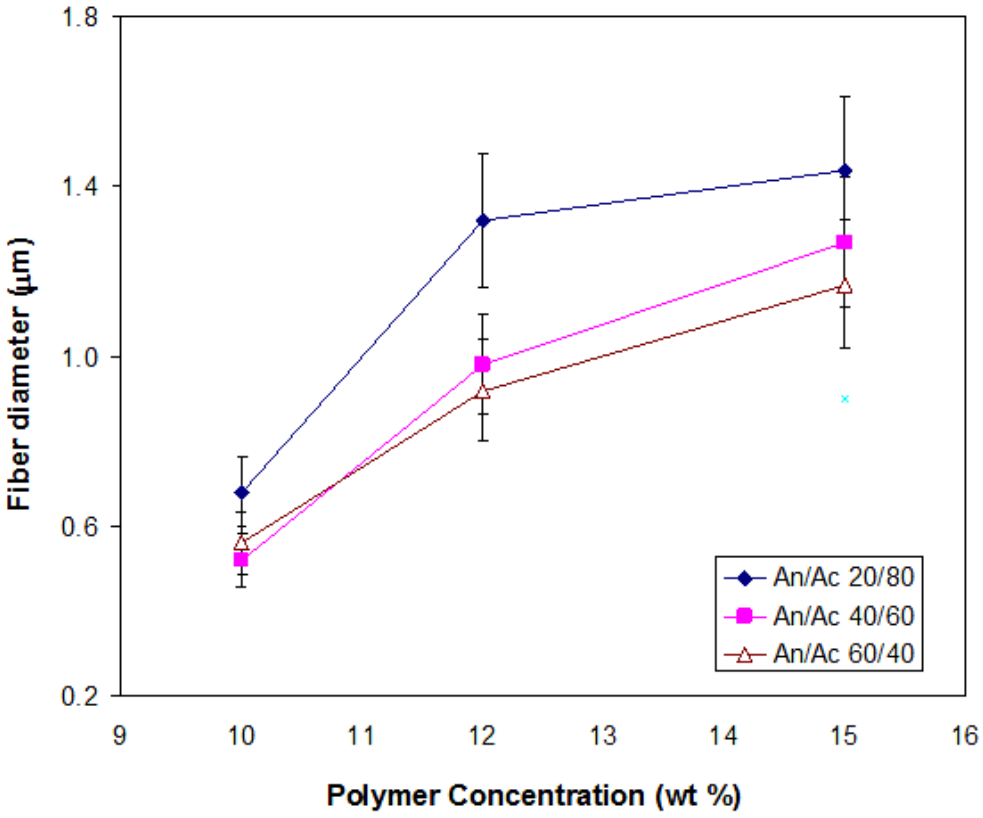

Figure 3.5 Electrospun CA/PEO Fiber Diameter with Polymer Content and Solvent Ratio (CA/PEO=75/25, mole/mole)

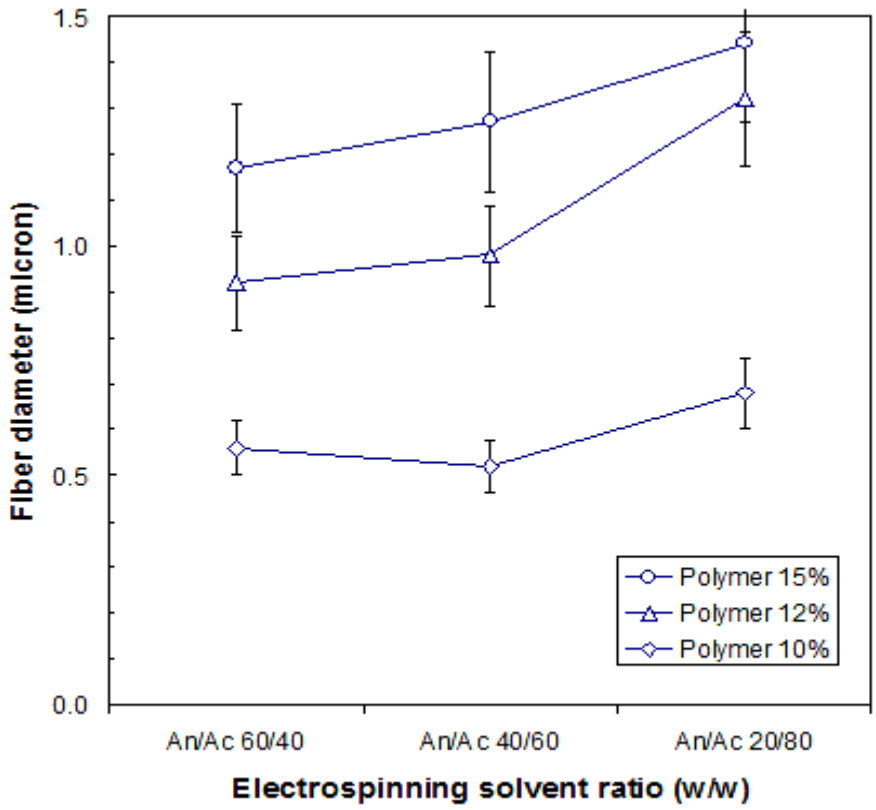

Figure 3.6 Electrospun CA/PEO Fiber Diameter with Solvent Ratio and Polymer Content (CA/PEO=75/25, mole/mole)

3.3 Phase Diagram

Electrospinning of polymer solutions involves rapid evaporation of the solvent as the jet surface increases sharply within milliseconds after its formation. During electrospinning, phase separation sets in as the solvent concentration is reduced so much that phase boundaries are crossed [25]. A time scale well below one second possibly down to the millisecond range characterizes the phase separation during electrospinning [26]. This has several consequences: The phase–separated regions are not able to grow prior

to solidification resulting in the preservation of very fine phase morphologies. A second consequence is that the tendency towards a spinodal (unstable homogeneous region) rather than a binodal (in between a two-phase metastable zone) phase separation will be enhanced since nucleation phenomena require more time to set in than the initial growth of unstable concentrations. Thus, we expected a certain preference for cocontinuous structures rather than matrix-domain phase morphologies in the polymer-solvent electrospinning system.

Phase diagrams for the mixture system in this study are displayed in Figure 3.7. The diagram that was obtained by turbidity measurements (Figure 3.8) shows the phase behavior of the blend solutions consisting of acetonitrile (An), acetone (Ac) and polymer mixture (CA/PEO). The polymer blend was considered one component that was fixed at the ratio of CA/PEO 60/40 in weights and 80/20 in moles. Before selecting suitable solutions for electrospinning, all solutions were reviewed in terms of viscosity and dissolution phase, and depicted in the diagram. It was obvious that solutions with high concentrations of solvent (bottom side of the phase diagram) were required in order to obtain homogeneous solutions providing freely dispersed polymers while solutions with high concentrations of polymer were observed to be more viscose. As some solutions having high polymer concentrations were ambiguous to determine as either one-phase or two-phase, such ones were denoted as coexistence solution. Finally, the phase diagram was obtained to show a small area of a clearly dissolved homogeneous one-phase solution region presenting around 18 wt% of polymer at the most. The reason for the limited single-phase area shaping a confined narrow region is certainly related

to the molecular weight of polymers in the study. For example, if lower molecular weight PEO than PEO (Mn: 87,000) in the study were used instead, the single-phase area would be much larger reaching over 20 wt % of polymer, resulting from the increase of polymer amount that would be dissolved. Since the shorter chains of polymer molecules would provide low viscosity and freely dispersed phase in blend, the MW decreasing could be another candidate way to investigate more diverse polymer blends of CA/PEO. And, it was also observed that acetone-rich area (right side) produced a slightly larger one-phase region, which means that acetone is more favorable to dissolve the CA/PEO mixture than acetonitrile. Figure 3.4 (solubility parameters) also indicated that acetone was anticipated to have higher solubility for the polymer mixture of CA/PEO. Thus, the highly dispersed polymer blend in strong solvents suggested the prediction of finer blend morphology and reduced disentanglement of molecules from the mixing state to phase separation, which will be described in further analysis.

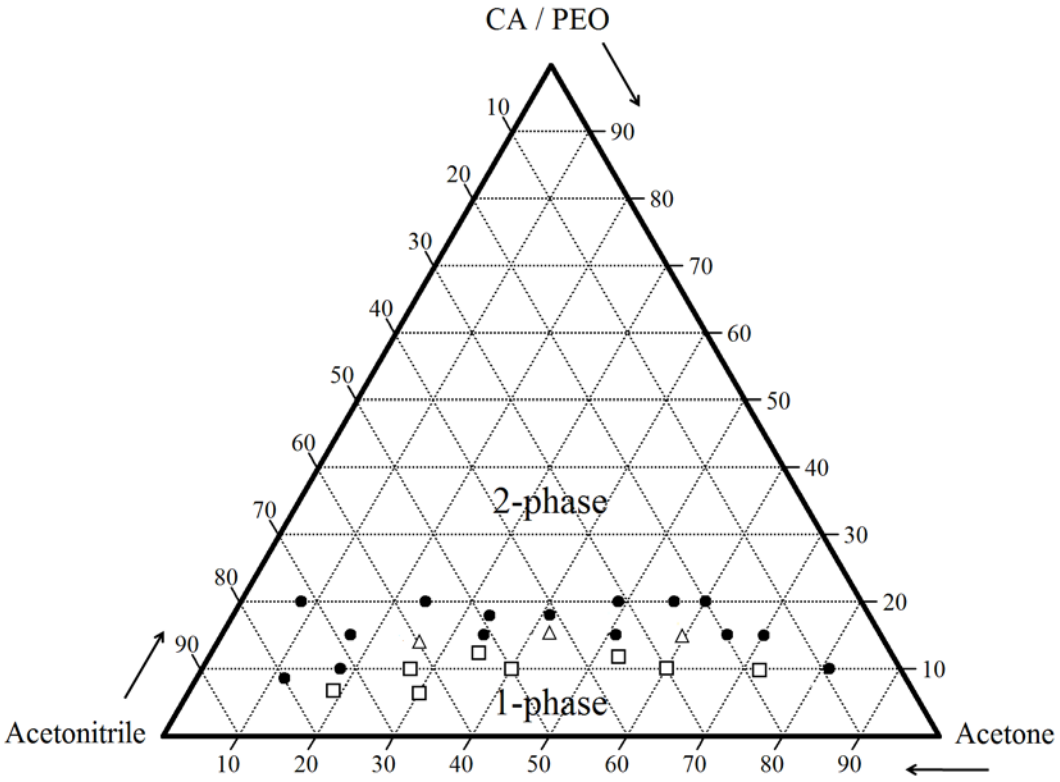

Figure 3.7 Ternary Phase Diagram (Solid circle: two-phase solution, Hollow square: single-phase solution, Hollow triangle: coexistence phase solution)

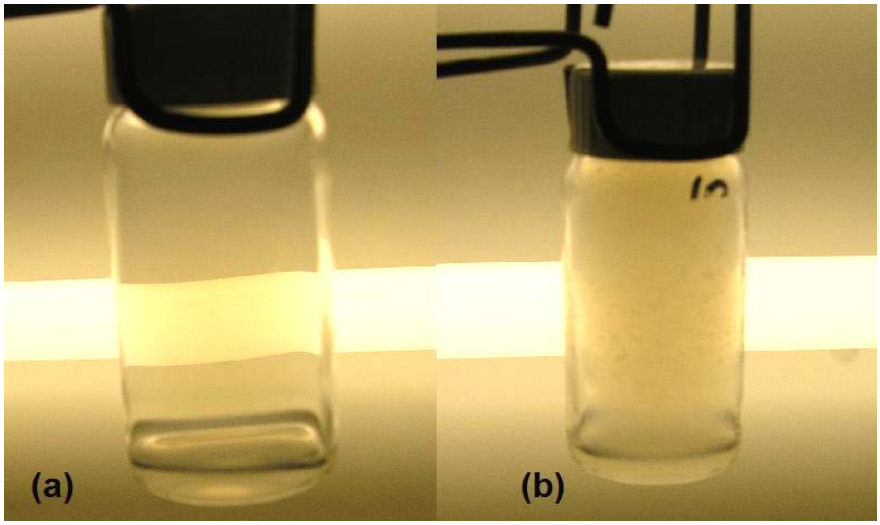

Figure 3.8 Turbidity of Polymer Solution: (a) One-phase, (b) Two-phase

The solution compositions used in the electrospinning experiment were not only of definite one phase region, but also adjacent to or on the phase boundary as well. This is because it is hard to say which phase is absolutely favorable to form a cocontinuous polymer blend during electrospinning. With regard to the growth of each polymer phase, the rapid phase separation at close to boundary region was more favorable than sufficient slow evaporation of low polymer concentration in the single phase. On the other hand, two phase region probably started to phase separation keeping polymer blend from continuous dispersion in a solution. Out of several solutions prepared varying the ratio of Ac/An and the total polymer contents, some of them seemed suitable in electrospinning, but some were not able to be electrospun due to the inappropriate solution properties such as too high or low viscosity at room temperature and insoluble components. Due to such limitation of experimental spinnability in electrospinning, certain selections were used in further studies as will be described.

3.4 Selective Dissolution and Mass Loss of PEO

Porous fiber morphology by selective dissolution was studied extensively. Here, we explored to form not only just porous fiber but also fibrous structure in which interconnected hollow spaces exist resulting from the cocontinuous polymer blend. The solubility of binary solvent consisting of acetonitrile (An) and acetone (Ac) was varied for the CA/PEO mixture of one composition (60/40 in weights, 80/20 in moles). In order to investigate the formation of PEO continuous structure within CA/PEO blended fibers, selective dissolution of PEO was performed using water as the extracting solvent. This was reported to be a very effective technique to obtain information on the

degree of continuity and microscopical analysis [27]. The mass changes of solvent extraction experiments are listed in Table 3.3. The degree of continuity of PEO was calculated from the mass difference before and after the solvent extraction; if the degree of continuity is close to unity, most of the contents are interconnected with a continuous structure. This was based on the assumption that water selectively dissolves PEO phase existing separated from CA phase.

The content of CA/PEO mixture was fixed at 15 wt% in solutions, and solvent ratios of An/Ac were varied in the range 30/70, 40/60, 60/40 and 70/30 with 85 wt% in solutions. After water washing, fiber from the solvent ratio of 60/40 An/Ac presented 0.77, the highest degree of continuity of PEO while other fibers showed from 0.11 to 0.61 of PEO continuity (Table 3.3). Figure 3.9 also compared the mass losses of CA/PEO fibers that were electrospun at different solvent ratios. The mass calculation was from the mass changes of entire fiber, not individual component in fiber. Based on the small change of CA in the extraction (Table 3.3), the mass loss of CA was not considered. The result of Table 3.3 and Figure 3.9 implied that there were optimum solubility and evaporation condition of solvent that enables the most continuous PEO structure at a certain CA/PEO blend ratio in electrospinning. With increasing acetone in electrospinning solutions (rightward in the phase diagram), the degree of continuity of PEO was more reduced (Table 3.3) than increasing acetonitrile. This tendency resulted from varying solvent-polymer interactions and polymer-polymer miscibility. Considering each solubility parameter in Figure 3.4, acetone-rich solvent was believed to favorably dissolve CA/PEO and make the blend more miscible and homogeneous phase with a longer radius of gyration rather matrix-domain type dispersion, thus,

leading to the limitation to bring rapid separation. In addition, the relatively high molecular weight of PEO may result in the disentanglement limitation in phase separation from the freely dispersed mixing state. Since polymers do not dissolve instantaneously, and the dissolution is controlled by either the disentanglement of the polymer chains or by the diffusion of the chains through a boundary layer adjacent to the polymer–solvent interface [44], the long chain of PEO molecules (Mn: PEO-87000, CA-30000) was suggested to bring the least mass loss and highest residue in the region of the acetone-rich solvent fiber when the selective dissolution of PEO by water. Compare with other similar investigations, the MW ratio in the study may have too low portion of PEO to CA (40 wt%, 20 mol%) to form a more interconnected cocontinuous polymer blend [51-59], which showed that a small region of stability of the gyroid structures (cubic bicontinuous blend) was found close to the ratio of 60/40 and 40/60 (v/v) between the lamellar and hexagonal regions in block copolymers and/or homopolymers/compatibilizer blend systems. A study on a polyethylene glycol (PEG)/cellulose acetate (CA) blend electrospun fiber [66] also suggested that a limitation of PEO extraction may exist in the current blend system. Finally, it was implied that the movement of the PEO distributed within the fiber was limited by the shield of the CA matrix, and the long chains of PEO molecules cannot freely leach out of the composite fibers. Furthermore, hydrogen bonding interactions between the CA and PEO chains [67, 68] could also contribute to the restriction of the free movement and extraction of PEO on the surface and inside of fibers when the selective dissolution.

Table 3.3 Mass Loss and Continuity of Solvent Varied Fibers after PEO Extraction

Sample	Electrospinning Solutions[a] (CA/PEO 80/20 in moles, 15 wt % in solutions)	Remaining fibers after water extraction (%)	Degree of continuity[b] of PEO phase
A	30/70 An/Ac	95.8	0.11
B	40/60 An/Ac	89.0	0.28
C	60/40 An/Ac	69.1	0.77
D	70/30 An/Ac	75.7	0.61
--	60/40 An/Ac, 100 CA	98.9	n/a

a. E-spinning condition: 0.08 mL/min, 15~18 kV, 15 cm
b. Deg. of continuity: $(m_0 - m_f)/m_0$, where m_0 =original PEO mass in fiber, m_f = final PEO mass after extraction

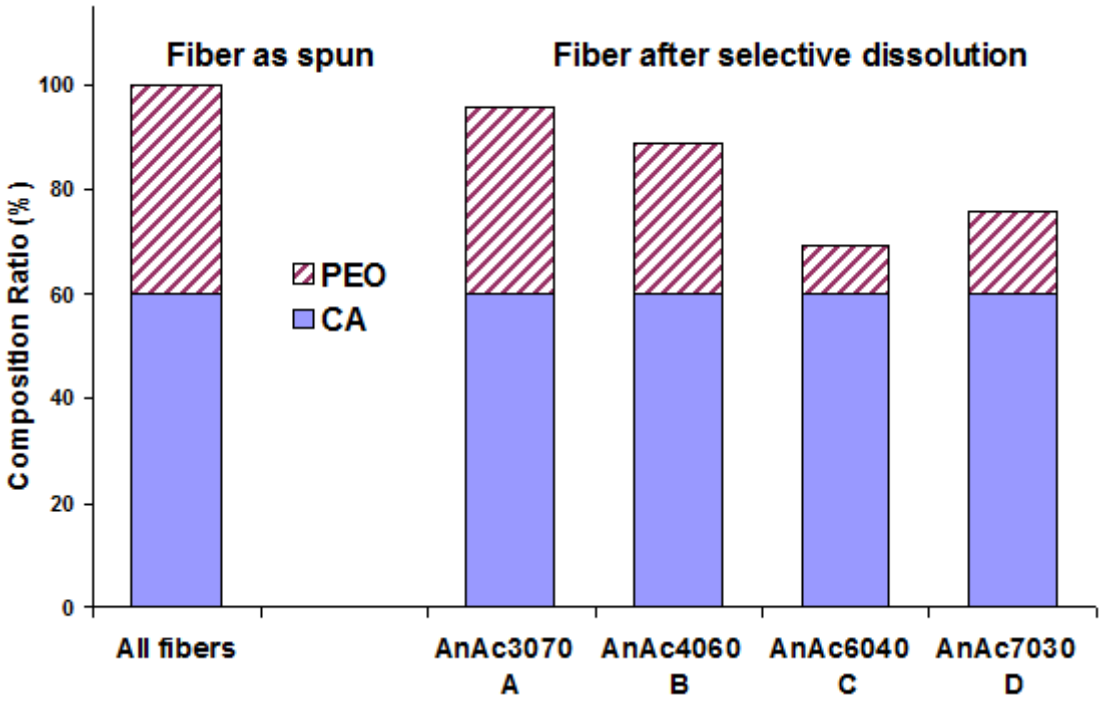

Figure 3.9 Comparison of CA/PEO Compositions after PEO Extraction; Four Types of Fibers Electrospun with Same Polymer Composition and Different Solvent Ratios (w/w)

3.5 Morphology of PEO Extracted Fiber

Morphologies of fiber electrospun with different solvent ratios were observed. The SEM images in Figure 3.10 are from electrospun CA/PEO fibers after selective dissolution, corresponding to those listed in Table 3.3 and Figure 3.9. While several fibers did not have any remarkable structural features, the fibers in Figure 3.10c showed obvious morphology of connected channels and elongated pores. The fascinating nano-structural patterns resulting from the PEO dissolution were observed to have 130 nm average width (Min: 90, Max: 200, Stdev: 32) and similar depth in fiber with 1.3 μm average diameter by means of the image analysis of SEM photographs. From the degree of continuity, approximate 80 wt% of PEO part in the CA/PEO blend formed a continuous structure and phase-separated in the blend during the electrospinning. Electrospun fiber with An/Ac 30/70 solvent (Figure 3.10a) was observed not to generate significant porous structure or channels on surface. This result suggested that the acetone-rich electrospinning solution had a highly mixed CA/PEO blend by the strong solubility of acetone, which resulted in little phase separation of PEO from the blend. Furthermore, the higher evaporation rate during electrospinning was too rapid allowing little for phase separation. And, due to the higher surface tension of acetonitrile, some of fibers were beaded as in the image (Figure 3.10a). On the contrary, the acetonitrile-rich solvent (70/30 An/Ac, Figure 3.10d) obviously enabled phase separation, however, the separated PEO phase did not merge or coarsen as observed for the solvent of 60/40 An/Ac (Figure 3.10c). The spinning solution with An/Ac 70/30 (Figure 3.10d) was believed to have an single phase, even the ambiguous turbidity in the diagram. However, the polymer molecules

were merely dispersed and behaved like a partially miscible blend. In addition, the solution had a relatively low vapor pressure than others. As a result, the time to phase coalescence of each phase was given [28] when the occurrence of CA/PEO phase separation, which leads to the most rough and coarse, but too open pattern in fiber after PEO extraction.

The phase separation mechanism involved with rapid solvent evaporation is very similar to that involved with spinodal decomposition [71]. The formation of the unique channeled structure may be due to a combination of factors, including viscosity and solubility of the polymers. This decreased viscosity promotes the development of a finely dispersed structure by two processes. The first is involved with rheological processes and the effect of the viscosity ratio of compositions, related to the minimum energy dissipation theory of a flow system [72]. The second effect is due to solvent effects, or the solubility of the components in the common solvent. Walheim *et. al* [73] showed that, with the evaporation of solvent, the different solubilities of polybutadiene (PB) and polycarbonate (PC) in THF would be likely to cause the PC to coaelesce, leading to the formation of an individually continuous aligned (core-sheath) structure. The process of phase separation of PEO from CA was also suggested to be dependent on the viscosity of the whole blending system, i.e. the mobility of the molecules at high solution concentration as the solvent evaporates.

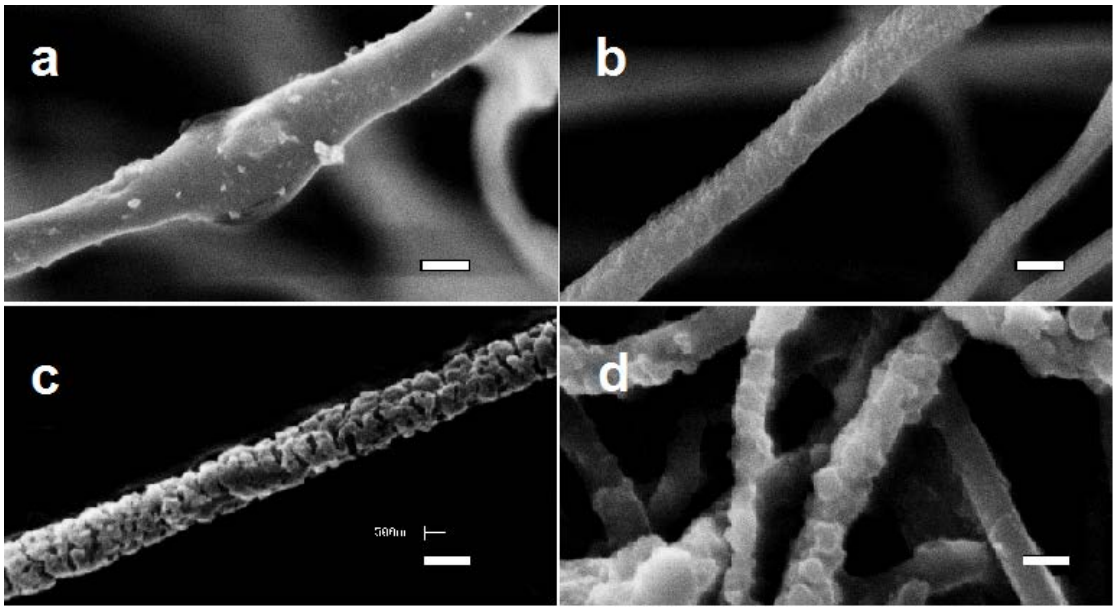

Figure 3.10 Morphology of Electrospun CA/PEO Fibers after PEO Extraction (Electrospinning Solvent Ratio: (a) An/Ac 30/70; (b) An/Ac 40/60; (c) An/Ac 60/40; (d) An/Ac 70/30; Polymer content: 15 wt% (a, b, c), 14 wt% (d), Polymer composition before extraction: CA/PEO 60/40 in weights, 80/20 in moles, Bar: 1 μm)

The thermodynamic behaviors discussed above were observed in thermal analysis results as well. Differential scanning calorimetry (DSC) thermograms showed thermal behaviors of components (Figure 3.11). It is known that glass transition temperature (T_g) of CA is 198–205 ^oC and the melting temperature (T_m) is 224–230 ^oC [29]. In the DSC analysis, the T_g transition is not obvious in the curve of the electrospun CA fiber (Figure 3.11a), while a broad low endothermic peak centering at 224 ^oC can be found, corresponding to T_m. Electrospun PEO fiber (Figure 3.11b) showed a strong melting endotherm at 64 ^oC and all PEO-containing products showed their typical melting peak in 50-65 ^oC. An interesting finding in the thermal analysis is that CA/PEO composites with the same ratio of CA/PEO (60/40, w/w) showed different behaviors. The electrospun fiber corresponding to Figure 3.11c was performed

with the electrospinning solution of An/Ac 60/40, while 3.11d with the solution of An/Ac 30/70. It was observed again that the An/Ac 30/70 solvent enabled a more miscible CA/PEO blend resulting in the strong peak at 172 ^{o}C in the middle of each phase of CA and PEO (Figure 3.11d). In contrast, An/Ac 60/40 solvent presented a relatively phase-separated behavior during the electrospinning (Figure 3.11c), leading to the individual peaks at 50 and 220, corresponding to PEO and CA, respectively. The phase behavior finally resulted in the electrospun fiber enabling the most extracted mass of PEO when the selective dissolution (Sample C in Table 3.3 and Figure 3.9). This indicated that the change in solubility of solvent affected miscibility of blended polymers [30-32]. Further analysis of the comparison of electrospun fiber (Figure 3.11d) with a solvent-casting sheet (Figure 3.11e) demonstrated that the degree of phase separation was affected by the drying condition. The solution (CA/PEO 60/40, An/Ac 70/30, Polymer/Solvent 15/85, w/w) was electrospun, in the mean time, the rest was then solvent-cast on a glass dish. While the solutions corresponding to Figure 3.11d and 3.11e are exactly identical, electrospun fiber showed a single peak indicating a well dispersed miscible phase of CA/PEO, whereas the solvent-casting presented a phase-separated blend with little or no evidence of miscibility (Figure 3.11e). Solvent-casting was a slow drying process compared with electrospinning where solvents evaporate very quickly due to the fast thinning of polymer jet. From the difference of evaporation rate, solvent-casting probably gave rise to the condition that CA and PEO nucleated and the phases grew. In the relevant literature, solvent-casting polymers have been reported to show sometimes higher heat of fusion (melting enthalpy) and sometimes lower heat. Chen *et al*. [45] reported that the higher crystallinity and higher heat of fusion took place

in a solvent-casting process compared with electrospun fiber in the thermal analysis of PEG/CA blend, whereas Liu *et. al* [22] studied cellulose acetate/acetone/dimethyl acetate solutions and found the lower heat of fusion and low crystallization in a solvent-cast film. In this study, thermal analysis showed that solvent-casting produced a lower melting enthalpy (Figure 3.11e) compared with electrospun fiber (Figure 3.11d), which suggested that the electrospinning process induced some levels of order, orientation and/or crystallization in the fibers. According to these thermal analyses, it is suggested that solvent properties (e.g. solubility parameter and vapor pressure) and a drying rate obviously affected the behavior of CA and PEO, especially in miscibility and phase separation of the blend both in solution state and the process of electrospinning.

It was interesting that there was no evidence of spherical or circular pores at tens (10s) nanometer level in the PEO extracted fibers while there were continuous interconnected patterns and channels. As shown in Figure 3.11d, the morphological feature probably resulted from the fact that the two polymers are thermodynamically not very immiscible. You *et. al* [60] showed the electrospun poly(glycolic acid)/poly(L-lactic acid) had a strongly immiscible behavior in thermal analysis, leading to uniform fine pores without channels or continuous grooves, which means an immiscible polymer blend tend to generate circular pores resulting from the matrix-domain dispersed morphology. Bognitzki *et. al* [61] analysed the phase separation mechanism of the cocontinuous blend in electrospinning. They expected that a concontinuous phase morphology would be more favored than a matrix-dispersed phase morphology for electrospun PLA/PVP blend fibers because

nucleation and growth decomposition needed more time to start than the initial growth of unstable concentration fluctuation. They demonstrated that the electrospun PLA/PVP blend fibers had a cocontinuous phase morphology. According to the observations, it is considered that the cocontinuous phase morphology in the CA/PEO fibers at 60/40 An/Ac in this study were formed by spinodal phase separation [65] rather nucleation and growth decomposition. A lot of previous selective dissolution studies were conducted with more immiscible polymers such as polyethylene oxide/polyacrylonitrile [33], P3HT/PCBM (photovoltaic blend) [62] and polybutadiene /polycarbonate [63], which presented immiscible thermal behaviors of electrospun fiber and three-dimensionally cocontinuous structure or interconnected pores after extracting one component. Kim *et. al* [64] reported that PVA/PAN bicomponent electrospun fiber using selective dissolution resulted in a decrease in the diameter of the fibers and the formation of grooves, pores, and craters on the fiber surface, which was also observed in this study, in spite of the immiscible PVA/PAN blend. Similarly, Wei *et. al* [63] observed that the good solubility of PMMA and PS in THF solvent, leads to the development of cocontinuous structure even with unfavorable solubility parameters to each other. Conclusively, in different solvent ratios from 30/70 to 70/30 of An/Ac (w/w), while the miscible nature of CA/PEO blend at a certain composition was observed to be favored for the cocontinuous morphology at 60/40, the miscible phases of the polymers gave a narrow composition range in producing a highly continuous structure and the extractable separated phase as in Figure 3.10c. And the solubility parameter differences between the polymers appeared to have an effect on blend morphology, however, the influence of solubility parameter was

reduced when a strong solvent for both polymers was employed, leading to various morphologies at a fixed polymer ratio.

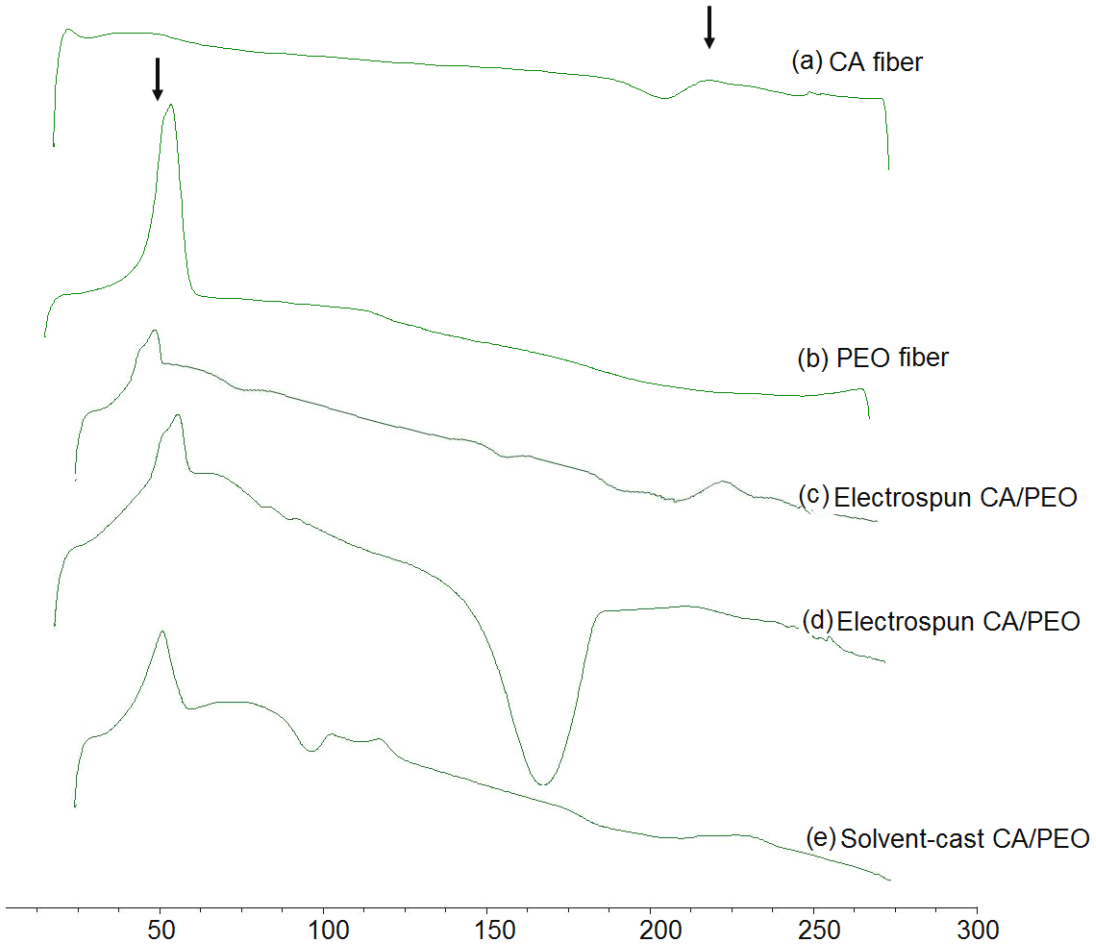

Figure 3.11 DSC of Electrospun CA, PEO and CA/PEO Composites: Electrospun fiber consisting of CA (a), PEO (b), CA/PEO from An/Ac 60/40 solvent (c), CA/PEO from An/Ac 30/70 (d) and solvent-casting sheet (e) from the same solution as (d)

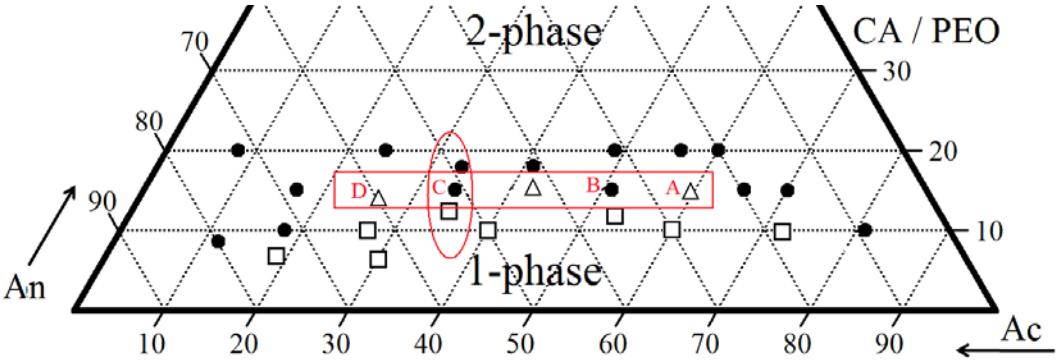

Figure 3.12 CA/PEO Solutions for Electrospinning (Solutions A~D in rectangular box: solvent ratio variation as in Table 3.3, Figure 3.9 and Figure 3.10; Solutions in oval : polymer content variation as in Figure 3.13)

Besides the effect of solvent ratio, the morphology dependence on polymer concentration at fixed solvent ratio was investigated. All the solutions used in the morphological observation were denoted in Figure 3.12. With the solvent ratio of An/Ac 60/40, 12 and 18 wt% of polymer solutions of those in Figure 3.10c were observed in Figure 3.13. In the morphology from 12 wt% polymer solution, it was observed that tiny knots and blossom-like structures existed on the surface of fiber (Figure 3.13a). In Figure 3.13b from 18 wt%, there were grooves and channels in more open pattern. Both are unique, however the reason was not very clear. It is suggested that more freely dispersed polymer molecules in 12 wt% solution than others resulted in fine dispersion and the PEO part burst out of the composite fiber breaking surface when dissolved in hot water; thus, leading to such a fluffy morphology on the fiber surface. As for the structure in Figure 3.13b, in terms of the electrospinning condition, initial polymer concentration resulting in higher viscosity may influence the orientation and aligned pattern in fiber. And low amount of solvents enabled rapid evaporation fluctuations and this affected the phase separation time and consistency in blended phase. In addition, increasing polymer content gave a bigger diameter of fiber because phase separation of higher content of

polymer solution would take place in an earlier stage of the jet formation in electrospinning. Overall, it was found that the lower polymer content (Figure 3.13a), if other compositions are constant, brought finer pattern according to the results of 12, 15 and 18 wt% of polymer with CA/PEO 60/40 solutions in Figure 3.10c and Figure 3.13. The morphological changes with the polymer concentrations mainly resulted from the solution viscosity as discussed before in the effect on increasing fiber diameter. In the investigation of the polymer concentration effect of PS-THF solutions consisting of single polymer and solvent [69], finer pores were observed with increasing concentration of polymer, resulting from a densely packed polymer and little amount of solvent when induced phase separation. However, CA/PEO blended polymer solutions showed a finer and fluffy surface morphology with increasing the polymer concentration. This demonstrated that the dissolution phase is controlled by the disentanglement of the polymer chains and by the diffusion of the chains through a boundary layer adjacent to the polymer–solvent interface, leading to an extractable finer phase in a low concentration of polymer [44].

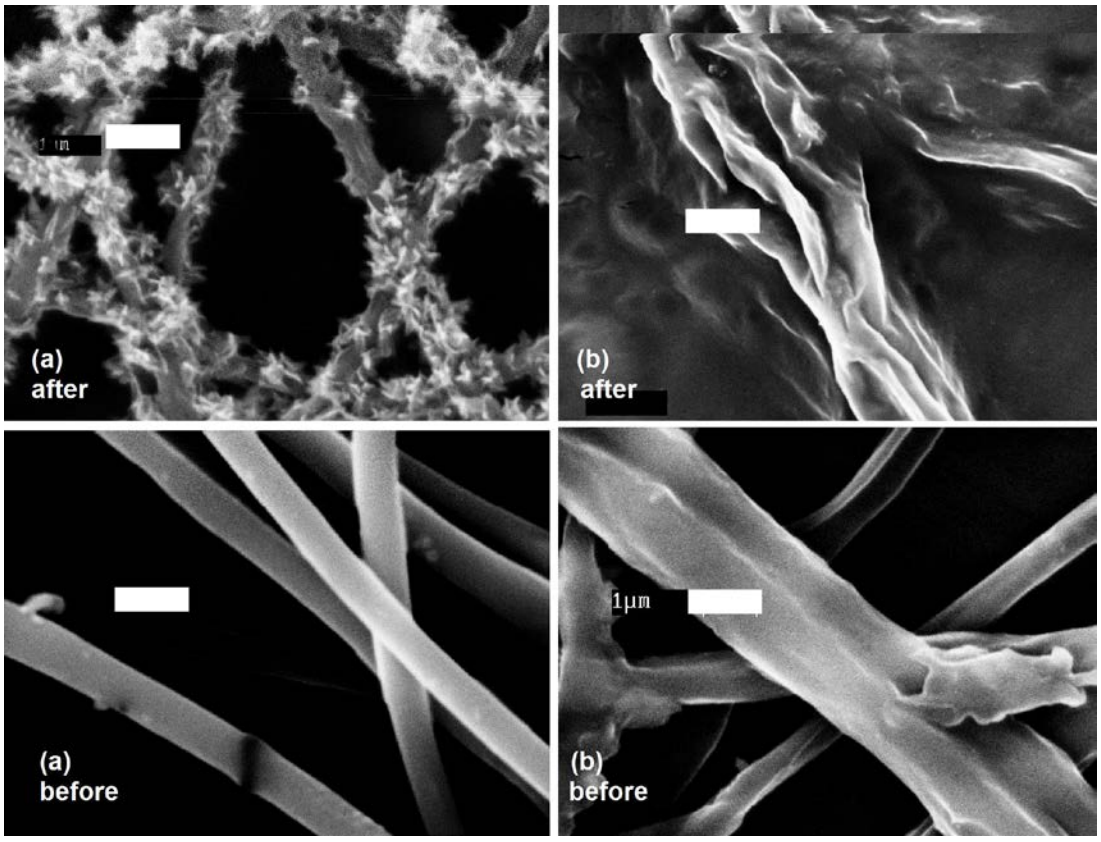

Figure 3.13 Morphology of Electrospun CA/PEO Fibers (Electrospinning Polymer Concentrations: 12 wt% (a) and 18 wt% (b); PEO extraction: after (upper) and before (bottom); Electropsinning solution composition: CA/PEO 60/40 in weights, 80/20 in moles, An/Ac 60/40 w/w; Bar: 1 μm)

In surface chemistry, BET surface area is used to gain insight into the active reaction area and adsorption properties of materials. The BET surface area was measured for electrospun fibers made using 60/40 An/Ac with the two weight percentages of polymer (15 and 12 %) that showed the most complex morphology in each comparison; solvent ratio variation and polymer concentration change (Figure 3.10 and Figure 3.13). The results from BET surface area measurements (Table 3.4) also support the microscopy observation. From BET measurements, it was found that the average surface area of the fluffy fibrous membrane made using a 12-weight percent of

polymer, Figure 3.13a, after selective dissolution of PEO was 19.7 m^2/g, whereas the normal CA electrospun fiber showed a surface area of 6.5 m^2/g. Furthermore, the channeled fiber spun using 15-weight percent of polymer, Figure 3.10c, showed 21.8 m^2/g even with the larger fiber diameter. While the surface area was about three times larger than the normal morphology, the result indicated that the actual increased surface of the continuous pores and nanochanneled pattern appeared in Figure 3.10c had an effect as that of six to seven times smaller diameter fiber considering the twice larger (1.33 μm) than that of the CA fiber with normal morphology (0.57 μm). This also suggested that the channeled fiber (Figure 3.10c) had more continuous and interconnected structures in it than the fine fluffy morphology (Figure 3.13a) in terms of surface area. The increase in surface area obtained in this study is higher than that reported by other researchers. In a study on formation of nanoporous polyacrylonitrile fibers by electrospinning bicomponent, the result was a 2.5 times increase in surface area compared to the as-spun nonporous fibers [33]. Similarly, another study of silica nanoparticulate-polyacrylonitrile composite and porous nanofibers showed 20 % increase in surface area in the formation of pores [34].

Table 3.4 BET Surface Area and BJH Pore Size of Electrospun Membrane

Electrospinning Solutions			BET surface area (m^2 g^{-1})	BJH pore size (nm)	Fiber diameter[a] (μm)	Morphology
Solvent (w/w)	Polymer[b] (w/w)					
An/Ac 60/40	CA100 (No extraction)	15 wt%	6.5	4.1	0.57 (0.17)	--
An/Ac 60/40	CA/PEO 60/40 (PEO extracted)	12 wt%	19.7	23.3	0.55 (0.20)	Figure 3.13a (upper)
An/Ac 60/40	CA/PEO 60/40 (PEO extracted)	15 wt%	21.8	89.0	1.33 (0.28)	Figure 3.10c

[a]Reported values are average diameter with standard deviation in parenthesis.
[b]CA/PEO 80/20 in moles

Nitrogen adsorption–desorption isotherms (BET method) and pore size distribution curves (BJH method) are shown in Figure 3.14. The N_2 isotherms of all the samples are generally similar (Figure 3.14 a, c, e). Isotherm (a) showed a type IV behavior and it was also partially similar to type II according to IUPAC classification [41], which means that physisorption behavior of the non-extracted normal CA fiber followed the nonporous materials or microporous adsorbents. This has good agreement with the very small average pore size and pore distribution showing narrow and micropore region distribution (Figure 3.14b). Considering the fiber formation condition, the microporous and dense structure was suggested to result from the

homogeneous state of pure CA in a solution and during electrospinning as well. The other isotherms showed a type IV adsorption with hysteresis loops of a type H2, tending to saturate at high pressures, which means the fibers are associated with capillary condensation taking place in near a mesopore level (2 nm – 50 nm). The initial part of the type IV, a curved slope, is attributed to monolayer-multilayer adsorption. Since the general shapes of adsorption-desorption isotherms and the hysteresis are similar in the other two fibers, it can be inferred that the pore structure is similar in the samples of fluffy morphology and channeled one. However, further detail analysis showed that the desorption curve fairly dropped and the hysteresis is narrower in Figure 3.14(c) compared with (e). This isotherm behavior (Figure 3.14c) indicates that the fluffy morphology fiber made using 12 wt% CA/PEO blend has a relatively simple pore structure inside and more uniform in size distribution, which is in good agreement with Figure 3.14 d. In contrast, the channeled fiber made using 15 wt% CA/PEO blend was suggested to have more complex porous structure inside compared with fiber from 12 wt% polymer, presenting a slightly longer desorption tail in hysteresis of the isotherm (Figure 3.14e). The structural differences between fluffy morphology and channeled morphology, in terms of pore structure, resulted from high viscosity and other consequential limitations such as long disentanglement time in polymer molecules in more viscose solution with 15 wt% polymer. Polymers in a low concentration solution are relatively freely in motion, which is favorable to bring a homogeneous phase when phase separation occurs, thus, leading to more uniform and regular phases of blend resulting in fine pores. With this insight, the order of intra-fiber pore size observed in the BET/BJH measurement was understandable: Pure CA polymer had the smallest pore,

the fiber from low concentration CA/PEO blend was next and the high concentration blend showed the largest and more complex porous structure than others. As discussed above, the intra-fiber pores (Figure 3.14d, f) were observed that 15 wt% CA/PEO polymer concentration generated significantly larger average pore (89.0 nm) than 12 wt% CA/PEO (23.3 nm). In addition, the intra-fiber pore information of channeled fiber suggested that the interconnected porous nanopatterned fiber has potential to offer a physical adsorption property. This will be further described in MP removal tests.

3.6 MgO Incorporated Fiber

MgO loaded electrospun membranes were prepared introducing MgO nanoparticles into the nanochanneled morphology that was previously confirmed. Before loading MgO in fiber, experimental data on the changes of MP concentration with the amount of MgO nanoparticles as same as used in this study was provided by Lange L. E. (Figure 3.15). Based on the preliminary result, the load amount of MgO was determined as 10-weight percent of polymer part. Before PEO selective dissolution was performed, CA/PEO/MgO (60/40/6) composite fiber was characterized (Figure 3.16). X-ray diffraction patterns (Figure 3.16) presented consistent characteristics of MgO particles. Typical peaks of the MgO crystal structure (Figure 3.17a) were still observed in electrospun CA/PEO/MgO composite fiber (Figure 3.17b). The corresponding peaks at 39 and 61 degree of 2θ were in agreement with the literature values of MgO particle [35, 36]. The incorporated amount of MgO was characterized with thermogravimetry analysis (Table 3.5), which showed that the fiber contained 9-11 wt % of metallic ashes. From the result, it was observed that fibers had approximately 8 wt% of MgO. In addition, the thermal decomposition temperature of fiber was increased with loading MgO.

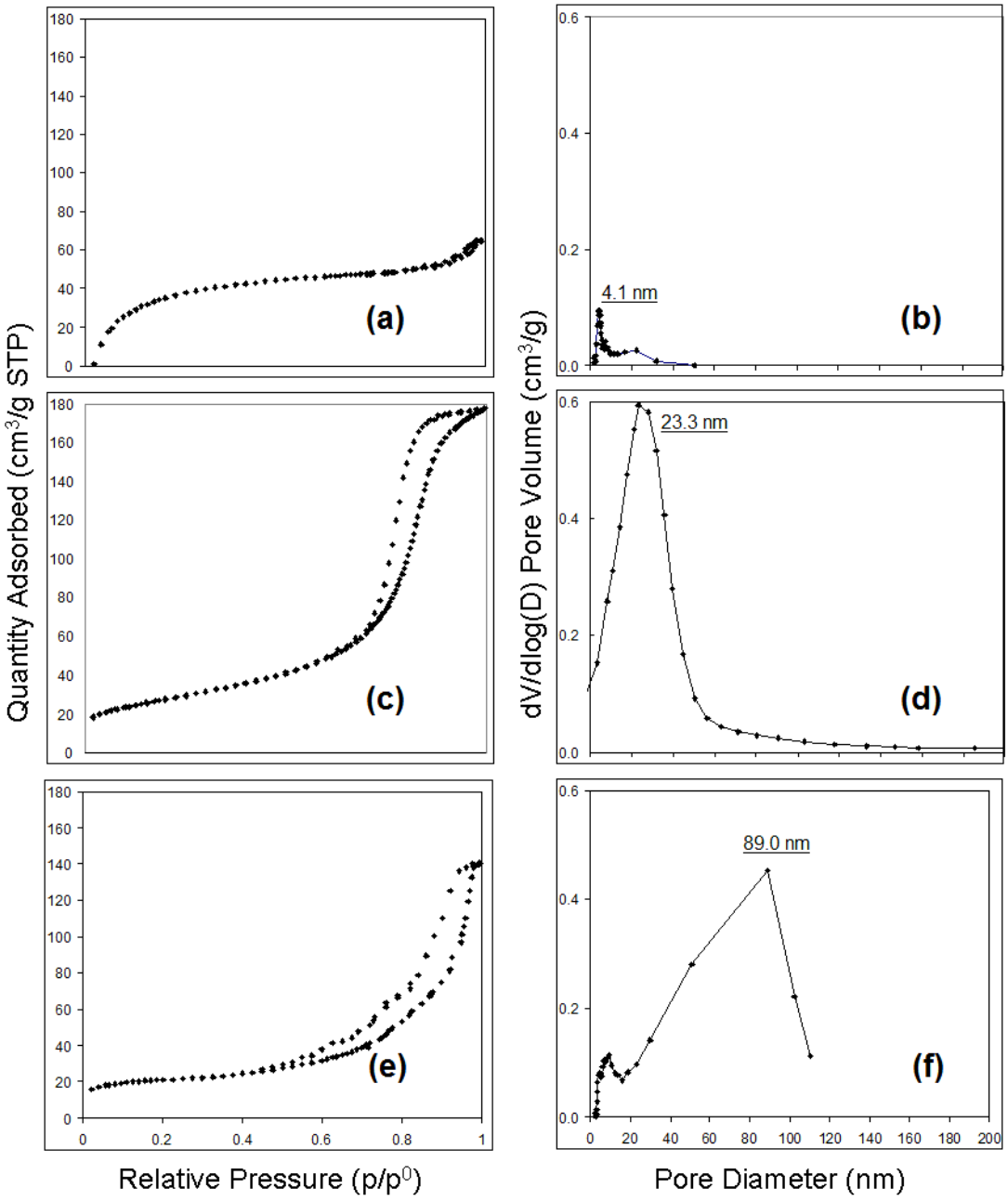

Figure 3.14 Nitrogen Adsorption-Desorption Isotherm (a, c, e) And BJH Pore Size Distribution (b, d, f); CA fiber (a), (b); CA/PEO 12 wt% Electrospun Fiber (c), (d); CA/PEO 15 wt% Electrospun Fiber (e), (f) (Solvent: An/Ac 60/40, w/w)

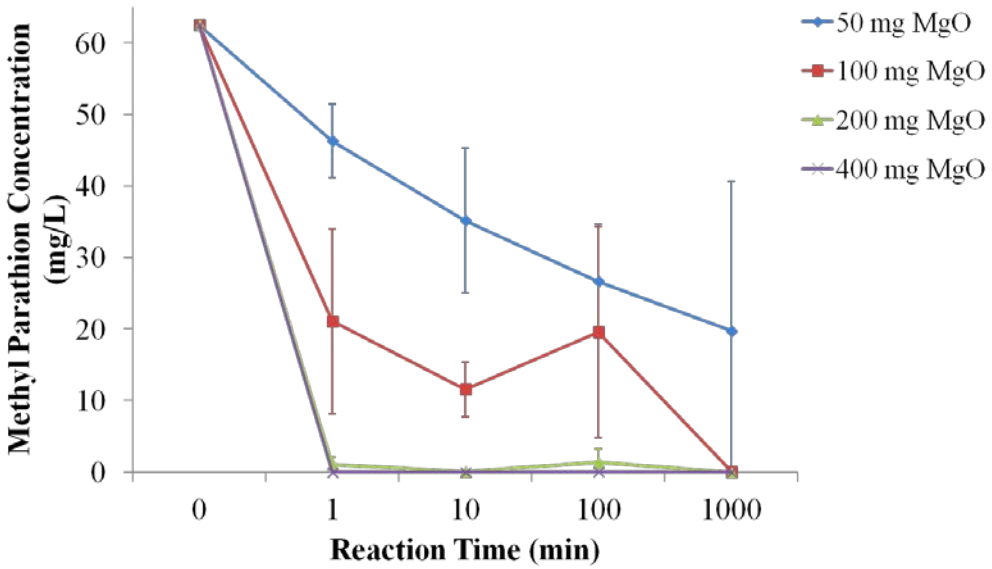

Figure 3.15 Methyl Parathion Concentration in Hexane After Degradation With MgO Nanoparticles [37]

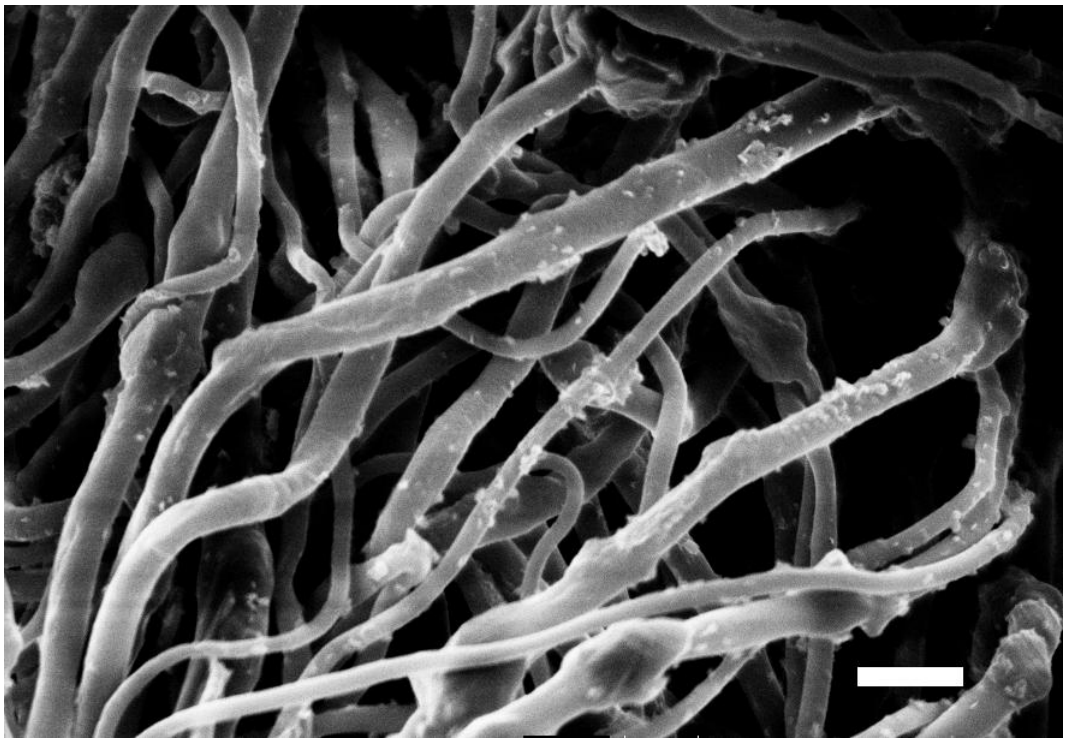

Figure 3.16 MgO Incorporated CA/PEO Electrospun Fiber (Not extracted, Bar: 3 μm)

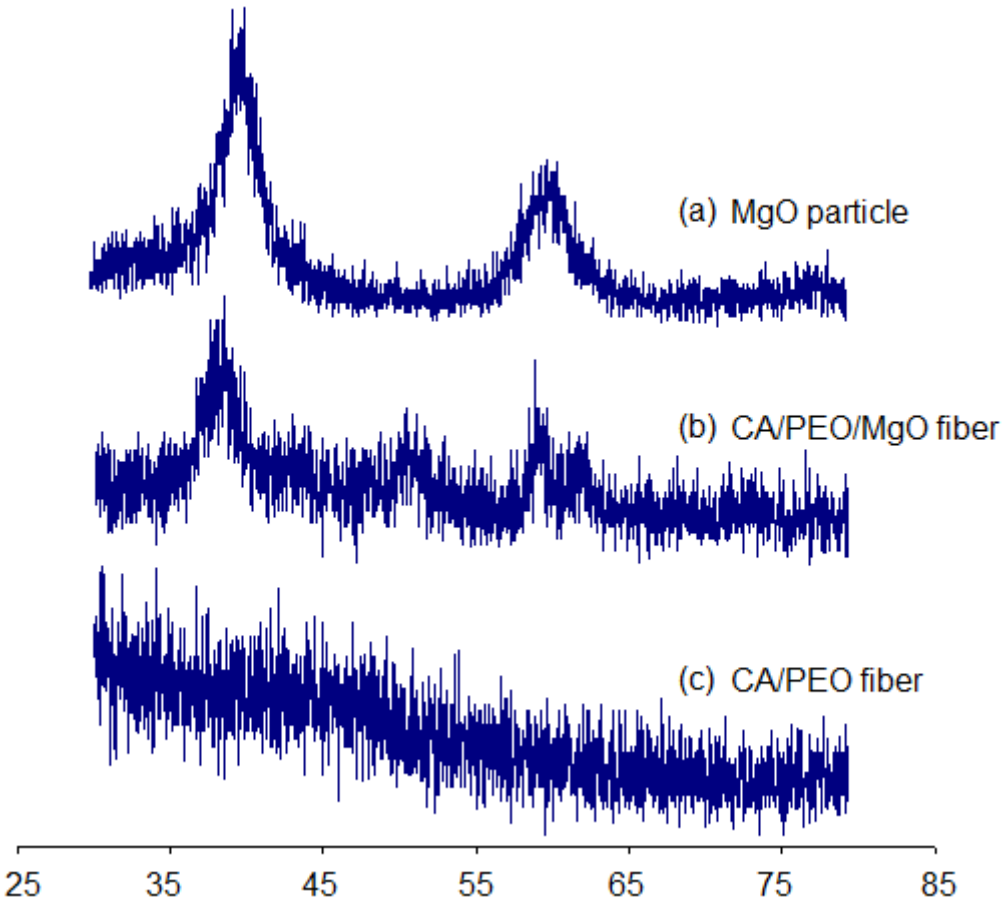

Figure 3.17 X-ray Diffraction Patterns of MgO particle (a), MgO loaded CA/PEO Fiber (b) and Unloaded CA/PEO Fiber (c)

Table 3.5 Thermal Decomposition Temperature (T_d) and Weight Residue of CA-MgO Electrospun Membrane

Electrospinning Solution Composition				T_d (°C) (at 5% wt loss)	Weight residue (at 700 °C, wt%)
Solvent (w/w)	Polymer ratio[a] and content (w/w)		MgO		
An/Ac 60/40	CA 100	15 wt%	Non	289	0.9
An/Ac 60/40	CA 100	15 wt%	Loaded	297	11.2
An/Ac 60/40	CA/PEO 60/40 (PEO extracted)	15 wt%	Non	290	0.7
An/Ac 60/40	CA/PEO 60/40 (PEO extracted)	15 wt%	Loaded	295	9.1

[a]CA/PEO 80/20 in moles

3.7 Deacetylation

It was demonstrated that deacetylation of CA generated the conversion into cellulose structure with more stable and rigid sheets resulting from the increased intermolecular H-bonds. Figure 3.18 showed changes in FTIR spectra for the CA fibrous mats during deacetylation reaction. The peaks at 1700-1800 cm^{-1}, 1350-1400 cm^{-1}, 1200-1300 cm^{-1} and 1000-1150 cm^{-1} correspond to carbonyl stretching (C=O), methyl deformations (C-CH_3), acetate stretching (C-C-O) and C-O stretching, respectively. The change in the chemical structure of the electrospun CA fibrous mats during deacetylation showed that the intensities of characteristic adsorption peaks of CA decreased and completely disappeared with increasing time. The peaks at 1742 to approximately 1744

cm^{-1} and 1365 to 1375 cm^{-1} almost disappeared in 1h, which is in agreement with published data [22, 38, 39]. This indicates that CA nanofibers were converted into cellulose. In addition, the broad hydroxyl peak (-OH) broad at around 3400 cm^{-1} became broader and increased as the deacetylation reaction time increase. This result demonstrates that the number of –OH groups increased over time. Since the carbonyl peak (1700-1760 cm^{-1}) does not overlap the other groups, this peak was utilized to monitor the degree of deacetylation.

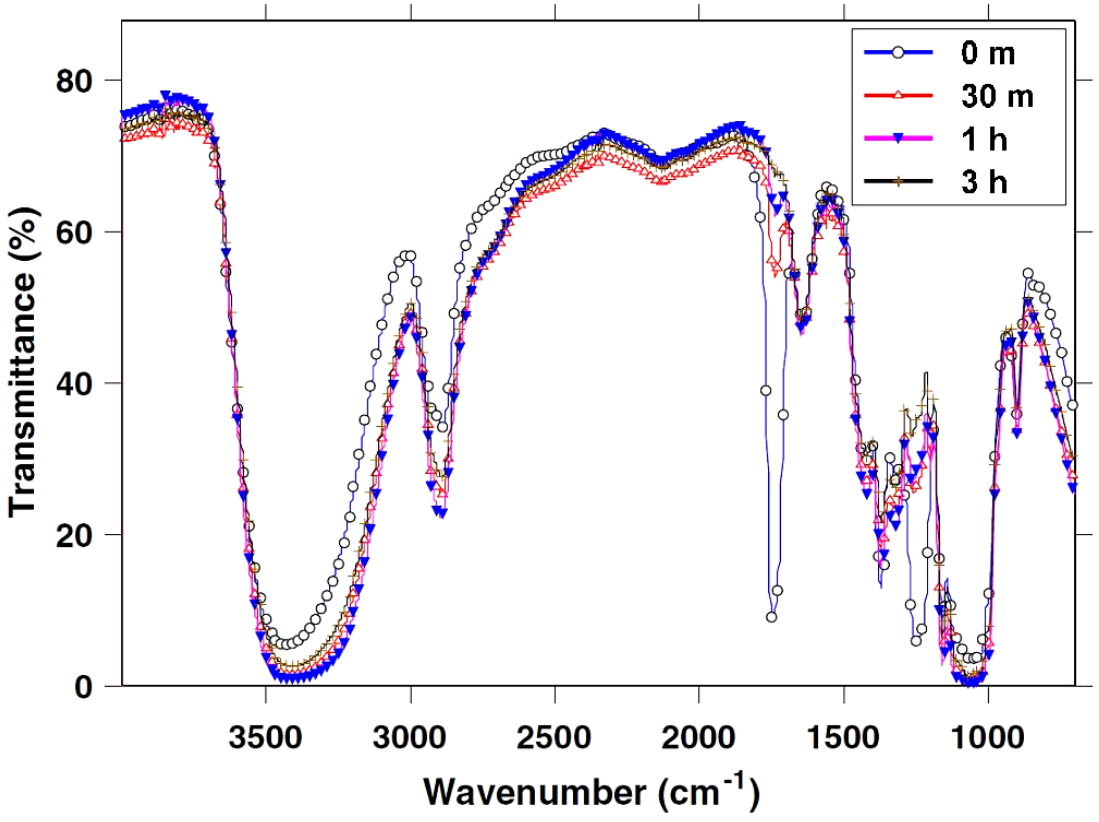

Figure 3.18 Changes in FTIR Spectra over Deacetylation Time (0, 30 min, 1 h, 3 h)

3.8 MP Removal Property of MgO Incorporated Membrane

The protective clothing in military is mostly expected to help maximize the survivability, sustainability, and combat effectiveness of the individual soldier system against extreme weather conditions, ballistics, and NBC (nuclear, biological, and chemical) warfare [74]. Because of their great surface area, nanofiber fabrics are capable of the neutralization of chemical agents and without impedance of the air and water vapor permeability to the clothing [75]. MP removal test with MgO incorporated channeled fibrous membrane has a purpose of investigating potential to use such a membrane as a protective clothing material. The channeled electrospun fiber (Figure 3.10c, Table 3.4) can be used as a self-decontamination membrane due to the enlarged surface area without downsizing fiber diameter. The selected model compounds were magnesium oxide (MgO) nanoparticles and methyl parathion (MP), an organophosphate that is used as a pesticide, i.e. insecticide and a stimulant of chemical warfare agents. The attempt to decompose MP using MgO incorporated surface patterned fiber was based on the surface chemistry between MgO and MP. The stoichiometric reaction scheme of MgO and MP was recently proposed by Lange *et al*. [35], which indicated that the exposed surface of MgO out of a fiber substrate predominantly involved in the adsorption and consequential destruction of MP. According to their study, the surface of MgO has more importance. It was reported that for every two methyl parathion molecules introduced to MgO surface, one O,O,O-compound, two adsorbed 4-nitrophenol groups and one adsorbed group containing phosphorous doubly bonded to sulfur are generated (Figure 3.19) [35]. Therefore, the highly channeled fiber with a large surface area was expected to favorably influence the adsorption activity of MgO. While the

three types of products existed, only the concentrations of MP in hexane were detected to determine the decontamination performance of the MgO loaded membrane in this study (Figure 3.20).

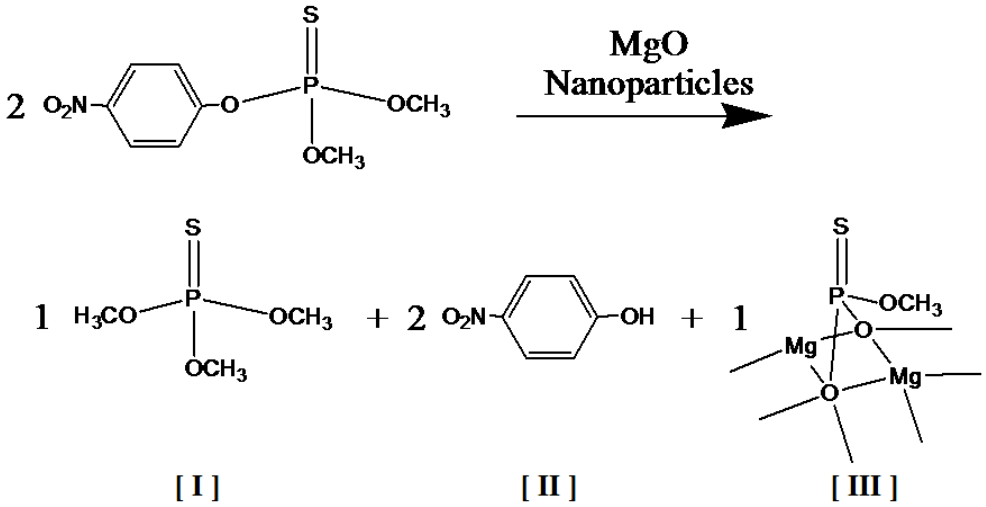

Figure 3.19 Reaction Scheme for Methyl Parathion in the Presence of MgO Nanoparticles[3] [35]

[3] [I] O,O,O-trimethyl phosphoric thiourate
[II] 4-nitrophenol
[III] degraded and adsorbed compound with P=S bond on MgO surface

Table 3.6 Sample Fibers in MP Solution Test

	Electrospinning Solution Composition				Fiber diameter[a] (μm)
	Solvent (w/w)	Polymer ratio[b] and content (w/w)		MgO	
Sample 1	An/Ac 60/40	CA 100	15 wt%	Non	0.57 (0.17)
Sample 1 with MgO	An/Ac 60/40	CA 100	15 wt%	Loaded	0.86 (0.21)
Sample 2	An/Ac 60/40	CA/PEO 60/40 (PEO extracted)	15 wt%	Non	1.33 (0.28)
Sample 2 with MgO	An/Ac 60/40	CA/PEO 60/40 (PEO extracted)	15 wt%	Loaded	1.35 (0.39)

[a]Reported values are average diameter with standard deviation in parenthesis.
[b]CA/PEO 80/20 in moles

Methyl parathion removal tests were conducted using several adsorbents such as chitosan-silver complexes [76], rice bran [77], chestnut shells [78], treated watermelon peels [79] from aqueous solutions. The solution-soaking test method was conducted with four types of samples listed in Table 3.6. Using normal morphology fiber (Sample 1) and nanochanneled patterned fiber (Sample 2), fibrous membranes with and without MgO nanoparticles were prepared. The result of fiber-soaking test (Figure 3.20 and Table 3.7) confirmed that both MgO containing fibers had enhanced MP removal from the contaminating MP/hexane solution. Overall, the Sample 2 with MgO showed larger decrease of MP and higher reaction rate than Sample 1 with MgO. In particular, 33.6% removal of MP was observed in Sample 2 with MgO

for 100 min, whereas 13.6% removal in Sample 1 with MgO. The remarkable performance of Sample 2 with MgO was suggested to result from the large amount of MgO active sites due to the large surface area of the channeled fiber substrate (BET surface area: 21.8 m^2/g). Furthermore, the channels and pores in the fiber were also suggested to contribute to the adsorption of MP molecules from the solution, which was supported with the result of SEM morphology observation (Figure 3.10c), BET isotherm and BJH pore information (Figure 3.14) indicating mesopores and micropores in fiber (average intra-fiber pore width: 89 nm). In fact, the MgO unloaded Sample 2 with channeled morphology was observed to have the property of adsorption and removal of MP, presenting a significant decrease of MP mass (7.2%) in 100 min, whereas unloaded Sample 1 had no evidence of removing MP. As a result, the MgO loaded Sample 2 fiber was observed to have a greater MP removal property. With regards to the physical adsorption of the porous fiber as well as the large amount of exposed MgO particles due to the large surface area of the fiber substrate, the MgO loaded nanochanneled fiber (Sample 2 with MgO) resulted in a larger decrease of MP concentration (Figure 3.20). In addition, the results suggest that the more than 100 min should require to have all the exposed surfaces of MgO particles active in destructive adsorption, and to enable the physical adsorption of MP into channels and pores in fiber.

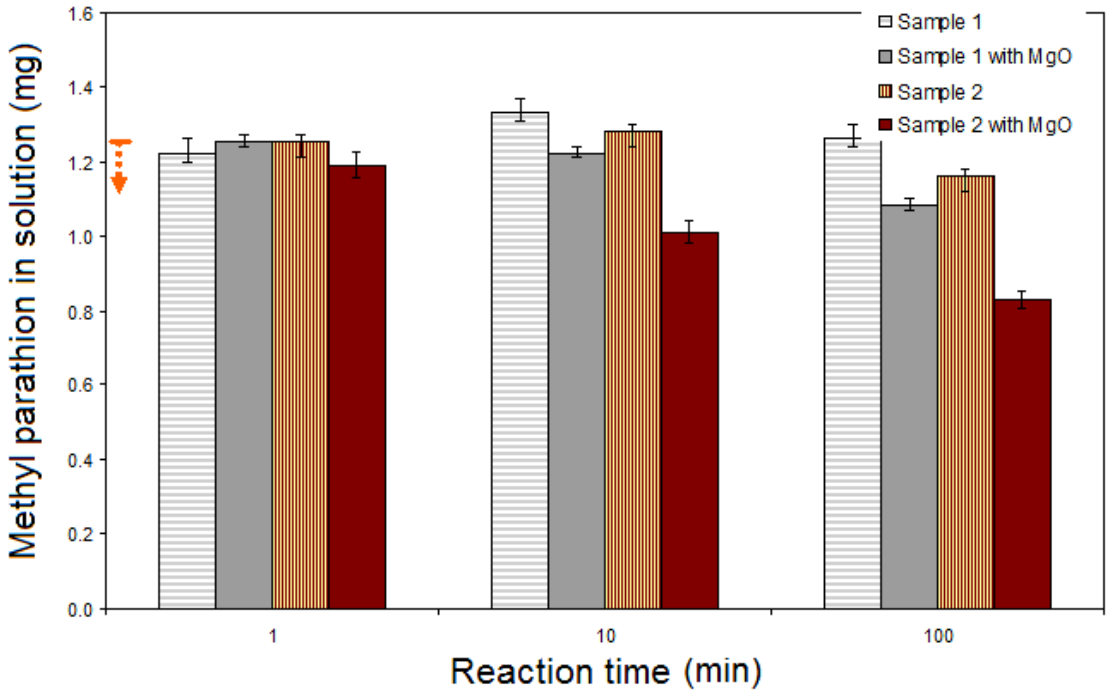

Figure 3.20 MP Amount after Reaction with Electrospun Fibers (Sample 1: conventional morphology, Sample 2: nanochanneled pattern, Starting mass 1.25 mg MP at 0 min)

Table 3.7 Methyl Parathion Amount and Removal Percentage[a] in Hexane after Treatment with MgO Incorporated Membrane (Sample 1: conventional morphology, Sample 2: nanochanneled, Starting mass 1.25 mg MP at 0 min)

		Reaction Time		
		1 min	**10 min**	**100 min**
Sample 1	MP mass (mg)	1.22	1.33	1.26
	Removed MP (%)	2.4	0	0
Sample 1 with MgO	MP mass (mg)	1.24	1.22	1.08
	Removed MP (%)	0.8	2.4	13.6
Sample 2	MP mass (mg)	1.26	1.28	1.16
	Removed MP (%)	0	0	7.2
Sample 2 with MgO	MP mass (mg)	1.19	1.01	0.83
	Removed MP (%)	4.8	19.2	33.6

[a]Percentage is based a starting amount (t = 0) of 1.25 mg. Negative value of removal percentage is denoted as zero.

Another evaluation of MP removal was conducted in membrane filtration (Figure 3.21 and Table 3.8). In the membrane test, the channeled morphology fiber (Sample 2 with MgO) was also observed to have the greater MP removal property than Sample 1. The initial mass of MP in the membrane test was ten times and incorporated MgO in fiber was approximately three times more than those in the soaking test. So, it is reasonable that the overall removal rates were observed to lower than the solution-soaking measurement. However, the higher MP removal was observed in MgO loaded Sample 2 fiber compared to that in MgO loaded Sample 1. Calculated with the initial mass of 12.5 mg MP, 6.7% vs 0.8 % at the second cycle and 8.4 % vs 2.8% at the third cycle of filtration were observed in MP removal percentage in Sample 2 MgO and Sample 1 MgO, respectively. The high removal ratios of channeled fiber to normal fiber were constantly observed and suggested that the physical adsorption by fiber substrate and destructive adsorption by MgO took place earlier stage in membrane filtration, which indicates that the membrane filtration by suctioning encouraged the intensive facilitation of MP molecules in liquid solution in coming into contact with MgO particles embedded in the fibrous substrate. Compared with the solution-submerging type evaluation, the time efficient reaction was observed in membrane filtration as the each filtration cycle was over within a minute due to a suction force. In other words, advantage of surface patterned porous structure could be rapidly established in the form of membrane with catalytic components without downsizing the diameter of fibers.

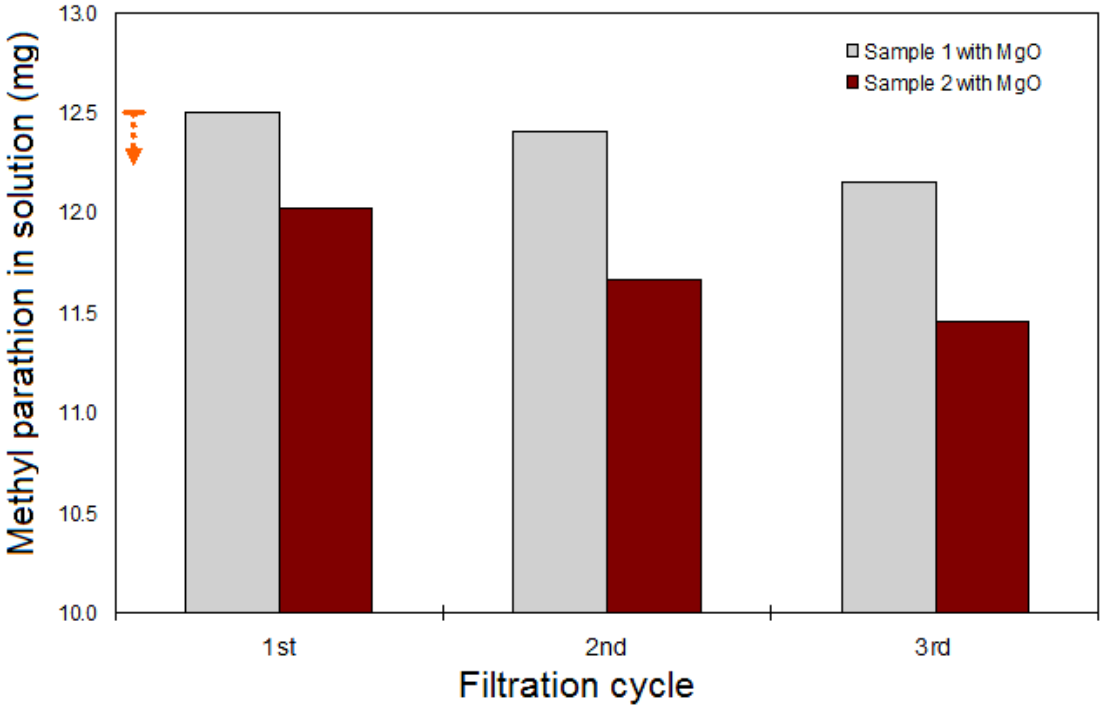

Figure 3.21 MP Amount and Degradation Ratio with Electrospun Fibrous Membrane in Filtration (Sample 1: conventional morphology, Sample 2: nanochanneled pattern, Starting mass: 12.5 mg MP at 0 min)

Table 3.8 Methyl Parathion Amount and Removal Percentage[a] in Hexane after Treatment with MgO Incorporated Membrane (Sample 1: conventional morphology, Sample 2: nanochanneled, Starting mass 12.5 mg MP at 0 min)

		Filtration Cycle		
		1st	**2nd**	**3rd**
Sample 1 with MgO	MP mass (mg)	12.49	12.40	12.15
	Removed MP (%)	0	0.8	2.8
Sample 2 with MgO	MP mass (mg)	12.22	11.66	11.45
	Removed MP (%)	3.8	6.7	8.4

[a]Percentage is based a starting amount (t = 0) of 12.5 mg. Negative value of removal percentage is denoted as zero.

4. CONCLUSIONS

Highly interconnected pores and channels were able to form in electrospun fiber using a binary solvent (An/Ac) and a polymer mixture (CA/PEO). Polymer-polymer, polymer-solvent and solvent-solvent interactions resulted from varying the ratio of solvents, leading to different morphology in electrospun fibers. A polymer solution consisting of An/Ac 60/40 and 15 wt % of CA/PEO 60/40 (80/20, mol) enabled the highest degree of continuity (0.77) of PEO phase in CA matrix during the electrospinning. The interconnected channels, intra-fiber pores (89 nm width) and large surface area (21.8 m^2/g) were observed at the electrospun fiber fabricated with the above composition. With decreasing polymer concentration in electrospinning solutions, the PEO extracted CA fiber showed fluffy structure, resulting from a single phase CA/PEO solution favorable to disperse to each polymer. Using deacetylation of CA, the highly connected nanochanneled fiber was able to expand the application to cellulose fiber, more stable material to organic solvents. A catalyst incorporated substrate of the nanochanneled fiber contained MgO was investigated as a methyl parathion removal membrane. In both a soaking test and a membrane filtration, the MgO loaded highly channeled fiber was observed to remove more MP, which resulted from the physical adsorption and destructive adsorption. MP was suggested to be adsorbed and removed from solutions by the exposed MgO particles in fiber and the adsorption to porous fiber. The advantage of the channeled morphology over the conventional regular surface in fiber was shown in a membrane filtration process.

REFERENCES

(1) McCann, J. T.; Li, D.; Xia, Y. N. "Electrospinning of Nanofibers with Core-Sheath, Hollow, or Porous Structures" *J. Mater. Chem.* **2005**, 15, 73.

(2) Kalra, V.; Lee, J. H.; Park, J. H.; Marquez, M.; Joo, Y. L. "Confined Assembly of Asymmetric Block-Copolymer Nanofibers via Multiaxial Jet Electrospinning" *Small* **2009**, 5 (20), 2323.

(3) Tang, C.; Chen, P.; Liu, H. "Cocontinuous cellulose acetate/polyurethane composite nanofiber fabricated through electrospinning" *Polym. Eng. Sci*. **2008**, 48, 1296.

(4) Zhang, W.; Yao, D.; Zhang, Q.; Zhou, J. G.; Lelkes, P. I. "Fabrication of interconnected microporous biomaterials with high hydroxyapatite nanoparticle loading" *Biofabrication* **2010**, 2, 1.

(5) Nguyen, L.; Mighri, F.; Deyrail, Y.;Elkoun, S. "Conductive Materials for Proton Exchange Membrane Fuel Cell Bipolar Plates Made from PVDF, PET and Co-continuous PVDF/PET Filled with Carbon Additives " *Fuel Cells* **2010**, 10, 938.

(6) Mooney, D. J.; Mazzoni, C. L.; Breuer, C.; McNamara, K.; Hern, D.; Vacanti, J. P.; Langer, R. "Stabilized polyglycolic acid fibre-based tubes for tissue engineering." *Biomaterials* **1996**, 17, 115–24.

(7) Freed, L. E.; Marquis, J. C.; Nohria, A.; Emmanual, J.; Mikos, A. G.; Langer R. "Neocartilage formation in vitro and in vivo using cells cultured on synthetic biodegradable polymers." *J. Biomed. Mater. Res*. **1993**, 27, 11–23.

(8) Thompson, R. C.; Yaszemski, M. J.; Powers, J. M.; Mikos, A. G. *Biomaterials* **1998**, 19, 1935–43.

(9) Mikos, A. G.; Bao, Y.; Cima, L. G.; Ingber, D. E.; Vacanti, J. P.; Langer, R. "Preparation of poly(glycolic acid) bonded fiber structures for cell attachment and transplantation" *J. Biomed. Mater. Res.* **1993**, 27, 183–9.

(10) Whang, K.; Thomas, C. H.; Healy, K. E.; Nuber, G. "A novel method to fabricate bioabsorbable scaffolds" *Polymer* **1995**, 36, 837–42.

(11) Schugens, C.; Maquet, V.; Grandfils, C.; Jerome, R.; Teyssie, P. "Polylactide macroporous biodegradable implants for cell transplantation. II. Preparation of polylactide foams by liquid-liquid phase separation" *J. Biomed. Mater. Res.* **1996**, 30, 449–61.

(12) Potschke, P.; Paul, D. R.; "Formation of Co-continuous Structures in Melt-Mixed Immiscible Polymer Blends" *J. Macromol. Sci., Polym. Rev.* C **2003**, 43, 87–141.

(13) Yuan, Z. H.; Favis, B. D.; "Macroporous poly(l-lactide) of controlled pore size derived from the annealing of co-continuous polystyrene/poly(l-lactide) blends" *Biomaterials* **2004**, 25, 2161–70.

(14) Yao, D.; Zhang, W.; Zhou, J. G.; "Controllable Growth of Gradient Porous Structures" *Biomacromolecules* **2009**, 10, 1282–6.

(15) Zhang, W.; Deodhar, S.; Yao, D. "Geometrical Confining Effects in Compression Molding of Co-continuous Polymer Blends" *Ann. Biomed. Eng.* **2010**, 38, 1954–64.

(16) Khaleel, A.; Kapoor, P. N.; Klabunde, K. J. "Nanocrystalline metal oxides as new adsorbents for air purification" *NanoStruct. Materials*. **1999**, 11, 459.

(17) Fujishima, A.; Honda, K. "Electrochemical photolysis of water at a semiconductor electrode" *Nature* **1972**, 37, 238.

(18) Linsebigler, A. L.; Lu, G.; Yates, J. T. "Photocatalysis on TiO_2 Surfaces: Principles, Mechanisms, and Selected Results" *Chem. Rev.* **1995**, 95, 735.

(19) Rajagopalan, S.; Koper, O.; Decker, S.; Klabunde, K. J. "Nanocrystalline Metal Oxides as Destructive Adsorbents for Organophosphorus Compounds at Ambient Temperatures" *Chem. Eur. J.* **2002**, 8 (11), 2602.

(20) Decker, S.; Klabunde K. J. "Enhancing Effect of Fe_2O_3 on the Ability of Nanocrystalline Calcium Oxide to Adsorb SO_2" *J. Am. Chem. Soc.* **1996,** 118, 12465.

(21) Hertel, R. F. et al. Environmental Health Criteria 145: Methyl Parathion, Fraunhofer Institute of Toxicology and Aerosol Research, Hanover, Germany **1993**, 19.

(22) Liu, H. Q.; Hsieh, Y. L. "Ultrafine Fibrous Cellulose Membranes from Electrospinning of Cellulose Acetate" *J. Polym. Sci.* **2002**, B 40, 2119-2129.

(23) Flory, P. J. *Principles of Polymer Chemistry*, Cornell University Press, Ithaca, N.Y. **1953**

(24) Baumgarten, P. K. "Electrostatic Spinning of Acrylic Microfibers" *J. Coll. Interf. Sci*. **1971**, 36, 71.

(25) Galloway1, J. A.; Koester, K. A.; Paasch, B. J.; Macosko, C. W. "Effect of Sample Size on Solvent Extraction for Detecting Cocontinuity in Polymer Blends" *Polymer* **2004**, 45, 423–428.

(26) Siggia, E. D. "Late Stages of Spinodal Decomposition in Binary Mixtures" Phys. Rev. **1979**, A, 20, 595-605.

(27) Chauvelon, G.; Doublier, J.-L. ; Buleon, A.; Thibault, J.-F.; Saulnier, L. "Rheological properties of sulfoacetate derivatives of cellulose" *Carbohydr. Res*. **2003**, 338, 751-759.

(28) Ha, C. S.; Lee, W. K.; Cho, W. J. "$\Delta\chi$ effects on the miscibility of polymer blends" *Macromolecular Symposia,* **1994**, 84, 1, 279–288.

(29) Etxeberria, A.; Guezala, S.; Iruin, J. J.; de la Campa, J. G.; de Abajo, J. "Miscibility and interactions in a mixture of poly(ethylene oxide) and an aromatic poly(ether amide)" *Polymer*, **1998**, 39, 1035-1042.

(30) Marsac, P. J.; Rumondor, A. C. F.; Nivens, D. E.; Kestur, U. S.; Stanciu, L.; Taylor, L. S. "Effect of temperature and moisture on the miscibility of amorphous dispersions of felodipine and poly(vinyl pyrrolidone)" *Journal of Pharmaceutical Sciences*, **2010**, 99, 1, 169–185.

(31) Crowley, J. D.; Teague Jr, G. S.; Lowe Jr, J. W. "A three-dimensional approach to solubility" *J Paint Technol* **1966**, 38, 496, 269–80.

(32) Crowley, J. D.; Teague Jr, G. S.; Lowe Jr, J. W. "A three-dimensional approach to solubility II" *J Paint Technol* **1967**, 39, 504, 19–2.

(33) Zhang, L.; Hsieh Y.-L.; "Nanoporous ultrahigh specific surface polyacrylonitrile fibres" *Nanotechnology*, **2006**, 17, 4416-4423.

(34) Ji, L.; Saquing, C.; Khan, S. A.; Zhang, X. "Preparation and characterization of silica nanoparticulate-polyacrylonitrile composite and porous nanofibers" *Nanotechnology*, **2008**, 19, 1-9.

(35) Lange, L. E.; Obendorf, S. K. "Effect of Plasma Etching on Destructive Adsorption Properties of Polypropylene Fibers Containing Magnesium Oxide Nanoparticles" *Arch Environ Contam Toxicol*, **2011** (DOI: 10.1007/s00244-011-9702-y.

(36) Park, J.-Y.; Lee, Y.-J.; Jun, K.-W.; Baeg, J.-O.; Yim, D. J. "Chemical Synthesis and Characterization of Highly Oil Dispersed MgO Nanoparticles " *J. Ind. Eng. Chem*., **2006**, 12, 6, 882-887.

(37) Yacob, A. R. Mustajab, M. K. A. A.; Samadi, N. S. "Calcination Temperature of Nano MgO Effect on Base Transesterification of Palm Oil" *World Academy of Science, Engineering and Technology* **2009**, 56, 408-412.

(38) Dixit, V.; Tewari, J.; Obendorf, S. K. "Fungal Growth Inhibition of Regenerated Cellulose Nanofibrous Membranes Containing Quillaja Saponin" *Arch Environ Contam Toxicol* **2010**, 59, 417-423.

(39) Xiang, C.; Frey, M. W.; Taylor, A. G.; Rebovich, M. "Selective chemical absorbance in electrospun nonwovens", *Journal of Applied Polymer Science* **2007**, 106, 2363–2370.

(40) Thompson, C. J.; Chase, G. G.; Yarin, A. L.; Reneker, D. H. "Effects of parameters on nanofiber diameter determined from electrospinning model" *Polymer* **2007**, 48, 6913-6922.

(41) Sing, K. S. W.; Everett, D. H.; Haul, R. A. W.; Moscou, L.; Pierotti, R. A.; Rouquerol, J.; Siemieniewska, T. "Reporting Physisorption Data for Gas/Solid Systems with Special Reference to the Determination of Surface Area and Porosity" *Pure Appl. Chem.*, **1985**, 57, 603.

(42) Barret, E. P.; Joyner, L. G.; Halenda, P. H.; "The determination of pore volume and area distributions in porous substances. I. Computations from nitrogen isotherms." *J. Am. Chem. Soc.* **1951**, 73, 373–380.

(43) Chowdhury, M.; Stylios, G. K. "Analysis of the effect of experimental parameters on the morphology of electrospun polyethylene oxide nanofibres and on their thermal properties" *Journal of the Textile Institute*, **2001**, 1-15.

(44) Miller-Chou, B. A.; Koenig, J. L. "A Review of Polymer Dissolution" *Prog. Polym. Sci.* **2003**, 28, 1223–1270.

(45) Chen, C.; Wang, L.; Huang, Y. "Role of Mn of PEG in the Morphology and Properties of Electrospun PEG/CA Composite Fibers for Thermal Energy Storage" *AIChE Journal*, **2009**, 55 (3), 820-827.

(46) Deitzel, J. M.; Kleinmeyer, J.; Harris, D.; Tan, B. "The effect of processing variables on the morphology of electrospun nanofibres and textiles." *Polymer* **2001,** 42, 261–272.

(47) Fong, H.; Chun, I.; Reneker, D. H. "Beaded nanofibers formed during electrospinning." *Polymer* **1999**, 40, 4585–4592.

(48) Wannatong, L.; Sirivat, A.; Supaphol, P. "Effects of solvents on electrospun polymeric fibers: preliminary study on polystyrene" *Polym Int* **2004**, 53, 1851–1859.

(49) Choktaweesap, N.; Arayanarakul, K.; Aht-ong, D.; Meechaisue, C.; Supaphol, P. "Electrospun Gelatin Fibers: Effect of Solvent System on Morphology and Fiber Diameters" *Polymer Journal*, **2007**, 39 (6), 622–631.

(50) Tungprapa, S.; Puangparn, T.; Weerasombut, M.; Jangchud, I.; Fakum, P.; Semongkhol, S.; Meechaisue C.; Supaphol P. "Electrospun cellulose acetate fibers: effect of solvent system on morphology and fiber diameter" Cellulose **2007**, 14 (6), 563-575.

(51) Marencic, A. P.; Register, R. A. "Controlling Order in Block Copolymer Thin Films for Nanopatterning Applications" *Annual Review of Chemical and Biomolecular Engineering* **2010**, 1, 277-297.

(52) Hamley, I. W., The Physics of Block Copolymers. Oxford University Press: Oxford, **1998**.

(53) Bates, F. S. "Polymer-polymer phase behavior" *Science* **1991**, 251, 898-905.

(54) Matsen, M. W.; Bates, F. S. "Origins of complex self-assembly in block copolymers" *Macromolecules* **1996**, 29, 7641-7644.

(55) Cui, H. G.; Chen, Z. Y.; Zhong, S.; Wooley, K. L.; Pochan, D. J. "Block copolymer assembly via kinetic control" *Science* **2007**, 317, 647-650.

(56) Jinnai, H.; Nishikawa, Y.; Spontak, R. J.; Smith, S. D.; Agard, D. A.; Hashimoto, T. "Direct measurement of interfacial curvature distributions in a bicontinuous block copolymer morphology" *Phys. Rev. Lett.,* **2000**, 84, 518-521

(57) Pernot, H.; Baumert, M.; Court, F.; Leibler, L. "Design and properties of co-continuous nanostructured polymers by reactive blending" *Nature Mater.* **2002**, 1, 54–58.

(58) Nakayama, A.; Inoue, T.; Guegan, P.; Macosko, C. W. "Compatibilizers for melt blending: premade vs. reactively formed block copolymers" *Polym. Prepr.* **1993**, 34, 840–841.

(59) Wilkinson, A. N.; Ryan, A. J. *Polymer Processing: Structure Development,* Kluwer, Dordrecht, The Netherlands, **1998**.

(60) You, Y.; Youk J. H.; Lee, S. W.; Min, B.-M.; Lee, S. J.; Park, W. H. "Preparation of porous ultrafine PGA fibers via selective dissolution of electrospun PGA/PLA blend fibers" *Materials Letters* **2006**, 60, 757-760.

(61) Bognitzki, M.; Frese, T.; Steinhar, M.; Greiner, A.; Wendorff, J. H. "Preparation of Fibers With Nanoscaled Morphologies: Electrospinning of Polymer Blends" Polym. Eng. Sci. **2001**, 41, 982-989.

(62) Bettina Friedel, B.; Ehrler, B.; Hüttner, S.; Greenham, N. C. "Enhanced Nanoscale Imaging of Polymer Blends by Temperature-Controlled Selective Dissolution" *Small* **2011** (DOI: 10.1002/smll.201101860).

(63) Wei, M.; Kang, B.; Sung, C.; Mead, J. "Phase Morphology Control of the Electrospun Nanofibers from the Polymer Blends" *NSTI-Nanotech* **2004**, 3, 375-378.

(64) Kim, M. N.; Koh, J.; Lee, Y.; Kim, H. "Preparation of PVA/PAN bicomponent nanofiber via electrospinning and selective dissolution" *Journal of Applied Polymer Science* **2009**, 113 (1) 274–282.

(65) Lee, J. K.; Han, C. D. "Evolution of a Dispersed Morphology from a Co-Continuous Morphology in Immiscible Polymer Blends" *Polymer*, **1999**, 40, 2521.

(66) Chen, C.; Wang, L.; Huang, Y. "Electrospinning of thermo-regulating ultrafine fibers based on polyethylene glycol/cellulose acetate composite" *Polymer* **2007**, 48, 5202-5207.

(67) Oyama, H. T.; Hemker, D. J.; Frank, C. J. " Effect of the degree of ionization of poly(methacrylic acid) on the complex formed with pyrene end-labeled poly(ethylene glycol)" *Macromolecules* **1989**, 22(3), 1255-1261.

(68) Alkan C.; Sari, A.; Uzun, O. "Poly(ethylene glycol)/acrylic polymer blends for latent heat thermal energy storage" *AlChE Journal* **2006**, 52(9), 3310-3314.

(69) Megelski, S.; Stephens, J. S.; Chase, D. B.; Rabolt, J. F. "Micro- and Nanostructured Surface Morphology on Electrospun Polymer Fibers" *Macromolecules* **2002,** *35,* 8456-8466

(70) Demir, M. M.; Yilgor, I.; Yilgor, E.; Erman, B. "Electrospinning of polyurethane fibers" *Polymer* **2002**, 43, 3303–3309.

(71) Lee, J. K.; Han, C. D. "Evolution of a Dispersed Morphology from a Co-Continuous Morphology in Immiscible Polymer Blends " *Polymer,* **1999**, 40, 2521.

(72) Salem, D. R., Structure Formation in Polymeric Fibers, Hanser Publishers, Munich **2000**.

(73) Walheim, S.; Boltau, M.; Mlynek, J.; Krausch, G.; Steiner, U. *Macromolecules*, **1997**, 30, 4995.

(74) Chamberlain, G.; Joyce, M. Design News **1990**, 20.

(75) Smith, D.; Reneker, D. H. PCT/US00/27737. 200, **2001**.

(76) Yoshizuka, K.; Lou, Z.; Inoue, K. "Silver-complexed chitosan microparticles for pesticide removal" *React Funct Polym* **2000,** 44, 47-54.

(77) Akhtar, M.; Syed, M. H.; Bhanger, M. I.; Iqbal, S. "Low cost sorbents for the removal of methyl parathion pesticide from aqueous solutions" *Chemosphere* **2006**, 66, 1829-1838.

(78) Memon, G. Z.; Bhanger, M. I.; Akhtar, M. "The removal efficiency of chestnut shells for selected pesticides from aqueous solutions" *J Colloid Interf Sci* **2007**, 315, 33-40.

(79) Memon, G. Z.; Bhanger, M. I.; Akhtar, M.; Talpur, F. N.; Memon, J. R. "Adsorption of methyl parathion pesticide from water using watermelon peels as a low cost adsorbent" *Chem Eng J* **2008**, 138, 616-621